Coiled Coils
as Mechanical Building Blocks

Univ.-Diss.
zur Erlangung des akademischen Grades
"doctor rerum naturalium"
(Dr. rer. nat.)
in der Wissenschaftsdisziplin Biochemie

eingereicht an der
Mathematisch-Naturwissenschaftlichen Fakultät
Institut für Biochemie und Biologie
der Universität Potsdam

angefertigt in der
Max-Planck-Forschungsgruppe "Mechano(bio)chemie"
Max-Planck-Institut für Kolloid- und Grenzflächenforschung

von

Patricia López García

Potsdam, June 2019

Declaration

The enclosed research was conducted in the Max Planck Research Group 'Mechano(bio)chemistry' at the Max Planck Institute of Colloids and Interfaces (MPIKG), under the supervision of Dr. Kerstin G. Blank between July 2015 and December 2018. This thesis has not been submitted for any other qualifications at this or any other institution. This dissertation is the original work of the author and does not include any research that is the outcome of work done in collaboration with others, apart from those specifically indicated in the text and acknowledgements.

Eidesstattliche Erklärung

Die vorliegende Arbeit wurde in der Zeit von Juli 2015 bis Dezember 2018 am Max-Planck-Institut für Kolloid- und Grenzflächenforschung in der Max-Planck-Forschungsgruppe 'Mechano(bio)chemie' unter der Leitung von Dr. Kerstin G. Blank angefertigt. Die Arbeit ist bisher an keiner anderen Hochschule eingereicht worden und wurde zudem selbständig und ausschließlich mit den angegebenen Mitteln angefertigt. Hiermit erkläre ich an Eides statt, dass ich die vorliegende Arbeit selbstständig verfasst und nur unter Zuhilfenahme der ausgewiesenen Quellen und Hilfsmittel angefertigt habe. Beiträge von Kooperationspartnern wurden explizit gekennzeichnet.

Referees

Dr. Kerstin G. Blank (MPIKG, Germany)

Dr. Ruby May Arana Sullan (University of Toronto, Canada)

Prof. Dr. Henrike Müller-Werkmeister (University of Potsdam, Germany)

Potsdam, June 2019

Patricia López García

TABLE OF CONTENTS

1. SUMMARY

The natural abundance of Coiled Coil (CC) motifs in cytoskeleton and extracellular matrix proteins suggests that CCs play an important role as passive (structural) and active (regulatory) mechanical building blocks. CCs are self-assembled superhelical structures consisting of 2-7 α-helices. Self-assembly is driven by hydrophobic and ionic interactions, while the helix propensity of the individual helices contributes additional stability to the structure. As a direct result of this simple sequence-structure relationship, CCs serve as templates for protein design and sequences with a pre-defined thermodynamic stability have been synthesized *de novo*. Despite this quickly increasing knowledge and the vast number of possible CC applications, the mechanical function of CCs has been largely overlooked and little is known about how different CC design parameters determine the mechanical stability of CCs. Once available, this knowledge will open up new applications for CCs as nanomechanical building blocks, e.g. in biomaterials and nanobiotechnology.

With the goal of shedding light on the **sequence-structure-mechanics relationship** of CCs, a well-characterized heterodimeric CC was utilized as a model system. The sequence of this model system was systematically modified to investigate how different design parameters affect the CC response when the force is applied to opposing termini in a shear geometry or separated in a zipper-like fashion from the same termini (unzip geometry). The force was applied using an atomic force microscope set-up and dynamic single-molecule force spectroscopy was performed to determine the rupture forces and energy landscape properties of the CC heterodimers under study. Using force as a denaturant, CC chain separation is initiated by helix uncoiling from the force application points. In the shear geometry, this allows uncoiling-assisted sliding parallel to the force vector or dissociation perpendicular to the force vector. Both competing processes involve the opening of stabilizing hydrophobic (and ionic) interactions. Also in the unzip geometry, helix uncoiling precedes the rupture of hydrophobic contacts.

In a first series of experiments, the focus was placed on **canonical modifications in the hydrophobic core and the helix propensity**. Using the shear geometry, it was shown that both a reduced core packing and helix propensity lower the thermodynamic and mechanical stability of the CC; however, with different effects on the energy landscape of the system. A less tightly packed hydrophobic core increases the distance to the transition state, with only a small effect on the barrier height. This originates from a more dynamic and less tightly packed core, which provides more degrees of freedom to respond to the applied force in the direction of the force vector. In contrast, a reduced helix propensity decreases both the distance to the transition state and the barrier height. The helices are 'easier' to unfold and the remaining structure is less thermodynamically stable so that dissociation perpendicular to the force axis can occur at smaller deformations.

Having elucidated how canonical sequence modifications influence CC mechanics, the **pulling geometry** was investigated in the next step. Using one and the same sequence, the force application points were exchanged and two different shear and one unzipping geometry were compared. It was shown that the pulling geometry determines the mechanical stability of the CC. Different rupture forces were observed in the different shear as well as in the unzipping geometries, suggesting that chain separation follows different pathways on the energy landscape. Whereas the difference between CC shearing and unzipping was anticipated and has also been observed for other biological structures, the observed difference for the two shear geometries was less expected. It can be explained with the structural asymmetry of the CC heterodimer. It is proposed that the direction of the α-helices, the different local helix propensities and the position of a polar asparagine in the hydrophobic core are responsible for the observed difference in the chain separation pathways. In combination, these factors are considered to influence the interplay between processes parallel and perpendicular to the force axis.

To obtain more detailed insights into the role of helix stability, helical turns were reinforced locally using **artificial constraints in the form of covalent and dynamic '*staples*'**. A covalent staple bridges to adjacent helical turns, thus protecting them against uncoiling. The staple was inserted directly at the point of force application in one helix or in the same terminus of the other helix, which did not experience the force directly. It was shown that preventing helix uncoiling at the point of force application reduces the distance to the transition state while slightly increasing the barrier height. This confirms that helix uncoiling is critically important for CC chain separation. When inserted into the second helix, this stabilizing effect is transferred across the hydrophobic core and protects the force-loaded turns against uncoiling. If both helices were *stapled*, no additional increase in mechanical stability was observed. When replacing the covalent staple with a dynamic metal-coordination bond, a smaller decrease in the distance to the transition was observed, suggesting that the staple opens up while the CC is under load.

Using **fluorinated amino acids** as another type of non-natural modification, it was investigated how the enhanced hydrophobicity and the altered packing at the interface influences CC mechanics. The fluorinated amino acid was inserted into one central heptad of one or both α-helices. It was shown that this substitution destabilized the CC thermodynamically and mechanically. Specifically, the barrier height was decreased and the distance to the transition state increased. This suggests that a possible stabilizing effect of the increased hydrophobicity is overruled by a disturbed packing, which originates from a bad fit of the fluorinated amino acid into the local environment. This in turn increases the flexibility at the interface, as also observed for the hydrophobic core substitution described above. In combination, this confirms that the arrangement of the hydrophobic side chains is an additional crucial factor determining the mechanical stability of CCs.

In conclusion, this work shows that knowledge of the thermodynamic stability alone is not sufficient to predict the mechanical stability of CCs. It is the interplay between helix

propensity and hydrophobic core packing that defines the sequence-structure-mechanics relationship. In combination, both parameters determine the relative contribution of processes parallel and perpendicular to the force axis, i.e. helix uncoiling and uncoiling-assisted sliding as well as dissociation. This new mechanistic knowledge provides insight into the mechanical function of CCs in tissues and opens up the road for designing CCs with pre-defined mechanical properties. The **library of mechanically characterized CCs** developed in this work is a powerful starting point for a wide spectrum of applications, ranging from molecular force sensors to mechanosensitive crosslinks in protein nanostructures and synthetic extracellular matrix mimics.

2. ZUSAMMENFASSUNG

Das „Coiled Coil" (CC) Faltungsmotiv ist Bestandteil vieler Proteine im Zytoskelett und der extrazellulären Matrix. Es kann daher davon ausgegangen werden, dass CCs essentielle mechanische Bausteine darstellen, die sowohl passive (strukturelle) als auch aktive (regulatorische) Aufgaben erfüllen. CCs bestehen aus 2-7 α-helikalen Untereinheiten, die eine superhelikale Struktur formen. Die Faltung und Stabilität der Superhelix wird durch hydrophobe und ionische Wechselwirkungen bestimmt, sowie durch die Helixpropensität der einzelnen Aminosäuren. Auf der Grundlage dieser gut verstandenen Struktur-Funktionsbeziehungen werden CCs häufig als Vorlage für das *de novo* Proteindesign genutzt. Trotz stetig wachsender wissenschaftlicher Erkenntnisse und der mannigfaltigen Anwendungsmöglichkeiten von CCs, ist ihre mechanische Funktion noch weitestgehend unerforscht. Insbesondere ist der Zusammenhang zwischen der Aminosäuresequenz und der mechanischen Stabilität kaum bekannt. Dieses Wissen ist jedoch essentiell für die Anwendung von CCs als nanomechanische Bausteine.

Um die **mechanischen Struktur-Funktionsbeziehungen von CCs** zu beleuchten, wurde ein gut charakterisiertes CC-Heterodimer als Modellsystem genutzt. Dessen Sequenz wurde systematisch modifiziert, um den Einfluss verschiedener Strukturparameter auf die mechanische Stabilität des CCs zu untersuchen. Mittels Rasterkraftmikroskop-basierter Einzelmolekülkraftspektroskopie wurden die Kraftangriffspunkte so platziert, dass das CC entweder geschert oder wie ein Reißverschluss geöffnet wurde („Unzip"-Geometrie). Dabei wurde die Kraft bestimmt, die zur Separation der beiden Helices benötigt wird. Diese sogenannte Abrisskraft wurde bei verschiedenen Ladungsraten gemessen, um Rückschlüsse auf die Energielandschaft der CCs zu ziehen. Die anliegende Kraft führt zunächst zur Entfaltung der Helix-Enden an den Kraftangriffspunkten. Diese partielle Entfaltung ermöglicht in der Scher-Geometrie zwei Mechanismen, die letztlich zur Separation der Helices führen: die Verschiebung der Helices entlang des Kraftvektors und die Dissoziation senkrecht zur angelegten Kraft. Auch in der „Unzip"-Geometrie geht die teilweise Entfaltung der Dissoziation voraus.

Zunächst wurde der Einfluss von **hydrophoben Wechselwirkungen im Kern des CCs sowie der Helixpropensität** systematisch untersucht. In der verwendeten Scher-Geometrie führten entsprechende Aminosäuremodifikationen zu einer Änderung der Abrisskraft des CCs, wobei spezifische Unterschiede in der Energielandschaft festzustellen sind. Weniger dicht gepackte hydrophobe Wechselwirkungen verlängern hauptsächlich den Abstand zum Übergangszustand, da sie die Freiheitsgrade des Entfaltungspfades erhöhen. Eine verringerte Helixpropensität verringert sowohl die Aktivierungsenergie als auch den Abstand zum Übergangszustand. Die niedrige thermodynamische Stabilität dieser Modifikation führt dazu, dass weniger Kraft angewandt werden muss, um die Dissoziation der Helices senkrecht zum Kraftvektor zu erreichen.

Mit diesem Wissen über den Einfluss der Helixpropensität und der hydrophoben Wechselwirkungen, wurde anschließend die **mechanische Entfaltung in zwei verschiedenen Scher-Geometrien, sowie der „Unzip"-Geometrie** untersucht. Dazu wurde jeweils die gleiche Sequenz verwendet, wobei nur die Kraftangriffspunkte modifiziert wurden. Die Ergebnisse zeigen, dass die Positionierung der Kraftangriffspunkte essentiell für die gemessene mechanische Stabilität des CC ist. Wie auch in anderen biologischen Strukturen zu beobachten, besteht ein Unterschied zwischen Scher- und „Unzip"-Geometrie. Jedoch weist das CC auch in den beiden Scher-Geometrien Unterschiede in der Stabilität auf. Dies ist auf eine Asymmetrie der ansonsten hochrepetitiven Sequenz zurückzuführen.

Die **Rolle der Helixstabilität** wurde durch die lokale Stabilisierung von Helixwindungen mit **kovalenten und dynamischen molekularen Klammern** genauer erforscht. Die Klammern verknüpfen zwei benachbarte Windungen und stabilisieren diese so gegen die mechanische Entfaltung. Die kovalente Klammer wurde entweder direkt am Kraftangriffspunkt eingefügt oder in der Partnerhelix, an der die Kraft nicht direkt angreift. Es wurde gezeigt, dass die Klammern die mechanische Stabilität des CCs erhöhen. Dem liegen eine Verringerung des Abstands zum Übergangszustand und eine leichte Erhöhung der Energiebarriere zu Grunde. Helix-stabilisierende Effekte können durch die hydrophoben Wechselwirkungen auf die Partnerhelix übertragen werden. Das Klammern beider Helices führte nicht zu einer weiteren Erhöhung der mechanischen Stabilität. Bei Einfügen einer dynamischen Klammer direkt am Kraftangriffspunkt fällt die Verringerung des Abstands zum Übergangszustand kleiner aus. Dies ist auf das Öffnen der reversiblen Klammer bei Krafteinwirkung zurückzuführen.

Auch die Rolle der **hydrophoben Wechselwirkungen** wurde unter Verwendung einer nicht-natürlichen Modifikation detaillierter untersucht. Dazu wurde eine **fluorinierte Aminosäure** im zentralen Teil des CCs eingebaut. Die fluorinierte Aminosäure ist hydrophober als die Ursprüngliche und verändert die Packung der Seitenketten im hydrophoben Kern. Die Anwesenheit der fluorinierten Aminosäure in einer der beiden Helices führte zu einer Erniedrigung der Aktivierungsenergie sowie zu einer gleichzeitigen Erhöhung des Abstandes zum Übergangszustand. Dies zeigt, dass die fluorinierte Aminosäure in erster Linie die Packung der hydrophoben Aminosäuren stört, während der Einfluss des hydrophoben Effekts ehr gering ist. Die fluorinierte Aminosäure kann nicht gut in die lokale Umgebung der anderen Aminosäuren integriert werden und zeigt so, dass die Anordnung und Wechselwirkung der hydrophoben Aminosäuren im Kern essentiell für die mechanische Stabilität von CCs ist.

Zusammenfassend zeigt diese Arbeit, dass allein auf Grundlage der thermodynamischen Stabilität nicht auf die mechanische Stabilität von CCs geschlossen werden kann. Das Zusammenspiel zwischen Helixstabilität und hydrophoben Wechselwirkungen ist maßgebend um die Zusammenhänge zwischen Sequenz, Struktur und mechanischer Stabilität von CCs zu verstehen. Beide Faktoren tragen zu den Entfaltungsmechanismen parallel und senkrecht zur Kraftrichtung bei. Diese neuen

mechanistischen Einblicke in die sequenzabhängige mechanische Stabilität von CCs ermöglichen die Entwicklung von CCs mit maßgeschneiderten mechanischen Eigenschaften. Die hier **charakterisierte CC-Bibliothek ist ein hervorragender Ausgangspunkt** für ein breites Spektrum an potentiellen Anwendungen, von molekularen Kraftsensoren bis zu mechanosensitiven Bausteinen für Proteinnanostrukturen und künstlichen extrazellulären Matrices.

3. LIST OF ABBREVIATIONS

AFM Atomic force microscope

Ala Alanine

Asn Asparagine

ATP Adenosine triphospate

CC Coiled Coil

CD Circular dichroism

Cys Cysteine

ECM Extracellular matrix

EDTA Ethylenediaminetetraacetic acid

F Force

FA Focal adhesion

FJC Freely-jointed chain

Gln Glutamine

Glu Glutamic acid

HPLC High performance liquid chromatography

Ile Isoleucine

IFs Intermediate Filaments

k spring constant

k_B Boltzmann constant

KIH Knobs-into-holes

k_{off} force-free dissociation constant

L_c contour length

Leu Leucine

L_p persistence length

MALDI-TOF Matrix-assisted laser desorption/ionization – Time of flight

MD Molecular dynamics

ME Molar ellipticity

Met Methionine

MFS Molecular force sensor

min minute

NHS *N*-hydroxy succinimide

PBS Phosphate buffered saline

PDB Protein Data Bank

PEG Poly(ethylene glycol)

Phe Phenylalanine

PIPPS-BS Piperazine-N,N′-*bis*(3-propanesulfonic acid) buffered saline

r Loading rate

SEM Standard error of the mean

SMFS Single-molecule force spectroscopy

SNARE Soluble NSF attachment protein receptor

SPPS Solid phase peptide synthesis

T Temperature

TCEP Tris(2-carboxyethyl)phosphine

TfeGly (S)-4,4,4-trifluoroethylglycine

Thr Threonine

T_m Melting temperature

Trp Tryptophan

Tyr Tyrosine

UV Ultra-violet

Val Valine

WLC Worm-like chain

z distance in the z-axis

ΔG Gibbs free energy

Δx Distance to the transition state

4. INTRODUCTION

Coiled Coils (CCs) have been studied over many decades since Crick, and simultaneously Pauling and Corey, described the first interpretation of this α-helical self-assembled motif [1, 2]. Their interpretation was based on the discovery of the fibrous *k-m-e-f* proteins (keratin, myosin, epidermin and fibrinogen) described by Astbury in 1945 in a series of lectures titled "The Structure of Biological Fibres and the Problem of Muscle" [3]. The discovery of these structures and their analysis laid the foundation for understanding the secondary structures of proteins.

Many CC containing proteins are involved in sensing and exerting mechanical forces in biological systems. They are essential building blocks of the cytoskeleton and the extracellular matrix (ECM) where they, for example, contribute to cell migration, division and mechanosensing [4]. Considering this important mechanical function, still little is known about the forces experienced by and transmitted through these structures. Furthermore, limited information is available about the mechanistic response of these structures when they are under mechanical load.

The present work aims to investigate the relationship between sequence, structure and mechanics of these important protein building blocks. Specifically, my goal is to investigate how modifications in the amino acid sequence affect the mechanical stability of CC heterodimers. Using this information, I aim to establish a series of guidelines that will allow the design of CCs with pre-defined mechanical properties for a range of different applications. In this introduction, I will give an overview of the occurrence of CC domains in Nature with a focus on CCs involved in mechanical processes. I will further explain the basic rules of rational CC design and introduce key applications in biochemistry, synthetic biology and materials science where the mechanical properties of CCs are of importance.

4.1. COILED COILS IN NATURE

To date, more than 140,000 structures can be found in the Protein Data Bank (PDB). When inserting the term "Coiled Coil", >1,400 crystal structures are obtained. On average, CCs further represent 2.86 % of all proteins in every genome sequenced so far [5].

In 1945, William Astbury discovered the first CC structures when investigating hair, muscle, blood clots, and skin samples with X-ray diffraction [3]. In the diffraction patterns, he identified a spacing of ~0.51 nm, which he called "alpha-pattern". It was not until 1953 when Francis Crick, Linus Pauling and Robert B Corey [1, 2] used the name **α-helix** to describe these structures (Figure 1A). Each helix is stabilized by hydrogen bonds between

the N-H and C=O groups of the peptide backbone, following a *i, i + 4* pattern. In a **Coiled Coil** two or more (up to seven) α-helices wind around each other at an angle of 20° with the following characteristics, as proposed by Crick:

- The CC structure has a periodicity of seven amino acids over two helical turns (3.5 residues per turn). This periodicity is termed *heptad.*
- The canonical heptad pattern, often depicted with the letters *abcdefg,* places hydrophobic amino acids in the *a* and *d* positions. The *e* and *g* positions are occupied with charged amino acids and the amino acids in the *b*, *c* and *f* positions are mostly hydrophilic (Figure 1B).
- The side chains of the hydrophobic residues interact with each other in a *knobs-into-holes* (KIH) fashion. This distorts the axes of the individual helices axis and results in *supercoil* formation. In the supercoil, each turn contains 3.5 residues instead of 3.63 residues as in a regular α-helix.

Although the Crick model suggests this 7-residue periodicity, different periodicities have been observed [6]. Also, insertions of three (i.e. stammers) or four (i.e. stutters) residues have been found, leading to different geometries of the CC. The addition of three residues does not complete a full helical turn thereby tensing the supercoil (local change of -17°, left-handed coil); while the addition of four residues introduces more than one helical turn, therefore relaxing the supercoil (local change of +17°, right-handed coil).
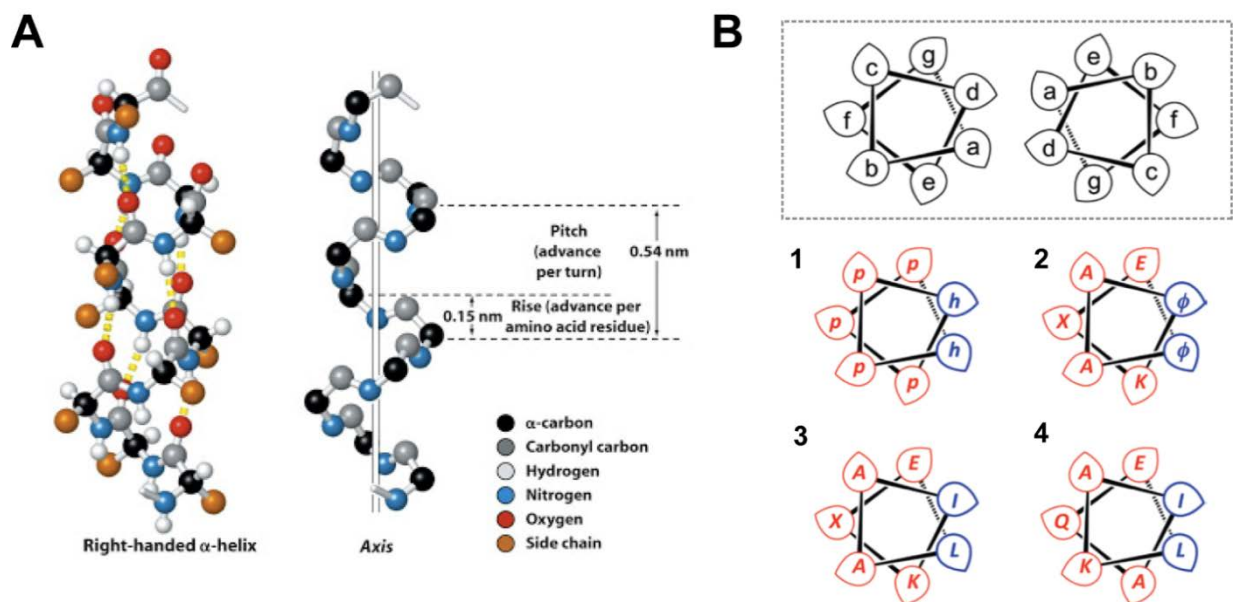
FIGURE 1 - α-helix and Coiled Coil structures. A) Structure of an α-helix as proposed by Crick and Pauling. (Extracted from Principles of Biochemistry, Pearson Ed. [7]). B) Helical wheel diagram of a dimeric CC (dashed box) following the pattern *abcdefg,* where *a* and *d* form the hydrophobic core. The orientation of the side chain of each residue is represented by the tip of each symbol. B1 shows the pattern of polar (p) and hydrophobic residues (h). In B2, the same pattern is substituted with the typical amino acids used for *de novo* CC design, where Φ represents different *h* amino acids (other amino acids in one-letter code). B3 and B4 show examples of homotetrameric and homohexameric CCs. (Reprinted with permission from Springer Nature: Coiled-coil design: updated and upgraded, Derek N. Woolfson; Copyright © 2017, Springer International Publishing AG [8])

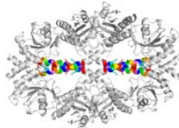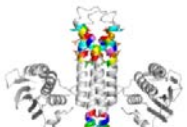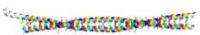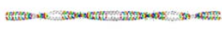Despite the usually well-defined periodicity, CCs are a diverse set of proteins. They comprise an enormous variety of monomer **lengths** (from 28 residues of the GCN4 leucine zipper to 1,123 residues of myosin [9]); **oligomerization states** (dimers, trimers, tetramers, pentamers, etc.; depending on their sequence as seen in Figure 1B); **geometries** (parallel or anti-parallel); **arrangements** (fibers, levers, tubes, funnels, sheets, spirals and rings); **deviations of the regular α-helix pattern** (3_{10}-helices, π-turns, αβ-Coiled Coils) and **function** [10] (Table 1).

CCs do not only appear on their own but often assemble into fibrous proteins (e.g. keratin). They also form domains in many other proteins [11], including globular proteins or proteins with a globular portion (e.g. myosin, kinesin, fibrinogen, M-protein and laminin). CC domains in globular proteins are often less regular and contain a larger fraction of polar and charged residues. Differences in CC sequence are also observed depending on the location in the cell. For instance, CCs in transmembrane proteins contain a larger number of apolar residues.

To gain more insight into the structure-function relationships of natural CCs and to predict CC structures *in silico*, various bioinformatics tools have been developed in recent years. For example, **CC+** [12] allows for searching a specific CC architecture in the PDB database. Focusing on the subject of this work (heterodimeric parallel CCs), the search delivered 751 2-helix-based CCs that were found in natural proteins. They can be classified in 2-stranded (if the CC motif belongs to the same chain) or dimeric (if the CC motif belongs to different chains). Out of the 751 2-helix CCs, 210 were dimeric CCs out of which only 107 were classified as canonical parallel CCs (7/2 periodicity as in the Crick model).

Whereas CC+ aids in searching for already published CCs, **CCBuilder** allows for predicting a 3D structural model based on the amino acid sequence, topology and orientation [13]. Other tools include **LOGICOIL,** which predicts the oligomerization state [14]; **bZIPA,** which yields the CC thermodynamic stability (melting temperature) [15]; and, lastly, **SOCKET,** a tool for KIH prediction in the hydrophobic interface [16]. In the ExPASY web portal [17] more prediction and docking software can be found, such as COILS [18], MARCOIL [19], SwissParam [20], TMHMM [21], etc.

TABLE 1 - Examples of proteins containing canonical parallel Coiled Coils in Nature. The CC part of the protein is coloured. *Number of residues = number of amino acids of the CC domain. (Extracted from CC+ database[12])

Name	PDB ID	Number of residues*	Organism	Function	Structure
Leucine Zipper	1A93	21	*Homo sapiens*	Transcription Factor	
Cortexillin	1D7M	95	*Dictyostelium discoideum*	Contractile Protein	
Enhancer Binding Protein B	1H88	32	*Homo sapiens*	Transcription Factor	
3',5'-Cyclic Nucleotide Phosphodiesterase 2a	1mc0	21	*Mus musculus*	Hydrolase	
Circadian Clock Protein Kaia	1R8J	14	*Synechococcus elongatus*	Circadian Clock Protein	
Sensor Histidine Kinase Protein	2C2A	11	*Thermotoga maritima*	Transferase	
Beta-Myosin S2 Fragment	2FXM	105	*Homo sapiens*	Contractile Protein	
Alpha-Tropomyosin	2D3E	10	*Oryctolagus cuniculus*	Contractile Protein	

4.1.1. COILED COILS AS PARTS OF INTRACELLULAR PROTEINS

The cytoskeleton of eukaryotic cells is composed of three protein-based networks, which are involved in a large number of cell functions, such as shape maintenance, movement, vesicle transport, etc. These are the actin-myosin network, intermediate filaments (IFs) and microtubules, which are associated with the molecular motors kinesin and dynein. Among these proteins, IFs and the motor proteins are composed of CCs or possess CC domains [10].

All IF types share a common structure, consisting of a central CC rod, flanked by globular domains at the N- (head domain) and C-termini (tail domain) [22]. Examples of IFs are keratin (Type II), vimentin and desmin (Type III), neurofilaments (Type IV) and

lamin (Type V). All IFs are located in the cytoskeleton of the cell, except for lamin, which is located in the nucleus. The first IF discovered was **α-keratin** [23]. This IF is composed of parallel homo- or heterodimers, which assemble into an antiparallel tetramer. These tetramers subsequently form higher order structures, which ultimately construct the α-keratin network that preserves the shape of cells [24]. Recent studies have identified a 14 residue motif that is responsible for nucleating CC formation [25]. **Vimentin** maintains the same salt bridges as keratin, which is a key factor for its stabilization [26].

Among the motor proteins, **myosin** is the most well-known. It is composed of a *head*, *neck* and *tail* domain [27]. The *head* domain (comprising the actin-binding motor and regulatory region) is very well conserved in the myosin family. The *tail* of myosin [28] contains a parallel 2-stranded CC, which is composed of 1,123 amino acids. CC formation triggers the self-assembly of the protein and confers the necessary elasticity for force generation and motor function [29].

Kinesin is structurally and functionally similar to myosin. The *head* domain binds microtubules and is responsible for its motor activity. The *neck* domain contains a CC, which plays an important role in the rearrangement of the structure thanks to ATP hydrolysis, leading to its motor function [30]. **Dynein**, the second microtubule-binding molecular motor, possesses a different structure, where the microtubule binding site is spatially separated from the site of ATP hydrolysis. These two functional units are connected by a highly conserved antiparallel CC, the so-called stalk domain. Upon ATP hydrolysis, the stalk domain allosterically transduces the mechanical force between the head domain and the microtubule binding site [10].

In addition to these key cytoskeleton proteins, also other cytoskeleton proteins contain CC structures. The first ever described cytoskeleton protein consisting exclusively of a CC is **tropomyosin**. Its structure consists of two parallel α-helices of a total of 248 residues in a canonical (7/2) periodicity [31]. Tropomyosins interact with actin filaments and play a regulatory role in the actin-myosin cytoskeleton.

4.1.2. COILED COILS AS PARTS OF ECM PROTEINS

In addition to the cytoskeleton, also the extracellular matrix (ECM) contains a large number of CC structures. The ECM varies greatly from tissue to tissue (e.g. stiffness and composition are different in brain and skeletal muscle), but has the following properties in common: it regulates tissue viscoelasticity, provides cell attachment sites and biochemical signals (e.g. binding and release of growth or coagulation factors) and influences the morphological space in which cells grow, differentiate and migrate (Figure 2) [32]. The ECM thus acts as a mechanical support for cells and plays an active role in the bidirectional mechanobiochemical signalling between cells and their environment. The ECM therefore contributes to controlling cell fate processes. ECM proteins, which include CCs in their structure, are fibrinogen, laminin, cartilage oligomeric matrix protein (COMP), etc. [33].

One of the ECM proteins composed of CCs is **fibrinogen**. Fibrinogen is a 340 kDa heterotrimeric CC-based glycoprotein. After activation in a protease cascade, it assembles into higher order structure, i.e. fibrin fibres. Fibrin plays an important role in blood clotting and the CC domain is known to be involved in determining the mechanical properties of blood clots [34]. Fibrin lysis involves the enzyme plasmin, which cleaves fibrin in a very flexible region in the CC domain. This cleavage site is exposed upon bending (as a hinge), once again highlighting the mechanical importance of CCs in Nature [34].

Another example of a CC-based ECM protein is **laminin.** Laminin is a 800 kDa cross-shaped heterotrimeric protein. It interacts with the fibre-forming ECM proteins fibrin and/or collagen, thereby playing a key role in the assembly and maintenance of the ECM network. Laminins also display cell-adhesion sites (e.g. the RGDS motif). The CC region forms the "body" of the protein with a certain flexibility, while the "head" and "feet" are globular domains with growth factor function [35].
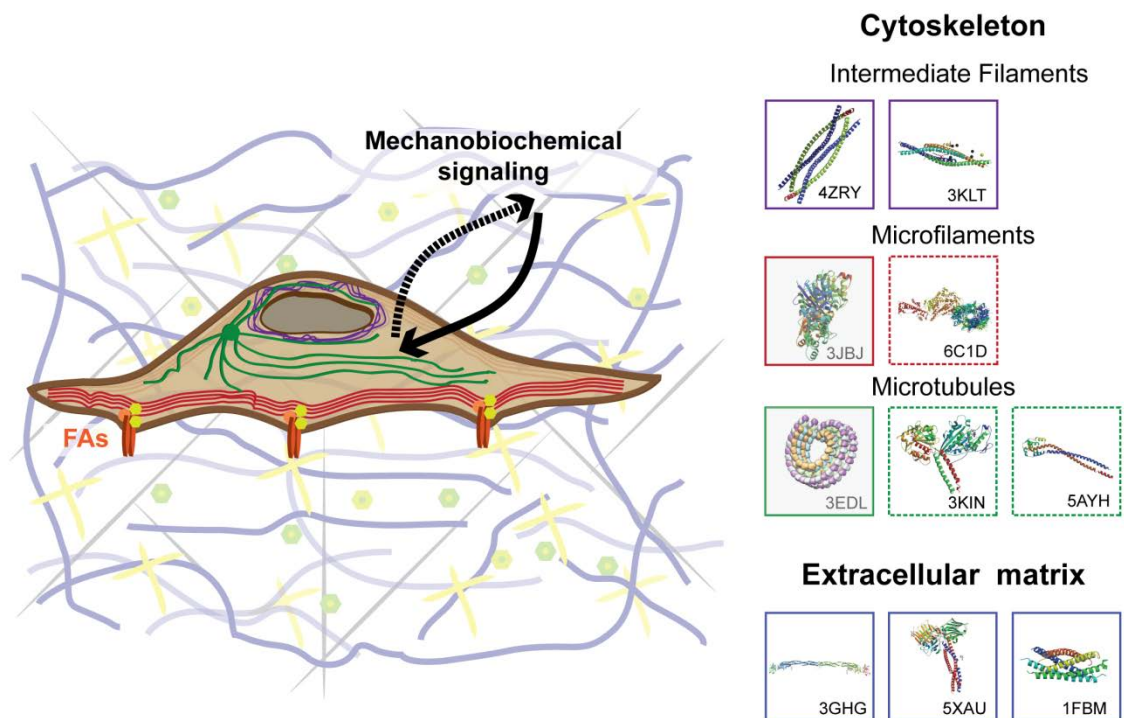
FIGURE 2 – Structural and motor proteins present in the cytoskeleton and the ECM. The cytoskeleton and the ECM are mechanically connected at FA sites, which mediate cell adhesion at the cell-ECM interface. FAs are key structures involved in mechanobiochemical signaling cascades, which are bidirectional (cell to ECM and ECM to cell). The structures of essential cytoskeleton and ECM proteins are shown on the right. The structures are extracted from the PBD: 4ZRY – heterocomplex 2B domain of keratin 1 and keratin 10; 3KLT – vimentin fragment; 3JBJ – F-actin; 6C1D – actin bound myosin; 3EDL – kinesin 13 bound to microtubule ring complex; 3KIN – dimeric kinesin; 5AYH – dynein stalk region; 3GHG – fibrinogen; 5XAU – integrin binding fragment of laminin-511; 1FBM – COMP.

COMP is a 525 kDa 5-stranded CC localized in the ECM of cartilage and tendon [36]. The five α-helices form a hydrophobic cavity that has the ability of storing hydrophilic molecules. This suggests its involvement in cell-ECM signalling [37]. Mutation of the COMP

gene leads to genetic disorders like *pseudoachondroplaxia*, a phenotype expressed as lax joints, among other features. This suggests that COMP also contributes to the ECM scaffolding of tissues.

CC-forming proteins in the cytoskeleton and the ECM are connected at **focal adhesion** (FA) sites (Figure 2). FAs are the major protein complex involved in mechanotransduction, sensing the forces that are transmitted between the cell and the ECM. FAs are mainly composed of integrins [38] and adaptor proteins [39], which are recruited after the cell binds to the matrix. To initiate FAs, integrins bind to a specific motif (i.e. RGDS) exposed on the surface of ECM-forming fibres.

Overall, many CC structures are experiencing mechanical load and are essential for maintaining cell and tissue integrity. Force is thus an important factor to consider when studying CCs and their functions, both at a cellular and at a molecular level. Considering the large variety of CC-containing proteins that are involved in mechanotransduction in Nature, detailed mechanistic insights into their sequence-structure-mechanics relationship is essential for understanding their function in tissues and for the creation of *de novo* CCs with pre-defined mechanical properties.

4.2.   RATIONAL DESIGN OF COILED COILS

To understand how CCs with defined properties can be designed, the basic sequence-structure relationship of CCs will be discussed in the following. CCs consist of two (up to seven) α-helices that wrap around each other. These α-helices have a characteristic heptad *abcdefg* pattern that facilitates their association into a supramolecular structure [8, 18, 40]. *a* and *d* are hydrophobic amino acids (Ile, Val or Leu), which define the hydrophobic core of the structure by KIH interactions (i.e. the side chain of one residue fits into the space between the side chains of the surrounding hydrophobic residues). *e* and *g* are usually charged amino acids (Glu, Arg, or Lys), which form interhelical salt bridges, thus specifying the topology of the CC (oligomerization state and helix orientation). Finally, *b, c,* and *f* are solvent-exposed amino acids, normally polar (Ser, Asn, Gln, etc.). Their helix propensity strongly contributes to the stability of the CC [41]. A typical helical wheel diagram, representing this heptad pattern, is shown in Figure 3.

A series of design guidelines [10, 18, 42-47] has been established for predicting different CC features. These include position-specific information about the effect of different amino acids on CC stability, strategies for establishing specificity and orthogonality in hetero-oligomers as well as a threshold length required to obtain a thermodynamically stable CC.
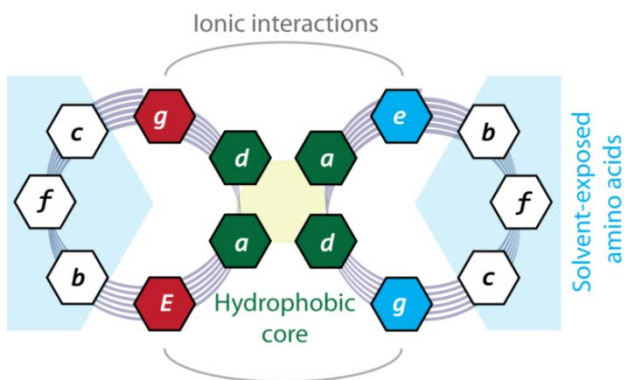
FIGURE 3 – Characteristic heptad pattern of a dimeric Coiled Coil. The scheme shows the hydrophobic interface, ionic interactions (or salt bridges) and the solvent-exposed amino acids on the Coiled Coil surface. Only one heptad characterized by the *abcdefg* repeat pattern is depicted.

Amino acids that exhibit long and charged side chains are the most frequent residues to populate a CC motif in combination with hydrophobic amino acids (Table 2). The most frequent hydrophobic amino acid is leucine. Glutamine is the most frequent polar amino acid and occurs on the solvent-exposed surface of CCs. In some cases, the CC sequence is less regular than the above-mentioned heptad pattern, i.e. a polar or charged residue may be placed in a *traditional* hydrophobic position, and vice versa, without disturbing the overall fold of the CC [48].

TABLE 2 – Amino acid content in Coiled Coils. [Adapted with permission from Oxford University Press: Evolutionary patterns in coiled-coils, Surkont, Jaroslaw; Pereira-Leal, Jose B. (Copyright © 2015, Oxford University Press] [49])

	Amino acid	Frequency in Coiled Coils (%)
Hydrophobic residues	Ile (I)	4
	Leu(L)	**12.5**
	Met (M)	2
	Phe (F)	1
	Trp (W)	<1
	Tyr (Y)	1
	Val (V)	4
	Pro (P)	0.5
	Ala (A)	7.5
Charged residues	Arg (R)	7.5
	Asp (D)	4.5
	Glu (E)	**16**
	Lys (K)	10
	His (H)	2
Polar residues	Asn (N)	4
	Cys (C)	1
	Gln (Q)	**10**
	Gly (G)	2.5
	Ser (S)	6
	Thr (T)	4

Not only the sequence, but also the **length** is important for CC stability: an increment of the CC length from 3 to 4 and 5 heptads increases CC stability [50]. The length increase

favours helix propagation from the N-terminus, while helix propagation from the C-terminus becomes less favourable or remains unaffected [44]. Furthermore, as the terminal heptads tend to fray, adding central heptads leads to a disproportionally high stabilization of the entire CC [45].

In the following, the key rules for the design of CCs will be discussed. These rules are mostly based on structural studies of the **GCN4 leucine zipper,** first published by O'Shea et al. [51] in 1991 (Figure 4). The structure is comprised of two parallel 30-residue peptides, forming a homodimer. In the hydrophobic core, the *a* position is mostly occupied by Val and the *d* position by Leu. In the third heptad, a polar Asn is located in the *a* position. This Asn forms a hydrogen bond with the Asn located in the other helix. Glu and Lys, located in the *e* and *g* positions, form ionic interactions on the CC surface. The rest of the solvent-exposed surface (*b, c, f*) is composed of mostly polar and charged amino acids: Ala, Ser, Tyr, His, Lys, Gln, Glu, Arg, and Asn.
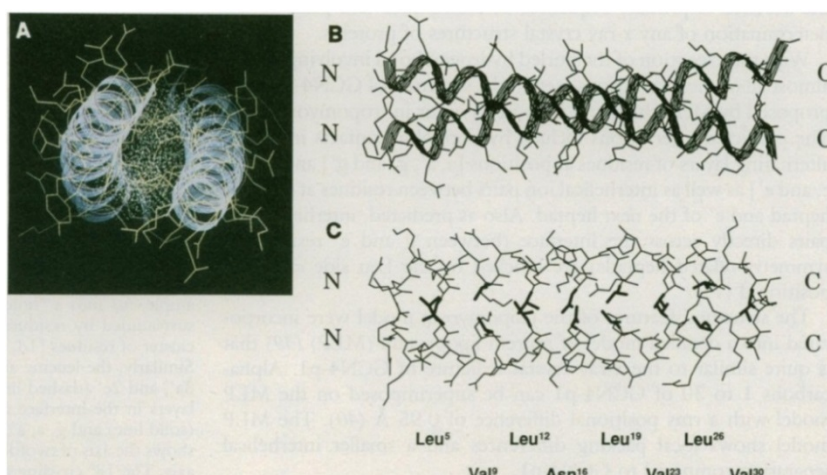
FIGURE 4 – **Structure of the GCN4 leucine zipper.** A) Front view of the dimer along the superhelix axis from the N-terminus. B) Side view of the CC. The amino acids located in positions *a* and *d* are shown in C). [Reprinted with permission from The American Association for the Advancement of Science: X-ray structure of the GCN4 leucine zipper, a two-stranded, parallel Coiled Coil, E. K. O'Shea, J. D. Klemm, P. S. Kim, T Alber [Copyright © 1991] [51]].

4.2.1. HYDROPHOBIC CORE

Design parameters that affect the hydrophobic core (*a* and *d* positions) involve the placement of amino acids with different levels of hydrophobicity and the insertion of polar amino acids in the CC interface. Considering that hydrophobic interactions are the main driving force for CC stabilization, a major focus has been placed on this design feature. One key aspect that has been addressed is why β-branched hydrophobic amino acids (Ile, Val) are mostly observed in the *a* position while the *d* positions frequently contain Leu.

When exchanging these amino acids in a GCN4 homodimer, it has been observed that Ile or Val are more stabilizing than Leu when placed in *a* positions. Furthermore, *a* positions are more tolerant to different hydrophobic amino acids than *d* positions. In contrast, according to the PDB, more than 50% of the *d* positions are occupied with Leu in dimeric CCs. The overall stability of a CC thus depends on the overall hydrophobicity of the amino acids in the *a* and *d* positions as well as the conformation adopted by their different side chains (i.e. their packing in the hydrophobic core) [52].

A more systematic study was performed using a newly designed heterodimer [53], which contained Val in *a* positions (except Asn in the third heptad) and Leu in all *d* positions. In this heterodimer (named *EK*), one peptide contained Lys in all *e* and *g* positions, whereas the second peptide contained Glu. To investigate the role of Leu, an Ala screening was done in all *d* positions. All mutants showed a lower thermodynamic stability with a decreased melting temperature (T_m) of 15-20 °C with respect to the control. These results again highlight the importance of hydrophobic interactions at the CC interface, showing that the shorter side chain of Ala causes destabilization. Using the same model system, the placement of Val and Ile in the *a* position was investigated. It was shown that replacing Val with Ile resulted in an increase of the thermodynamic stability by 0.47 kcal mol^{-1} per substitution [45].

The packing of the side chains does not only determine the stability of the CC. It also affects the oligomerization state. In general, the sequence pattern EHAAHKX (H = Ile, Val, Leu, Met) facilitates CC formation; however, different combinations of these hydrophobic amino acids give rise to different packing geometries, which lead to different oligomerization states (Table 3). For example, Harbury *et al.* modified the hydrophobic core of the well-established GCN4 leucine zipper, using different amino acid combinations [54]: Ile@*a* and Leu@*d* shows dimers, Ile (both @*a* and @*d*) shows trimers, and Leu@*a* and Ile@*d* shows tetramers. The use of Val resulted in mixed oligomerization states. To form pentamers and higher order oligomers, also the *e* and *g* positions need to contain hydrophobic residues [8].

TABLE 3 – Coiled Coil oligomerization state. Examples of how the four most common substitutions in the hydrophobic core (*a* and *d* position) affect the oligomerization state of Coiled Coils. Each of the Coiled Coils shown has a different sequence in the *b*, *c*, *e*, *f* and *g* positions.

		d position			
		Ile	Val	Leu	Met
a position	Ile	trimer [42] trimer [54] trimer [8]		dimer[42] dimer [54] dimer [8]	
	Val			dimer [55] dimer, trimer [54] dimer, trimer [56] trimer [46]	
	Leu	tetramer[42] tetramer [54] tetramer [8]	trimer [54]	trimer [54]	
	Met			dimer [55]	

In some cases, the same sequence can form multiple oligomerization states or assemble in a different register. The specificity of a dimeric CC assembly is usually increased when

the CC contains an **Asn-Asn interaction in the *a* positions of a central heptad**. This Asn-Asn pair is also present in the GCN4 structure and its importance was already recognized when the GCN4 structure was first published [51]. Even though Asn incorporation is generally destabilizing [57] it is now frequently included in *de novo* designed dimeric CCs to control their oligomerization state. More recently, it was found that the presence of Asn in the *a* or *d* position can also change the CC oligomerization state (dimers if Asn@*a* position and trimers if Asn@*d* position) [43]. Lastly, a specifically placed Asn-Asn interaction can also ensure a specific helix orientation (parallel or antiparallel) independent of the other amino acids located at the dimer interface [58].

4.2.2.   IONIC INTERACTIONS

In addition to hydrophobic interactions, also ionic interactions (or *salt bridges*) need to be considered when designing a CC sequence. These ionic interactions are usually formed between negatively (Glu) and positively charged (Lys, Arg) amino acids. The location of these charged amino acids determines if inter- or intrahelical ionic interactions are formed (Figure 6). **Interhelical ionic interactions** exist between two charged residues positioned in the *g* position of one helix and the *e* position of the following heptad in the other helix (i, i+5). These interactions thus play an important role in the formation and stabilization of the supramolecular structure. The removal of charged amino acids at the *e* and *g* positions in the GCN4 leucine zipper leads to a decrease in thermodynamic stability and loss of dimer structure [59]. **Intrahelical ionic interactions** primarily stabilize individual α-helices. Amino acids forming intrahelical interactions are positioned in a distance of (i, i+3) or (i, i+4), with (i, i+4) positions possessing a larger stabilizing effect [60, 61]. Intrahelical interactions do not only contribute to helix stability, they also affect folding rates [62]. Glu-Arg pairs initiate folding highly efficiently as they possess the longest side chains with the largest conformational space in comparison to Asp-Arg and Glu-Lys. Substituting two intrahelical ionic interactions with Ala in the GCN4 leucine zipper was shown to destabilize the structure [63].
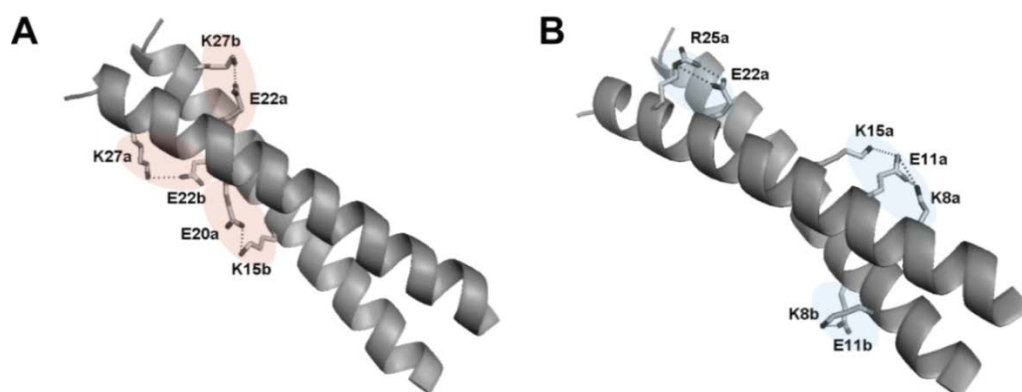
FIGURE 5 – Ionic interactions in the GCN4 leucine zipper. A) Interhelical ionic interactions. B) Intrahelical ionic interactions. The designation a and b refers to the individual helices forming the homodimer. [Adapted with permission from Elsevier: Electrostatic Contributions to the Stability of the GCN4 Leucine Zipper Structure, W. M. Matousek, B. Ciani, C. A. Fitch, B. Garcia-Moreno, R. A. Kammerer, A. T. Alexandrescu (Copyright © 2007 Elsevier Ltd. All rights reserved [64])

Ionic interactions are further known to determine CC topology. Most importantly, interhelical ionic interactions control the assembly into homo- or hetero-oligomers. This is most easily achieved when designing one helix that carries only positively charged amino acids in positions *e* and *g* while its counterpart is negatively charged.

Ionic interactions are thus key for designing **orthogonal Coiled Coils** (i.e. sets of monomers, which form specific CCs in the presence of others). Orthogonal, self-sorting CCs are powerful building blocks in applications, such as CC-based biomaterials [65, 66] or nanostructures [67-69]. Orthogonal designs rely on carefully positioned attractive and repulsive residues [70] along with specific amino acids in the CC interface, which allow desired pairs to form while others (the so-called *off-targets*) are weakened as a result of intermolecular repulsion.

Ultimately, to control the formation of ionic interactions, also the solvent pH plays an important role [71]. It has been shown that the protonation states of the charged amino acids affect CC topology. pH changes can, for example, alter the oligomerization state (dimers/trimers vs. pentamers) [72] or fully disrupt the supercoil structure [73]. Also, the reorganization into amyloid structures can be induced by a pH change [74]. Lastly, it should be noted that the helical propensity contribution of each amino acid needs to be considered when considering the introduction of charged amino acids. The stabilizing effect of ionic interactions may be counterbalanced by a decrease in helix propensity [75], another important factor of CC stability that will be discussed in more detail in the following.

4.2.3. SOLVENT-EXPOSED SURFACE AND HELIX PROPENSITY

The solvent-exposed positions *b, c,* and *f* can be utilized for introducing intrahelical ionic interactions as described above. In addition, they allow for altering the helix propensity of the individual helices, which represents an important contribution to the overall stability of the superhelical structure. The previously described EHAAHKX heptad model contains Ala in positions *b* and *c*. Ala provides great stability to the individual helices as it is the amino acid with the highest helix propensity [76]. Table 4 shows a ranking of helix propensities, defining the energetic contribution of Ala as 0 kcal mol^{-1} and Gly as 1 kcal mol^{-1} (with Gly being the amino acid with the lowest helix propensity, except Pro). This energetic difference originates from the additional methyl group in the Ala side chain, which reduces the available conformational space for the Φ and Ψ angles in the peptide backbone. In the *f* position, Gln or Lys are frequently used as they combine high helix propensity with water solubility [42].

Litowski *et al.* [45] described a decrease in CC stability of 0.41-0.45 kcal mol^{-1} when Ala was replaced with Ser in all heptads of a heterodimeric CC. Ser has a lower helix propensity since the OH-group in its side chain competes for water molecules with the peptide backbone. The helix propensities of individual amino acids synergistically determine the stability of a helix [77]. This overall helix propensity can be predicted with online bioinformatics tools like AGADIR [78], which displays a score depending on the amino acid

and its specific position in the sequence: the same amino acid does not contribute in the same manner when located in the center or in the terminal parts of a peptide due to end fraying.

When redesigning the thermodynamic stability of a CC, both helix propensity and intrahelical ionic interactions need to be considered since both modifications are usually introduced in the *b*, *c* and *f* positions. In some designs, a destabilization of the CC has occurred when ionic interactions were removed with the goal of inserting amino acids with a higher helix propensity. On the other hand, Drobnak *et al.* [79] introduced intrahelical ionic interactions with (i, i+3) and (i, i+4) spacing in the heptads with the highest helix propensity, thereby increasing the thermodynamic stability by 20 °C. This shows that intrahelical ionic interactions can also compensate for a loss of helix propensity.

TABLE 4 – Helix propensities of individual amino acids, based on experimental studies in peptides/proteins. The energetic contribution of Ala is set to 0 kcal mol^{-1} and Gly to 1 kcal mol^{-1}. [Adapted with permission from Elsevier: A Helix Propensity Scale Based on Experimental Studies of Peptides and Proteins, C. N. Pace, J. M. Scholtz (Copyright © 1998 The Biophysical Society. Published by Elsevier Inc. All rights reserved.[76])

Amino acid	Helix propensity (kcal mol^{-1})
Ala	0.00
Glu^a	0.16
Leu	0.21
Met	0.24
Arg$^+$	0.21
Lys$^+$	0.26
Gln	0.39
Glu$^-$	0.40
Ile	0.41
Asp^o	0.43
Ser	0.50
Trp	0.49
Tyr	0.53
Phe	0.54
Val	0.61
Thr	0.66
His^a	0.56
His$^+$	0.66
Cys	0.68
Asn	0.65
Asp$^-$	0.69
Gly	1.00
Pro	3.16

4.2.4. OTHER DESIGN PARAMETERS

The above design parameters have usually been tested for dimeric parallel CCs and are now available for rationally predicting the properties of these structures based on their primary amino acid sequence. They have been implemented in a number of prediction programs, such as SOCKET [16], or structural design programs like CCBuilder [13] or Rosetta [80]. More recently, higher order structures and antiparallel CCs have been designed as well.

Higher order oligomers possess a different hydrophobic core packing, and the specific placement of Ile, Leu, Val and others [81] in the *a* and *d* positions is known to control the formation of dimers, trimers and tetramers (see also 4.2.1). Obtaining pentamers, hexamers and heptamers is only possible when traditional polar positions are occupied with hydrophobic amino acids for the extension of the hydrophobic interface [82]. With this approach, α-helical barrels (αHBs) made from 5, 6 or 7 helices have been engineered. These αHBs have later been equipped with additional functions. For example, they are able to accommodate and discriminate various lipophilic molecules in their hydrophobic core with different affinities [83] and, moreover, hydrolytic activity has been engineered into their core [84].

With the rise of prediction programs and databases like SYNZIP [85], also **antiparallel Coiled Coils** have been investigated in more detail and several *de novo* designs exist. For instance, Negron *et al*. developed a computational method for the prediction of CC orientation [86], which was utilized for the design of orthogonal antiparallel homodimers. These antiparallel CCs were then used as engineered building blocks for the specific assembly of protein-origami nanocages [87].

Even though large progress has been made towards *de novo* protein and peptide design, it has been recognized that the use of only natural amino acids presents an obvious limitation. This is even more critical when the aim is to create CCs, where the residue types are restricted to specific positions in the canonical heptad pattern. To overcome the limitations imposed by the amount of possible amino acid combinations, introducing **non-natural elements into the amino acid sequence** has emerged as a new strategy. This strategy opens up the sequence space and provides new possibilities for manipulating hydrophobicity and helix stability.

Frequently used non-natural modifications include the introduction of synthetic bridges or *staples*. These constrain and stabilize the helical structure thereby increasing the thermodynamic stability of the CC [88]. Hydrophobic core modifications include the insertion of non-canonical amino acids, such as **fluorine-modified amino acids** [89, 90] or cyclohexylalanine. The latter is particularly interesting, as it has been used to increase the specificity of heterotrimeric assemblies [91].

In general, in the area of protein design both natural and non-natural amino acid substitutions have been successfully applied to improve protein properties, e.g. in the areas

of biomedicine and pharmacology. However, these substitutions are usually made with the goal of improving protein stability or of increasing the affinity or specificity of protein-protein interactions. Only very recently, attempts have been made to control the mechanical properties of proteins. Understanding how to use these strategies for designing proteins with controlled mechanical properties is of particular importance for CCs, which are known to possess mechanical function in Nature.

4.3.   MECHANICAL ASPECTS OF COILED COIL DESIGN

To understand the **mechanical properties of CCs**, the general response of proteins to force needs to be considered along with specific molecular interactions that define the CC. The native or folded state of a protein resides at its minimum of Gibbs free energy. The energy difference between the folded (or native) (N) and the unfolded (U) state ΔG_{N-U} defines its thermodynamic stability. In a two-state energy landscape model (folded/unfolded), force can act as a *denaturant* directly on the reaction coordinate of the protein, forcing the protein to overcome the energy barrier (ΔG_{N-TS}), which separates the folded from the unfolded state. Force tilts the energy landscape, thereby lowering ΔG_{N-TS} and increasing the unfolding rate [92] (Figure 8). The same principle applies to receptor-ligand interactions, or more specifically to CC oligomers.
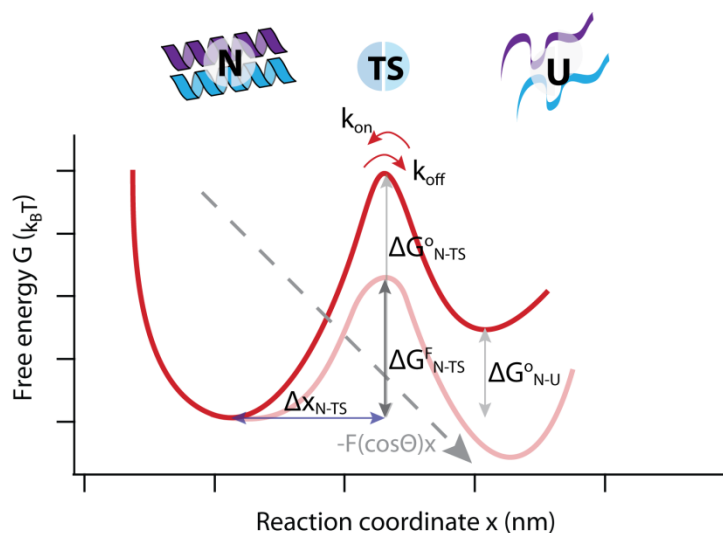
FIGURE 6 – Energy landscape of a model Coiled Coil. The force acting on the CC tilts the energy landscape, thereby lowering the energy barrier (ΔG_{N-TS}) and increasing the dissociation rate of the oligomer (k_{off}).

The molecular interactions that define the folded state of proteins include hydrogen bonds, ionic and polar as well as hydrophobic interactions. These interactions stabilize secondary structure elements as well as the overall fold. The mechanics of protein unfolding is mostly determined by the specific arrangement of secondary structure elements [92-94]. In general, β-sheets (e.g. in immunoglobulin domains) unfold at higher forces than α-helical assemblies (e.g. the spectrin domain) The loading geometry of the hydrogen bond network

contributes to these differences [95]. These differences cannot be observed in the thermodynamic stability experiments, being non-dependent of loading.

In the specific case of CCs, hydrogen bonds and hydrophobic interactions are the key interactions that are expected to contribute to the mechanical stability of these structures. Hydrogen bonds are aligned parallel to the helical axis whereas hydrophobic interactions are oriented perpendicularly. It can thus be expected that the **orientation** of a CC relative to the force vector affects its mechanical stability. The orientation, for example, depends on the exact residue where the force is applied [96, 97] and on the pulling geometry (tensile, shear or unzip) [98, 99] (Figure 9, Table 5).
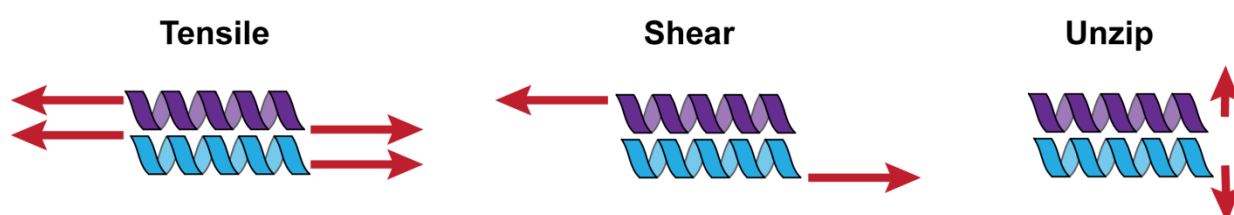
FIGURE 7 – Pulling geometries in Coiled Coil models. The arrows reflect the direction of the force vector.

TABLE 5 – Mechanical stability of Coiled Coils in different pulling geometries. *The pulling speed or strain rate is shown, if data is provided. If not, the plateau forces are shown.

Protein	Pulling geometry	SMFS method	Force in pN (retract speed in nm s^{-1} or rate in s^{-1})*	Ref.
α-catenin	Tensile	Magnetic tweezers	5 pN (Phase I) 10-15 pN (Phase II)	[100]
Spectrin	Tensile	AFM	32 pN (600 nm s^{-1})	[101]
Myosin	Tensile	AFM	20-25 pN (40-130 nm s^{-1})	[28]
Fibrinogen trimer	Tensile	AFM	94 pN (0.03 s^{-1})	[102]
LZ10 homodimer	Unzip Tensile	AFM	10 pN 25 pN	[103]
Calmodulin DomC	Unzip	AFM	18 pN (600 nm s^{-1})	[104]
GCN4	Unzip	Optical tweezers	8-15 pN (500 nm s^{-1})	[105]
Kinesin neck	Unzip	AFM	11 pN (150 nm s^{-1})	[106]
LZ26 homodimer	Unzip	AFM	~12 pN (150-760 nm s^{-1})	[98]
Talin	Shear	AFM	12 pN (2.7 s^{-1})	[107]
A$_4$B$_4$ heterodimer	Shear	AFM	35-50 pN (5-500 nm s^{-1})	[108]
A$_4$B$_3$ heterodimer	Shear	AFM	25-45 pN (5-500 nm s^{-1})	[108]

When pulled along their axis (tensile or shear geometry), CCs show a 3-phase response to the applied force: In the first phase, the CC extends linearly with the applied force. In the second phase, hydrogen bonds break sequentially at an almost constant force. Hydrogen bonds start breaking at the ends where the mechanical load is applied [108]. In this phase, new hydrogen bonds may form between the CC chains, leading to a β -sheet structure (α-β transition). For instance, this has been observed for myosin at extensions >30 nm [109]. In phase III, the force rises again as the resulting structure is extended further [29, 102, 110]. For short CCs pulled in shear geometry, CC chain separation (i.e. dissociation) may occur before phase III is reached [108].

For heterodimeric CCs with a length of ≤4 heptads, Goktas *et al.* suggested that chain separation involves three time-scale dependent processes [108]: at fast retract speeds, helix uncoiling propagates from the ends where the force is applied until the helical structure is lost and the chains separate. In an intermediate regime, uncoiling-assisted sliding facilitates a relative displacement of the helices. At slow retract speeds, uncoiling-assisted dissociation occurs once a critical amount of helical structure is uncoiled.

In a similar manner, unzipping a CC requires the partial unfolding of the helices prior to the loss of hydrophobic contacts and final chain separation. In this case, the force propagates in a perpendicular direction to the helix axis (Figure 7), therefore the hydrogen bonds are not aligned with the direction of the force vector, while the hydrophobic contacts are expected to detach in a parallel manner [111].

Overall, considering the different pulling geometries and retract speeds, the forces required to break a CC range from 5-94 pN. Although sequence and length vary, a tendency can be observed when comparing the pulling geometries: tensile and shear geometries require higher forces than CC unzipping (Table 5). To fully understand the mechanistic response of CCs to an applied force, however, it is necessary to consider also the CC sequence and to establish a relationship between sequence, structure and mechanics. Only when taking into account all of the previously discussed parameters will it be possible to **predict both the thermodynamic and mechanical stability of CCs** and to use them as building blocks in different applications.

4.4.   APPLICATIONS OF SYNTHETIC COILED COIL BUILDING BLOCKS

Once the sequence-structure-mechanics relationship is understood and CCs with defined mechanical properties can be designed *de novo*, what can we "construct" with these mechanical building blocks? CCs are already used in a wide range of different applications, ranging from protein-based biomaterials to biosensors and protein-protein interactions [112] in drug development. Here, a special emphasis will be placed on the use of CC building blocks in applications where their mechanical properties are important (Figure 8).
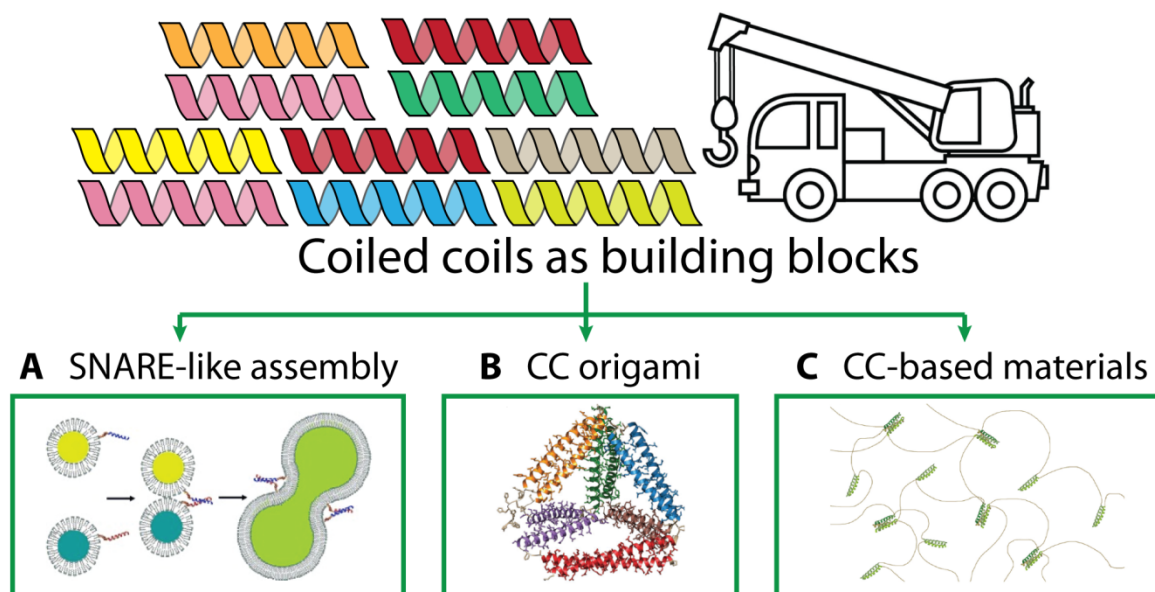
FIGURE 8 – Examples of Coiled Coil applications. A) CC-based mimics of SNARE complexes [Reprinted with permission from Angewandte Chemie Int. Ed.: A reduced SNARE model for membrane fusion, H. R. Marsden, N. A. Elbers, P. H. Bomans, et al. (copyright © 2009, John Wiley and sons [113])]. B) CC-based protein origami. In the examples shown orthogonal CCs are combined in different orientations to form a tetrahedron [Reprinted with permission from Nature Biotechnology: Design of coiled-coil protein-origami cages that self-assemble in vitro and in vivo, A. Ljubetič, F. Lapenta, H. Gradišar, I. Drobnak, J. Aupič et al. (copyright © 2017, Springer Nature[114])]. C) CCs act as physical crosslinks in PEG-based hydrogels [Reprinted with permission from Biomacromolecules: Self-assembling peptide-polymer hydrogels designed from the Coiled Coil region of fibrin, P. Jing, Jai S. Rudra, A. B. Herr, et al (copyright © 2008, American Chemical Society[115])].

The *EK* heterodimer developed by Hodges *et al.* [45] can be used for protein immobilization in **biosensor applications** and as an **affinity tag for protein purification,** in a similar manner as Ni^{2+}-NTA (nitrilotriacetic acid) [116]. More interestingly, it is also used for the development of **SNARE-inspired methods** for membrane fusion in synthetic vesicles [113]. SNARE (Soluble NSF Attachment protein REceptor) proteins are natural CCs and are involved in the recognition of transport vesicles to initiate membrane fusion. The resultant SNARE complex is a four-helix bundle, assembled in a zipper fashion. SNARE-mediated membrane fusion has been mimicked using newly designed CCs. These are able to initiate the fusion of artificial lipid vesicles, thereby facilitating their use as drug carriers. Different systems have been designed for this purpose, using both zipping and shear geometries. No difference in the efficiency of the fusion process was observed, suggesting that the fusion process is not sensitive to the mechanical stability of the CC or that the parameters determining the fusion process are not yet fully understood [117].

The ability to design orthogonal CC dimers allowed for building more complex supramolecular assemblies, the so-called **protein origami structures**, which were inspired by the success of DNA origami [118]. All parameters of CC design [68, 119] can be used for the construction of such structures: parallel/antiparallel orientation, oligomerization, zipping/shear geometry, etc. [120] Various different structures have been constructed, including a tetrahedron, where six CC pairs interact in parallel and antiparallel orientations [87], a four-sided pyramid and a triangular prism [114]. These nanocages self-assemble

from just one polypeptide chain, both *in vitro* and *in vivo*. They allow for the development of scaffolds for peptidic vaccines or as drug carriers (ligand binding can be accommodated in the interior of the nanocage cavity). The use of protein-origami is further allowing the development of protein nanomachines, sensors and functional biomaterials [114], applications where the mechanical properties of the overall assembly are crucial.

In Nature, CCs frequently self-assemble into hierarchical structures, as it is the case for intermediate filaments for example. This process has been mimicked in synthetic CCs and 2D nanostructures. For example, fibers and hydrogels have been assembled from CC building blocks [32, 121-123]. Of particular interest are hydrogels, as they can be used as synthetic mimics of the cytoskeleton and the ECM [4, 124]. In addition to purely CC-based materials, CC building blocks can also be used as physical crosslinks in **polymer-based hydrogels**. For example, the CC of the ECM protein fibrinogen was prepared synthetically and used to crosslink the polymer poly(ethylene glycol) (PEG), resulting in a well-characterized biomimetic material [115]. Whereas the above example uses a trimeric CC in combination with linear PEG, also dimeric CCs can be combined with branched, star-shaped PEG [66]. The area of peptide-based ECM-mimetic materials is quickly expanding [125] and *de novo* designed CCs with defined thermodynamic and mechanical properties are excellent building blocks. The modulation of their properties is expected to alter the stiffness and viscoelasticity of the resulting materials. This, in turn, is expected to influence mechanotransduction cascades of the cells cultured in these hydrogels, thus affecting processes such as cell migration or differentiation.

5. AIMS

In Nature, CCs form essential parts of structural proteins in the cytoskeleton and the ECM. CC-based proteins further play important roles in mechanobiochemical processes, such as cell migration, differentiation and growth [39]. In the past years, research has focused on identifying parameters that determine CC structure as well as **thermodynamic and kinetic stability**. The main driving force for CC formation is the burial of the hydrophobic side chains at the interface [45, 46]. Additional parameters, which stabilize the folded CC, are ionic interactions [126] and the helix propensity of the individual helices [127]. From a thermodynamic and kinetic point of view, CC chain separation is a cooperative two-state process, where helix unfolding and dissociation are coupled [128].

Studies aimed at understanding the **mechanical stability** of CCs suggest a different and less cooperative chain separation pathway. This pathway also depends on the direction of the applied force, i.e. the pulling geometry. When shearing a CC, the helix stabilizing hydrogen bonds are aligned parallel to the force vector [108]. As a result, the CC responds to the applied force with uncoiling of the individual helices at the points of force application, suggesting that helix stabilizing hydrogen bonds rupture before hydrophobic interactions are broken. It is hence helix stability that determines the overall mechanical stability of a CC. Contrarily, when unzipping a CC [129], the force vector is initially aligned parallel to the hydrophobic interactions and perpendicular to the hydrogen bonds.

Mechanically-induced CC chain separation is thus expected to depend on the pulling geometry and does not share the same pathway as the thermodynamic process. Moreover, the influence of the well-known design parameters (hydrophobic and ionic interactions and helix propensity) on the mechanical stability of CCs is not known. In this work, I will focus on understating the effect of these parameters with the aim of establishing the sequence-structure-mechanics relationship of heterodimeric CCs. I will further compare the thermodynamic and mechanical stabilities of a series of CCs to understand if and how they are correlated. Specifically, the following questions will be addressed in this work:

⇒ **How do the basic design parameters (hydrophobic interactions and helix propensity) affect CC mechanics?**

In the first part, I aim to establish the sequence-structure-mechanics relationship of a 4-heptad heterodimer, using canonical modifications in the amino acid sequence. Specifically, I am to investigate the effect of modifications at the hydrophobic interface and in the overall helix propensity. I will substitute Ile for Val in the *a* position. Val lacks one methyl group in comparison to Ile. It is thus less hydrophobic and packs less tightly in the hydrophobic core. I will further replace Ala with Ser in the *b* position to lower the helix propensity of the individual helices. Both modifications are known to destabilize the CC thermodynamically. Here, I will focus on the effect of these substitutions on the mechanical stability when loading the CC in the shear geometry. The results are expected to provide

insights into how specific design features alter CC mechanics and how the thermodynamic stability correlates with the mechanical stability of CCs.

⇒ **What is the effect of the pulling geometry on the mechanical stability of the same CC sequence?**

Previous studies have provided a first indication that the mechanical stability (i.e. the force required for chain separation) is lower in the unzip than in the shear geometry; however, this has never been tested with one and the same sequence. A 4-heptad heterodimer with a given thermodynamic stability can be mechanically loaded in 4 different ways: 2 shear geometries and 2 unzip geometries (see Figure 18 in the experimental design section). Here, I will investigate if exchanging the points of force application in the shear geometry affects CC mechanical stability. In addition, I will compare the two shear geometries to one unzip geometry. The comparison of these three systems will identify if strand separation follows different mechanical pathways and provide insights into which interactions will be disrupted in the CC.

⇒ **Is it possible to mechanically stabilize the CC when introducing artificial helix stabilizing interactions?**

A small number of experiments and molecular dynamics simulations [130] have already pointed towards helix stability as one of the key parameters defining the response of CCs to shear forces. Here, I aim to answer the question if and how a CC can be stabilized against force-induced unfolding. For this purpose, I will use additional interactions that stabilize and constrain the structure of the individual helices. Specifically, I will insert dynamic and covalent *staples* into the terminal heptads where the force is applied. These *staples* will join two amino acid side chains in positions (i, i+4) on the solvent-exposed surface of the CC.

It has already been shown that the use of dynamic metal coordinating *staples* leads to a thermodynamic and mechanical stabilization of a CC heterodimer. Here, I build on this strategy and compare these dynamic *staples* with an irreversible, covalent staple (lactam bridge). This staple will be inserted at the force application point of the less helical monomer with the goal of stabilizing the weakest part of the CC. In addition, the staple will be inserted at the same terminus in the complementary helix, which is not directly loaded. This will allow for testing if helix stabilization is transmitted through the hydrophobic core. The comparison between different staple positions and its dynamic behavior will provide detailed insights into the chain separation mechanism and show possible routes towards tuning the CC mechanical response for applications.

⇒ **Is it possible to enhance hydrophobicity at the CC interface with non-natural, fluorinated amino acids?**

It is known from a series of thermodynamic studies that an increase of the hydrophobicity at the interface leads to an increase in the CC stability. This has been shown both for canonical hydrophobic amino acid substitutions (e.g. Ile vs. Val), but also for non-

canonical amino acids (e.g. fluorinated amino acids). Even though fluorinated amino acids generally increase the thermodynamic stability, also destabilization has been observed in some cases, depending on the type and position of the fluorinated amino acid(s). Here, I will substitute one Leu in the *d* position of one helix with trifluoroethylglycine (TfeGly). Fluorine-hydrogen substitutions in the side chain increase the hydrophobicity while conserving the size of the side chain. The insertion of this fluorinated amino acid will thus allow for testing if this increased hydrophobicity affects the mechanical stability of the CC and if additional interface packing effects influence the chain separation mechanism.

To fully understand the influence of these modifications on the mechanical properties of CCs, a comparison between their thermodynamic and mechanical stabilities is essential. For this purpose, all rationally designed CC will first be characterized thermodynamically using Circular Dichroism (CD) spectroscopy. I will apply temperature as a denaturant to obtain the melting temperature (T_m) as well as the free energy difference between the folded and the unfolded state (ΔG_{N-U}). For the mechanical characterization, atomic force microscope-based single molecule force spectroscopy (AFM-SMFS) will be used. AFM-based SMFS allows for stretching the CCs of interest in the shear geometry with a steadily increasing force (constant cantilever retract speed) until the CC ruptures (chain separation). This type of experiment allows for obtaining kinetic parameters, which describe essential energy landscape properties of the CCs, namely the force-free dissociation rate (k_{off}) and the distance to the transition state (Δx_{N-TS}).

Answering the above questions will provide detailed insights into the key parameters, which define the mechanical stability of CCs. Most importantly, once the sequence-structure-mechanics relationship is established, synthetic CCs with a pre-defined mechanical stability can be designed *de novo*, just as is the case for CCs with a pre-defined thermodynamic stability. This will open up a number of applications, which require CCs as mechanical building blocks, as mentioned in the former Introduction section. One highly interesting application is the use of CCs as physical crosslinks in ECM-inspired biomaterials. The use of mechanically characterized crosslinks will not only allow for tuning mechanical material properties but also for the synthesis of self-reporting materials, which contain CCs as molecular force sensors (MFSs) [131]. Towards this ultimate goal, the work carried out in this thesis **creates a library of CCs with different mechanical properties that can serve as mechanosensitive crosslinks in hydrogel-based materials**.

6. MATERIALS AND METHODS

6.1. MATERIALS

6.1.1. PEPTIDES

The peptides were purchased from Centic Biotec (Heidelberg, Germany) or synthesized by our collaborators using solid-phase peptide synthesis (SPPS) (*Prof. David Fairlie, University of Queensland, Australia* and *Prof. Beate Koksch, Freie Universität Berlin, Germany*). $A4_{H-2}$ was synthesized in house (Tribute; Gyros Protein Technologies, USA), following a standard Fmoc-protocol using ChemMatrix resin (Merck, Germany) and HCTU (Merck, Germany) as coupling reagent. Acidic cleavage from the resin was achieved using a mixture of trifluoroacetic acid (TFA), triisopropylsilane (TIS), 1,2-ethanedithiol (EDT) and water in a ratio of 92.5:2.5:2.5:2.5. The peptide was purified with high-performance liquid chromatography (HPLC), using a C_{18}-column (Nucleodur® 300-5C18ec, Macherey-Nagel, Germany). A linear gradient from 20-100 % acetonitrile + 0.1% TFA was used at a flow rate of 25 mL min^{-1}. The correct sequence of the peptide was confirmed with mass spectrometry (MALDI-TOF; Bruker, USA).

The sequence, origin, molecular weight and purity of each peptide is summarized in Table A1 in the appendix. HPLC chromatograms and MALDI-TOF spectra of $A4_{H-2}$ are shown in Figures A1 and A2.

The peptide concentrations were measured using the UV absorbance of the peptides at 280 nm. The respective extinction coefficients were calculated using ProtParam [132] accessed via the ExPASy site. The concentration measurements were performed with a Cytation 5 microplate reader (BioTek, USA), using the Take3 micro-volume plate.

6.1.2. BUFFERS

TABLE 6 – Composition of the buffers used in the different experiments.

Name	Composition		
PBS	10	mM	Na_2HPO_4 pH~7.4
	2	mM	KH_2PO_4
	137	mM	NaCl
	2.7	mM	KCl
Coupling buffer	50	mM	Na_2HPO_4 pH~7.2
	50	mM	NaCl
	10	mM	EDTA
Borate buffer	50	mM	$H_3BO_3/Na_2B_4O_7$ pH~8.5
PIPPS-BS	10	mM	PIPPS pH~7.4
	137	mM	NaCl
	2.7	mM	KCl
PIPPS-BS + Ni^{2+}	10	mM	PIPPS pH~7.4
	137	mM	NaCl
	2.7	mM	KCl
	1	mM	$NiCl_2$ (in AFM experiments)
	150	μM	$NiCl_2$ (in CD experiments)
Phosphate buffers to test ionic interactions	10	mM	Na_2HPO_4 pH~7.4
	10	mM	Na_2HPO_4 pH~7.4
	150	mM	NaCl
	10	mM	Na_2HPO_4 pH~7.4
	5	M	NaCl
	10	mM	Na_2HPO_4 pH~7.4
	150	mM	$NaClO_4$
	10	mM	Na_2HPO_4 pH~7.4
	5	M	$NaClO_4$
	10	mM	Na_2HPO_4 pH~2.5
	10	mM	Na_2HPO_4 pH~2.5
	150	mM	NaCl
	10	mM	Na_2HPO_4 pH~2.5
	5	M	NaCl
	10	mM	Na_2HPO_4 pH~2.5
	150	mM	$NaClO_4$
	10	mM	Na_2HPO_4 pH~2.5
	5	M	$NaClO_4$

All experiments were performed in the same manner for the different sequences investigated, except stated otherwise. The two main methods will be introduced in detail in the following: **Circular Dichroism (CD) spectroscopy**, which gives information about the secondary structure and thermodynamic stability of the peptides, and **atomic force microscope-based single molecule force spectroscopy (AFM-SMFS)**, which was used for the mechanical characterization of the CCs.

6.2.1.   CIRCULAR DICHROISM SPECTROSCOPY

Introduction

Circular Dichroism (CD) spectroscopy is a technique that provides structural information about proteins and peptides in solution. Just as other spectroscopy techniques, CD measures the absorption of electromagnetic radiation in the sample. Therefore, CD follows the Lambert-Beer law, which describes how much light the sample absorbs at a given wavelength:

(1)
$$A = \ln\left(\frac{I}{I_o}\right) = -\varepsilon l c$$

where A is the absorption, I_o is the incident intensity, I is the intensity of the transmitted light, ε is the molar extinction coefficient, l is the path length and c the molar concentration of the sample.
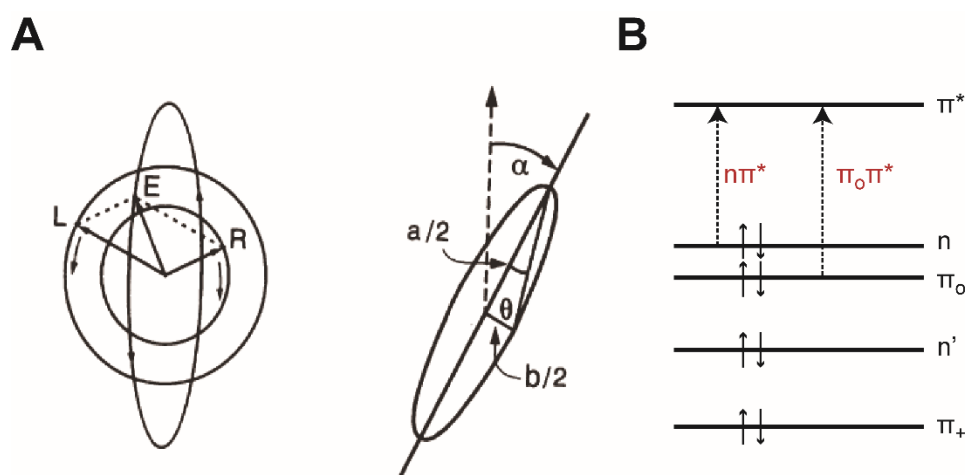

FIGURE 9 – Principle of Circular Dichroism (CD) spectroscopy. A) Elliptically polarized light (right) formed via the superposition of right-handed and left-handed polarized light (left). Ellipticity is described, using the tangent of the Θ angle of the formed ellipse. The α angle refers to the *optical rotation*. It represents the angle between the major axis of the ellipse and the initial plane of the polarized light as depicted on the left. B) Electronic transitions of the amide bond. The $\pi_o\pi^*$ transition is observed in the wavelength range of ~190 nm and the $n\pi^*$ transition in the range of ~222 nm, which gives the characteristic α-helical pattern in the CD spectrum. [Reprinted with permission from Springer Nature: Theory of Circular Dichroism of Proteins, R. W. Woody [Copyright © 1996, Springer Science Business Media New York [133]]

CD refers to the differential absorption of right-handed (R) and left-handed (L) circularly polarized light. When both components are absorbed to a different extent when passing through the sample, the resulting radiation has elliptical polarization. This can only occur when the molecules in the sample are *chiral* therefore showing different absorption of the R and L circularly polarized light [133]. In the case of proteins and peptides, chirality is shown in the amide bonds (i.e. chiral centers), which are used as the chromophores in this study. The mixing of the spectroscopic signatures of the n-$\pi^\star$ and π_0-$\pi^\star$ electronic transitions of the amide (Figure 9B, and more to be explained below) determines the final structure displayed in the CD spectrum (α-helix, β-sheet, random coil, etc.).

The previous Lambert-Beer equation (eq. 1) only referred to one of the circularly polarized components. Therefore, for quantifying the CD effect, the difference in absorbance of the R and L components needs to be determined (ΔA). ΔA refers to the subtraction of both polarized components A_R and A_L, leading to the following equation:

(2) $$\Delta A = A_L - A_R = \varepsilon_L lc - \varepsilon_R lc = \Delta\varepsilon lc$$

As stated before, proteins and peptides rotate circularly-polarized light in a specific and distinct manner. The resulting difference in the transmission of polarized light through the sample is reported in terms of ellipticity (Θ, $\Theta = \tan^{-1}(b/a)$, where a and b are both the axes of the ellipse, Figure 9). The ellipticity value is given in radians, although it can be converted into degrees, using 32.98 ΔA. Following the Lambert-Beer law, the CD signal Θ is proportional to the concentration and path length of the sample. To obtain sample specific information, the result is usually given as the *molar ellipticity* (*ME*, traditionally, deg cm^2 dmol^{-1}), which is defined as follows:

(3) $$ME = 100\frac{\theta}{cl} = 3298\,\Delta\varepsilon$$

Proteins and peptides absorb light in the far (160-250 nm) and near UV (260-320 nm) regions. In the far UV region, the chromophore is the peptide bond. This yields specific and characteristic CD spectra, which report on the secondary structure content of the sample. In the near UV region, the different aromatic amino acids (Trp at 290 nm, Phe at 255-270 nm, Tyr at 275-282 nm) may give rise to specific CD signals, if they experience a chiral environment. In addition, other chromophores (e.g. ligands and cofactors) can bind to a chiral environment originating chirality from the binding of a molecule to a chiral center in a protein or from the protein/peptide structure [134].
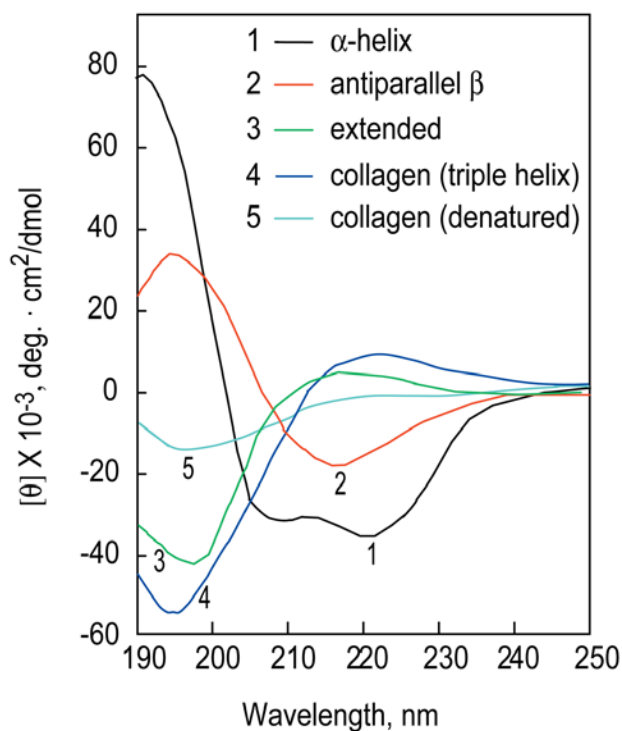
FIGURE 10 – Far UV CD spectra, showing different secondary structures. 1, 2 and 3 show poly-Lys displaying different secondary structures at different pH values. 4 and 5 show plancental collagen in its folded and denatured form. (Reprinted with permission from Springer Nature: Using circular dichroism collected as a function of temperature to determine the thermodynamics of protein unfolding and binding interactions, N. J. Greenfield [Copyright © 2006, Springer Nature [135])

CD spectra consist of different bands, representing the electronic transitions from the ground state to an electronically excited state in the amide orbitals. As shown in Figure 9B and Figure 10 for an α-helix, the peak at ~222 nm corresponds to the n-π* transition in the peptide bond, while the ~190 nm maximum and ~208 nm minimum corresponds to a series of overlapping π_o-π* transitions. In the case of a β-sheet, the distinct spectrum shows the n-π* transition at 215 nm and the π_0-π* transition at ~198-175 nm, due to the electric and magnetic dipole transition moments in the amide orbitals. The heterodimeric CC investigated in this work forms an α-helical structure and CD will be used as the main structural characterization technique. The individual CC-forming peptides form a random coil, which is characterized by a minimum at ~200 nm in the CD spectrum. CD spectra greatly depend on the solvent, which mainly affects the n-π* transition, and on the helix length. The latter affects the π_o-π* transition, as short helices (<30 residues) show a larger dependence on the helix macrodipole.

CD does not only provide information about the secondary structure. It can also be used to monitor changes in the secondary structure, e.g. upon ligand binding. It further reports on conformational changes induced by environmental changes, such as salts, temperature or chemical denaturants (GuHCl or urea). Thermal or chemical denaturation allows quantifying the stability of the protein or peptide of interest. In this work, CD was utilized with the goal of investigating the secondary structure of the CCs at room

temperature and to determine their thermodynamic stability, using temperature as the denaturant.

Experimental procedure

All CD measurements were performed using a Chirascan™ CD spectrometer (Applied Photophysics, UK) in a quartz cuvette with 1 mm path length. The individual CC-forming peptides were dissolved in a concentration of 50 µM in the buffer required for the measurements (PBS; PIPPS-BS +/- Ni^{2+}), containing a 10-fold excess of TCEP to prevent disulfide bond formation. The peptides were then mixed in a 1:1 ratio to yield a CC concentration of 25 µM. Before measuring the CD spectra, a blank was measured with the respective buffer. In the experiments using PIPPS-BS + Ni^{2+}, the $NiCl_2$ concentration was 3x the total peptide concentration (i.e. 150 µM).

All measurements were performed in a wavelength range from 195-250 nm. The parameters used for these measurements were: scan speed 1 nm s^{-1}, band width 1 nm, 1 nm step size, and 0.7 s integration time per point. For the thermal denaturation experiments, the temperature was increased from 4.5 °C to 95 °C at a rate of 1 °C min^{-1}. The molar ellipticity (ME) in deg cm^2 $dmol^{-1}$ was calculated using the following equation:

$$(4) \qquad ME\ (deg\ cm^2\ dmol^{-1}) = \frac{\theta \times 10^6}{l \times c},$$

where θ is the ellipticity in mdeg, l is the path length in mm, and c the total peptide concentration in micromolar (50 µM).

The melting temperature T_m was extracted using a global fit to the full spectra (GlobalFit3, Applied Photophysics). Double baseline correction was used whenever possible; otherwise single baseline correction was applied. All measurements were performed in triplicate.

van't Hoff analysis

In addition to the T_m determination described above, also the free energy between the folded and the unfolded state (ΔG_{N-U}) of each CC was determined from van't Hoff plots. For this purpose, the molar ellipticity values at 222 nm were extracted from the thermal denaturation experiments, and plotted as a function of temperature. Subsequently, van't Hoff plots were established as described in Mergny et al. [136]: The upper ($ME_{222,F}(T)=ME_{222,F}^0+m_F T$) and lower ($ME_{222,U}(T)=ME_{222,U}^0+m_U T$) baselines were selected manually and the median was calculated (($ME_{222,U}$ + $ME_{222,F}$)/2) to establish the melting temperature (Figure 11). In the following, the fraction folded was determined to calculate the equilibrium constant (K_{eq}) for each temperature:

(5)
$$K_{eq} = (1 - \theta_T)/\theta_T$$

where θ_T is the folded fraction:

(6)
$$\theta_T = [ME_{222}(T) - ME_{222,U}(T)]/[ME_{222,F}(T) - ME_{222,U}(T)]$$

Using the equilibrium constant (K_{eq}) and the absolute temperature in Kelvin (T), the enthalpy (ΔH) and entropy (ΔS) can be extracted from the van't Hoff plot:

(7)
$$\ln K_{eq} = -\frac{\Delta H}{R}\left(\frac{1}{T}\right) + \frac{\Delta S}{R}$$

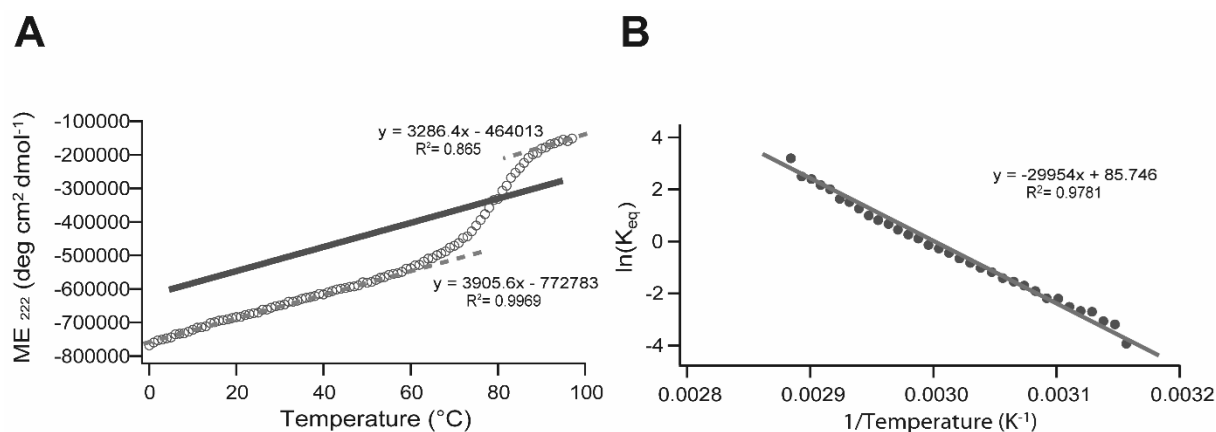where R is the gas constant (8.314 J mol^{-1} K^{-1}).

FIGURE 11 – Example of one van't Hoff plot. Extraction of thermodynamic parameters from the molar ellipticity data at 222 nm (ME$_{222}$) from one of the A4/B4 triplicates. A) Determination of the upper and lower baselines (dashed lines) of the ME$_{222}$ data. The solid line indicates the median from which the T$_m$ can be obtained. B) van't Hoff plot restricted to 0.03<folded fraction<0.97. From the linear fitting, ΔH and ΔS are obtained.

The Gibb's free energy ΔG_{N-U} was subsequently obtained from equation

(8)
$$\Delta G = \Delta H - T\Delta S$$

It should be noted that the T_m values reported throughout this work are those obtained from the global fit as described above.

6.2.2. SINGLE MOLECULE FORCE SPECTROSCOPY

Introduction

Single-molecule force spectroscopy (SMFS) allows for the mechanical manipulation of biomolecules at a molecular level. SMFS is frequently used for investigating the stability of receptor-ligand interactions, where the applied force speeds up the dissociation process. It is further used for determining the mechanical stability of biomolecules, such as protein domains and nucleic acid structures. In these cases, force is used as a denaturant, speeding up the unfolding and slowing down the folding process. SMFS commonly utilizes the atomic force microscope (AFM) as well as optical and magnetic tweezers (Table 7). In this work, I will use the AFM to mechanically separate the two chains of heterodimeric CCs and to record the force required for chain separation.

TABLE 7 – Comparison of single-molecule force spectroscopy techniques. Adapted with permission from Springer Nature: Single-molecule force spectroscopy: optical tweezers, magnetic tweezers and atomic force microscopy, K. C. Neuman, A. Nagy [Copyright © 2008, Springer Nature [137]

	Optical tweezers	Magnetic tweezers	AFM
Spatial resolution (nm)	0.1–2	5–10	0.5–1
Temporal resolution (s)	10^{-4}	10^{-1}–10^{-2}	10^{-3}
Stiffness (pN nm^{-1})	0.005–1	10^{-3}–10^{-6}	10–10^5
Force range (pN)	0.1–100	10^{-3}–10^2	10–10^4
Displacement range (nm)	0.1–10^5	5 –10^4	0.5–10^4
Total probe size (μM)	0.25–5	0.5–5	100–250

Optical and magnetic tweezers are usually applied for constant force measurements (force clamp), where the molecule(s) of interest are held at a constant force for extended periods of time. In contrast, AFM-based SMFS is used to apply a steadily increasing force on the molecule(s). This allows for recording the force required to dissociate a receptor-ligand interaction or to unfold a protein domain. In general, the AFM is used for detecting forces larger than 10 pN. As AFM-based SMFS is the main technique used throughout this work, I will describe the working principle of the AFM in the following.

The **atomic force microscope (AFM)** is mainly known as a high-resolution imaging technique, which was first developed in 1989 by Binnig, Quate and Gerber [138]. The AFM is composed of the following components (Figure 12B): the cantilever and a piezoelectric scanner, which provides accurate *x,y,z* resolution in the sub-nanometer range. When

performing SMFS, the cantilever is only moved in the *z*-direction, i.e. towards and away from a surface. Therefore, when a biomolecular interaction is immobilized between the surface and the cantilever, this interaction is stretched when the distance between cantilever and surface increases (Figure 12). With increasing distance, the interaction feels an increasing force, which bends the cantilever towards the surface. Cantilever bending is read out with a focused laser beam, which is reflected at the backside of the cantilever. The reflected beam is recorded on a quadrant photodiode where the deflection of the laser beam is converted into voltage. An unbinding or unfolding event is thus displayed as a jump in voltage at a given piezo position. These quantities are subsequently converted into force and distance between the cantilever tip and the surface.
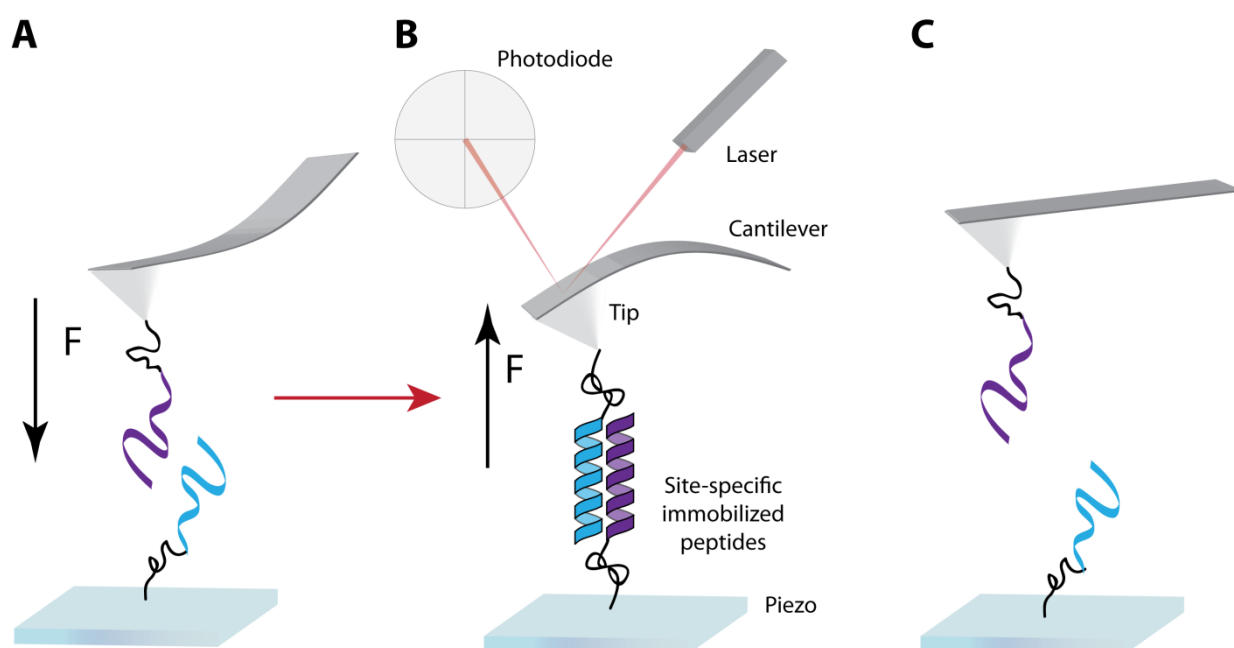

FIGURE 12 – Overview of the single-molecule force spectroscopy set-up for CCs. A) The flexible cantilever with a sharp tip is approaching the surface, allowing the peptides to interact. B) The tip is retracted to induce the detachment of the peptide-peptide interaction. A focused laser beam, reflected onto a photodiode, is used to read out the bending. To form the CC, one peptide chain is immobilized on the cantilever tip and the second chain is immobilized on a surface. The distance between the cantilever tip and the surface is controlled with a piezoelectric device. C) The rupture force is determined at the point where detachment occurs.

To convert the raw data into force-distance curves, the voltage recorded at the photodiode needs to be converted into force (*F*). The cantilever behaves like a Hookean spring so that *F* can be calculated using its intrinsic spring constant *k*:

(9) $$F = -k \cdot \Delta z_c$$

Where Δz_c is the difference in deflection in the *z*-range of the cantilever (corrected with the piezo displacement, Δz_p).

To calculate the force, two values are hence necessary: the **cantilever bending** calibrated against the voltage difference (ΔV; optical sensitivity), and the calibrated **spring constant** of the cantilever.

In this work, the optical sensitivity was obtained from pushing the cantilever onto the surface at high contact forces, so that the displacement of the piezoelectric positioner (Δz_p) equals the displacement of the cantilever (Δz_c). The optical sensitivity (in nm V^{-1}) is then extracted from the slope of a ΔV *vs* Δz_p, plot.

The spring constant usually ranges from $10\text{-}10^5$ pN nm^{-1} and depends on the material and shape of the cantilever. As a result of the fabrication process, each cantilever has its own spring constant, and needs to be calibrated experimentally. In this work, the thermal noise method was used [139]. The method is based on the assumption that the cantilever behaves as an ideal spring, which is only affected by thermal fluctuations. The spring constant is thus obtained from the thermal noise spectrum of the cantilever (mean square displacement of the cantilever fluctuations vs. oscillation frequency). The integration of the frequency spectrum yields the spring constant value. In this work, the AFM software (JPK Instruments AG, Germany) was used to derive the spring constant from the thermal noise spectrum [140].

Having determined the cantilever deflection (in nm), this value is multiplied by the spring constant (in pN nm^{-1}) to obtain the force in pN. Following this conversion, the data is displayed in the form of **force-distance curves** [140]. A typical force-distance curve is shown in Figure 13.
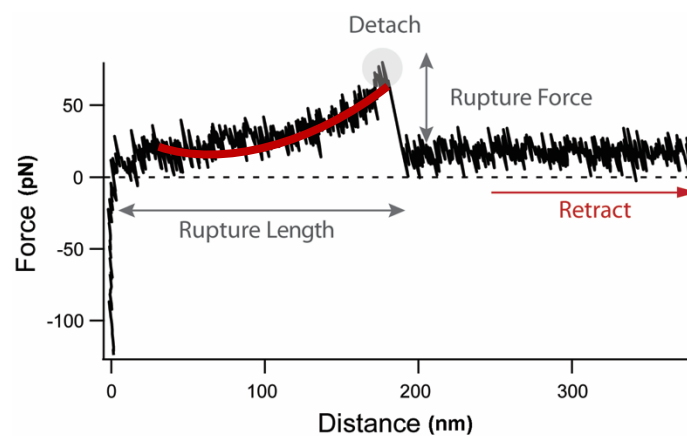

FIGURE 13 - Example of a force-distance curve. Upon retraction of the cantilever, the CC is stretched and the force increases until the CC ruptures. The rupture force is extracted at the detachment point. The red solid line illustrates a fit with a polymer model (WLC).

In a SMFS experiment, it is necessary to include a linker between the molecule of interest and the cantilever or surface (Figure 12). This linker allows for distinguishing between specific and non-specific rupture events. It further allows for distinguishing true single rupture events from multiple rupture events (i.e. force-distance curves where more

than one interaction ruptures). For this purpose, PEG [141] is frequently used as the linker of choice. PEG is a well-characterized polymer with a low polydispersity [142, 143]. Its force-extension behavior is well-characterized, i.e. it can be fully described with a polymer model, such as the worm-like chain (WLC, eq. 10) or freely jointed chain (FJC) model.

$$(10) \qquad F(z) = \frac{k_B T}{Lp} \left[\frac{1}{4} \left(1 - \frac{z}{L_c} \right)^{-2} - \frac{1}{4} + \frac{z}{L_c} \right],$$

where k_B is the Boltzmann constant, z is the end-to-end distance of the polymer, and L_p and L_c are the persistence length and the contour length of the polymer, respectively.

Fitting the obtained force-distance curves with e.g. the WLC model provides the contour length of the polymer, which links the molecule of interest between the surface and the cantilever tip. Comparing the extracted contour length with the expected length for the polymer used, this provides an important control for ensuring that specific interactions are observed. Knowledge of the polymer properties is further required to determine the so-called loading rate ($r = \mathrm{d}F/\mathrm{d}t$), which describes how fast the force increases directly at the molecular interaction.

Dynamic single-molecule force spectroscopy

When performing AFM-based SMFS, the cantilever is usually moved away from the surface at a constant retract speed (v in nm s^{-1}); however, the force acting on the molecule does not increase linearly as the polymeric linker possesses a non-linear force extension behavior as described above. To fully describe the mechanical stability of a molecular interaction, knowledge of the loading rate is required. It is well-described that the mechanical stability of many biomolecular interactions depends on the loading rate experienced. This can be explained when considering the effect of the applied force on the energy landscape of the interaction.

In this work, the CC exists in a folded and an unfolded state. Initially the CC is in its unfolded state as the individual peptide chains are immobilized to the surface and the cantilever, respectively. The chains associate and fold into a CC when the cantilever is approached to the surface. When the cantilever is retracted, force acts as a denaturant, thereby increasing the probability of the CC to dissociate and unfold (Figure 14). The applied external force thus tilts the energy landscape, lowering the energy barrier at the transition state along the reaction coordinate x. If the barrier is lowered slowly (low loading rate), thermal fluctuations have a higher relative contribution to chain separation than at high loading rates.
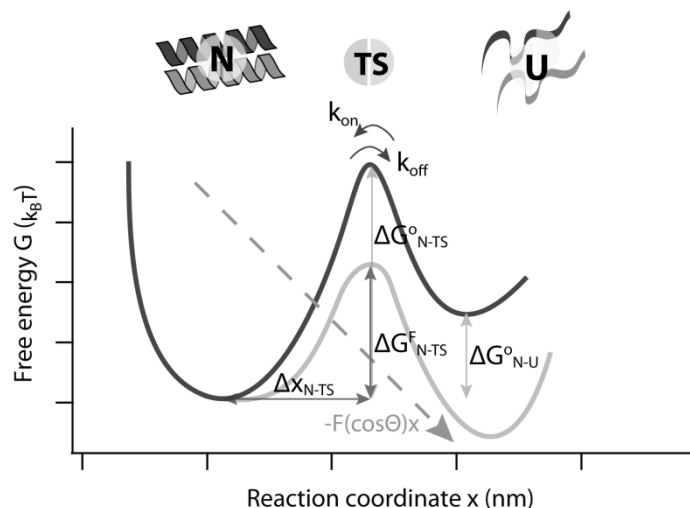
FIGURE 14 – Schematic energy landscape of the folded-unfolded states of a CC. Force acts along the reaction coordinate lowering the energy barrier and therefore favouring the CC unfolded state (assuming a two-state model).

The thermally assisted nature of the process necessitates that a high number of force-distance curves must be obtained at different loading rates. For each loading rate the most probable rupture force is a function of the loading rate as first described by Evans and Ritchie in 1997 [144]. An example of the forces obtained at different loading rates is given in Figure 15.
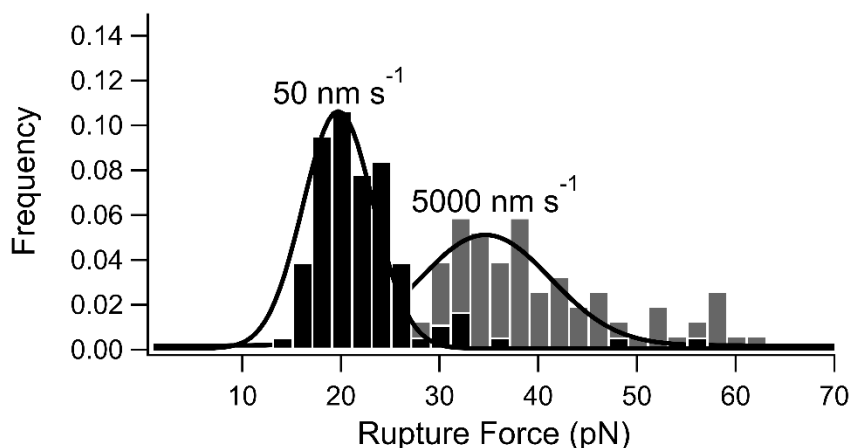

FIGURE 15 – Typical rupture force histograms obtained at different loading rates. The histograms show the rupture forces for one Coiled Coil, when measured at the lowest and fastest retract speed (50 and 5,000 nm s^{-1}). The dependence of the rupture force on the loading rate is clearly visible. The retract speeds shown yield loading rates of 26 and 9072 pN s^{-1}, respectively.

This procedure has since been named **dynamic single-molecule force spectroscopy**. Several models [145] are now available to analyze the relationship between rupture force and loading rate. These models yield kinetic parameters, describing the energy landscape of the interaction of interest, such as the dissociation rate k_{off} (probability of bond survival at zero force) and the distance to the transition state $\Delta x_{N\text{-}TS}$ (measure of the total deformation

of the structure prior to chain separation) (Figure 14). In this work, the **Bell-Evans model** [144] was utilized for the analysis of dynamic SMFS data (Figure 16).
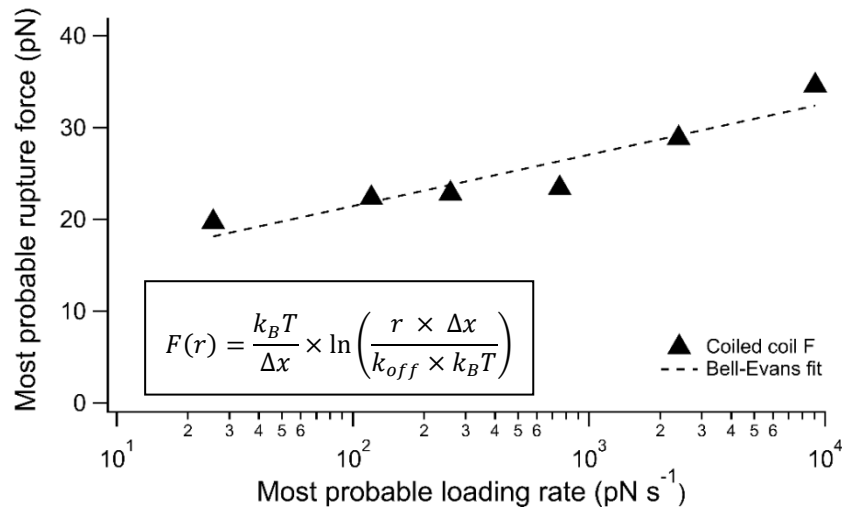

FIGURE 16 – Example data set of the dynamic SMFS experiment. The most probable rupture forces are plotted against the corresponding most probable loading rates. The dashed line represent the Bell-Evans fit (equation is shown in the text box), from where Δx_{N-TS} and k_{off} are extracted. Coiled Coil F represents the most probable rupture force at the corresponding most probable loading rate.

More recently, the initially proposed Bell-Evans model [144] has been generalized and extended. Whereas the Bell-Evans model assumes that the distance to the transition state is not altered by the applied force, the Dudko–Hummer–Szabo model includes the possibility that the distance to the transition state may be affected as the molecular interaction experiences a force. In contrast to the Bell-Evans model, the Dudko–Hummer–Szabo further allows for obtaining the height of the energy barrier between the folded and the transition state ΔG_{N-TS} [146]. The Friddle-Noy-DeYoreo model considers *rebinding* of the molecular interaction [147].

It should be noted that ΔG_{N-TS} (i.e. the difference in energy between the native and the transition state) can also be calculated from the Arrhenius equation using the k_{off} extracted from the above mentioned Bell-Evans fit, provided that the Arrhenius pre-exponential factor A is known [148]:

$$(13) \qquad \Delta G_{N-TS} = k_B T * \ln\left(\frac{A}{k_{off}}\right)$$

For the pre-exponential factor A, a value of 5×10^8 s^{-1} was used, considering diffusive barrier crossing as proposed by Kramers. This pre-exponential factor is in the range of the values used in the literature for small α-helical dimers like the GCN4 leucine zipper [149, 150].

Experimental procedure

Dynamic SMFS measurements were performed using a ForceRobot300 (JPK Instruments AG, Germany) at room temperature in PBS or PIPPS-BS buffer. MLCT cantilever chips (Bruker, CA, USA) were used for all measurements where the CCs were measured in the shear geometry, whereas MLCT-Bio cantilever chips (Bruker, CA, USA) were used for measurements in the unzip geometry (due to its larger tip radius). In all cases, cantilever C with a nominal spring constant of 0.01 N m^{-1} was used. The cantilevers were post-calibrated using the thermal noise method [139]. The calibration values are shown in Table A2.

Several hundred force-distance curves were collected for each retract speed in the range from 50 nm s^{-1} to 5,000 nm s^{-1}. During each measurement, the cantilever was moved on a 8 x 8 grid (corresponding to an area of 10 x 10 μm^2). Each CC was measured in triplicate (using a new cantilever and surface) at 6 different retract speeds. The force-distance curves were analyzed using the JPK analysis program and IGORPro (WaveMetrics, USA). The force-distance curves were fitted with the WLC model to select force-distance curves that contained a specific single rupture event. Only force-distance curves with a contour length >100 nm (the expected length is ~130 nm: 2 PEG polymers with a length of ~65 nm; 10 kDa) and a persistence length >0.3 nm were considered as a specific binding event and used for the following steps [142]. For each retract speed, the rupture forces and loading rates were extracted for further analysis [151]. The rupture forces and loading rates, obtained from 20-200 force-distance curves, were plotted into histograms and the corresponding most probable values were obtained from a Gaussian fit to these histograms. The most probable rupture forces were then plotted against the corresponding most probable loading rates. The resulting plots were fitted with the Bell-Evans model [144] (see Figure 16 for an example).

6.2.3. SURFACE IMMOBILIZATION OF COILED COIL-FORMING PEPTIDES

Introduction

To define the pulling geometry (shear vs. unzip), the CCs need to be immobilized in a site-specific manner. To obtain a shear pulling geometry, a cysteine (containing a thiol group) was introduced at the N-terminus of one peptide and at the C-terminus of the other peptide. In contrast, the Cys residues were placed in the same terminus of both peptides to obtain the unzip geometry.

As mentioned above, long linkers need to be placed between the peptide and the cantilever tip and the surface. Also for this purpose, PEG is an ideal linker as it is available with a number of different reactive groups, including thiol-reactive maleimide groups. Utilizing the Michael addition between thiol and maleimide functional groups provides a number of advantages. First, the thiol group is easily incorporated into the peptides at the desired position during solid-phase peptide synthesis. Second, the reaction is highly specific and efficient, ensuring good control over the density of peptides on the cantilever and the surface.

Overall, a 3-step protocol was used, as described by Zimmermann *et al.* [152] (Figure 17). The surfaces (glass coverslips) and cantilevers were first silanized with a mono-reactive silane, carrying an amino-group. The amino-group was then reacted with a hetero-bifunctional PEG, carrying an amino-reactive NHS-ester and a thiol-reactive maleimide group. In the last step, the Cys-terminated peptides were coupled to the maleimide-functionalized surface. With this protocol, the concentration of peptides can be adjusted in the last step to ensure that between 5-15 % of all force-distance curves contain a single rupture event.
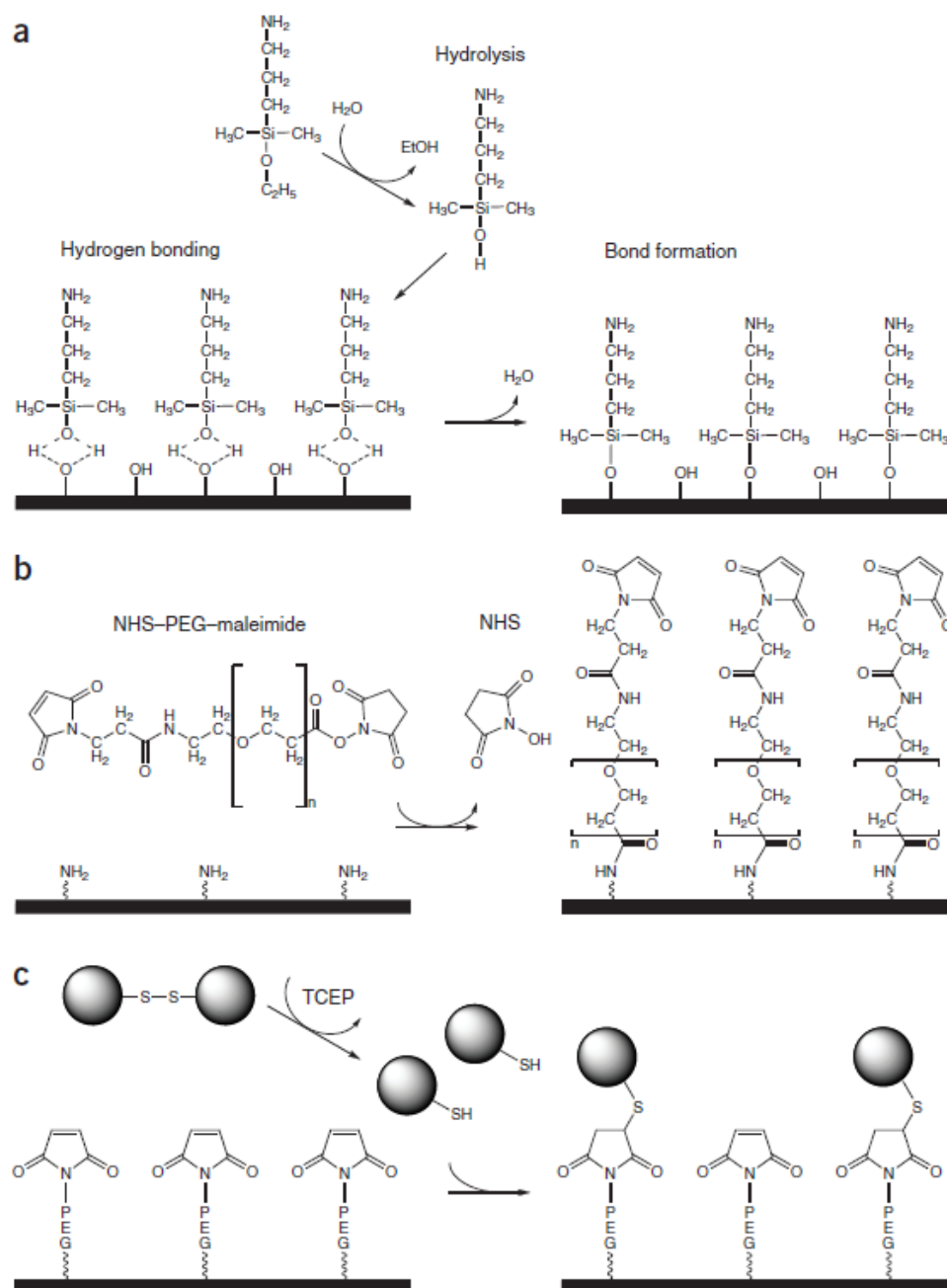
FIGURE 17 – Site-specific immobilization of the peptides. A) Functionalization of a silicon oxide surface with amino-silane. B) Coupling of a hetero-bifunctional NHS-PEG-maleimide. C) Thiol-maleimide reaction between the Cys of the peptide and the maleimide-functionalized surface. (Reprinted with permission from Springer Nature: Thiol-based, site-specific and covalent immobilization of biomolecules for single-molecule experiments, J. L. Zimmermann, T. Nicolaus, G. Neuert, K. Blank [Copyright © 2010, Springer Nature [152])

Experimental procedure

Glass coverslips (Menzel Gläser, Germany) with a diameter of 22 mm were cleaned with ultrapure water and isopropanol to remove any impurities that could interfere with the silanization reaction. The clean coverslips were then incubated for 1 hour in a solution of 1 % (v/v) 3-aminopropyl dimethyl ethoxysilane (ABCR GmbH, Germany) in ethanol.

Following incubation, the coverslips were washed in isopropanol and ultrapure water, and baked at 80 ºC for 1 hour. MLCT and MLCT-Bio cantilever chips (Bruker, USA) were cleaned in a UV-ozone cleaner for 10 min. Following cleaning, they were immersed in pure 3-aminopropyl dimethyl ethoxysilane for 10 min. The cantilever chips were washed in isopropanol and ultrapure water and baked at 80 ºC for 30 min. The amino-functionalized coverslips and cantilever chips were stored in dry N_2 atmosphere until use.

For the next step, the functionalized coverslips and cantilever chips were incubated in borate buffer for 1 hour. Subsequently, the hetero-bifunctional NHS-PEG-maleimide (10 kDa; Rapp Polymere, Germany) was dissolved in borate buffer to a concentration of 30 mM. The PEG solution was incubated on the coverslips and the cantilever chips for 1 h to allow for the thiol-maleimide reaction to occur. The peptides were diluted in coupling buffer to a concentration of 300 µM (cantilever) and 1 mM (surface). Thiol-maleimide coupling reactions were then performed in coupling buffer at 4 ºC for 1 h. Finally, cantilevers and surfaces were first washed and then stored in PBS or PIPPS-BS at 4 °C until the AFM measurement was started.

7. RESULTS AND DISCUSSION

7.1. EXPERIMENTAL DESIGN

To understand how different modifications affect the mechanics of CCs and how these correlate with the thermodynamic properties, a thermodynamically well-characterized 4-heptad heterodimer was used as the starting point. This heterodimer was published by Thomas *et al.* [47] in 2013 and will be called A4/B4 in the following. The acidic peptide (A4) follows the heptad pattern (EIAALEX)$_n$ and the basic sequence (B4) has a (KIAALKX)$_n$ heptad repeat, where X are Gln and Lys to add solubility. *a* and *d* positions are thus occupied by Ile and Leu. The location of a β-branched amino acid in the *a* position and a γ-branched amino acid in the *d* position confers a tight packing at the CC interface. This buried apolar interface is hence one of the main driving forces to provide stability to the CC [128]. The third heptad of each peptide contains Asn to enhance the specificity of heterodimer formation. The CC further contains one aromatic amino acid per chain (Trp or Tyr) for concentration measurements. The termini have been capped (acetylated N-terminus and amidated C-terminus; Table A1) to avoid undesired interactions between the side chains and the helix dipole (which could lead to a destabilizing effect [61, 153]).

A4/B4 is a thermodynamically highly stable CC with a dissociation constant in the picomolar range and a melting temperature (T_m) of 81.0 ± 0.5 °C. As described in the introduction, A4/B4 has also been characterized mechanically in the shear geometry using AFM-based SMFS. It shows rupture forces between 35 and 50 pN, depending on the loading rate used [108].

Using this CC heterodimer as the starting point, different CCs were designed, synthesized and characterized thermodynamically and mechanically (Figure 18). Specifically, the sequences were designed to answer the following questions:

1. How do the basic design parameters (hydrophobic interactions and helix propensity) affect CC mechanics? What is the **sequence-structure-mechanics relationship** of CC dimers?

   This question will be addressed using two new sequences, which carry a Ile->Val substitution in the *a* position (A4$_{V1-4}$/B4$_{V1-4}$) or an Ala->Ser substitution in the *b* position (A4$_{S1-4}$/B4$_{S1-4}$).

2. What is the effect of the **pulling geometry** on the mechanical stability of the same CC sequence?

   This question will be addressed using different coupling sites on A4/B4, where the Cys residues are located at different termini. The A4 and B4 peptides where the Cys residues are placed at the opposite termini are designated A4$_2$ and B4$_2$.

3. Is it possible to mechanically stabilize the CC when introducing artificial helix stabilizing interactions?

    This question will be addressed with *stapled* **peptides,** where the *staples* are inserted with the goal of bridging two amino acid side chains either directly at the point of force application or in the complementary peptide. To understand the mechanistic response of the CC to the applied force, covalent ($A4_{X-2}$ and $B4_{X-2}$) and dynamic *staples* ($A4_{H-2}$) will be compared.

4. Is it possible to enhance hydrophobicity at the CC interface with non-natural, **fluorinated amino acids**?

    This question will be addressed with one new sequence, which carries trifluoroethyl glycine (TfeGly) in the *d* position of the second heptad in the A4 and/or B4 peptide. The fluorinated peptides are termed $A4_F$ and $B4_F$, respectively.
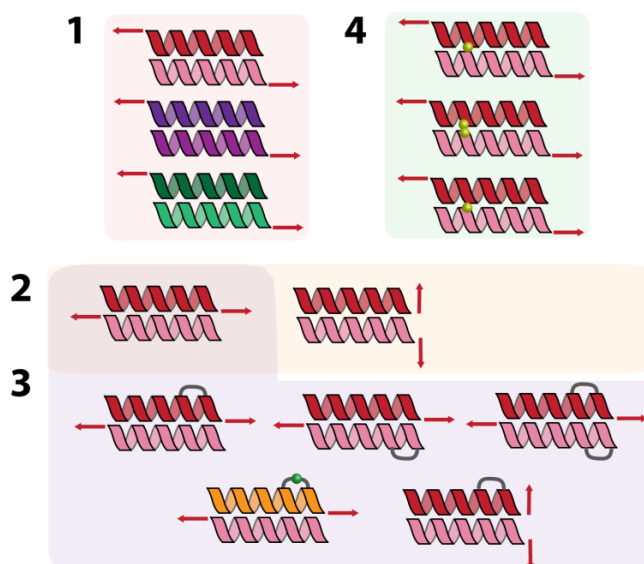

FIGURE 18 – General overview of the systems used in this thesis. The table shows the Coiled Coils formed when combining the different monomers. The Coiled Coils are grouped by the different sections in the results: 1 (sequence-structure-mechanics relationship), 2 (pulling geometry), 3 (*stapled* peptides) and 4 (fluorinated peptides). Different colors indicate changes in their sequence, and red arrows show the direction of the applied force.

7.2. UNDERSTANDING COILED COIL MECHANICS USING A SEQUENCE-BASED APPROACH

In the first part of this work, a sequence-based approach towards understanding CC mechanics was used. SMFS has already been established as a key technique for determining the unfolding and rupture forces of CC-based proteins [28, 29, 94, 106] and CC motifs. A GCN4-derived CC hairpin was studied in the unzip geometry [98, 129] with unfolding forces below 20 pN and the 4-heptad CC A4/B4, used in this work, was investigated in the shear geometry with rupture forces above 40 pN [108].

It has been established for a number of different protein folds, and most importantly for CCs, how sequence modifications affect the native state structure [154-156] and also the mechanical stability [155, 156]. In the case of CCs, the following modifications need to be considered: the hydrophobic core [45], the α-helix propensity [77] and ionic interactions [157]. Specifically, the following aspects are presented and discussed in this section:

(1)   Canonical amino acid substitutions have been made in the established model system A4/B4 to investigate how hydrophobicity and α-helix propensity determine the mechanical stability and the underlying energy landscape of this CC.

(2)   The solution conditions have been altered to elucidate the role of interhelical salt bridges on the mechanical stability of the CC. Buffers with different pH and/or salt concentration were used to disrupt these salt bridges without the need to alter CC sequence.
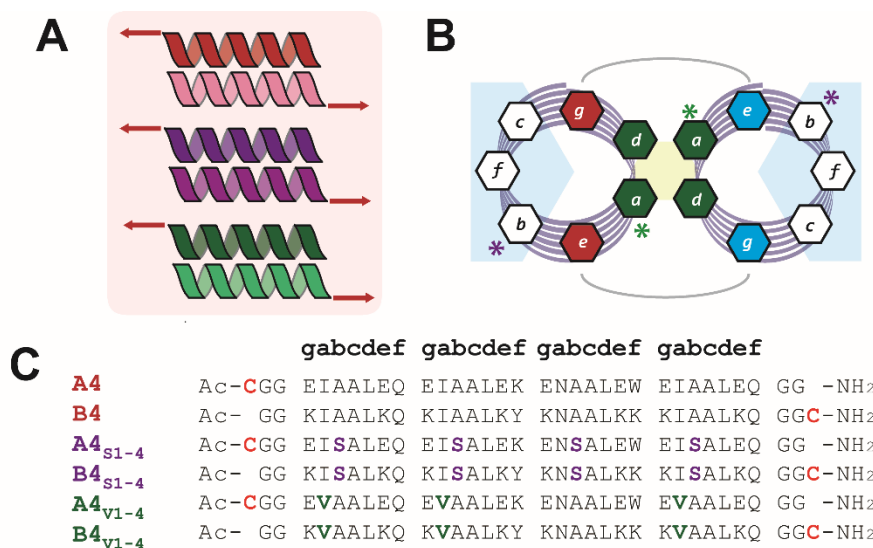

FIGURE 19 – Rational design of the Coiled Coils A4/B4, A4$_{S1-4}$/B4$_{S1-4}$ and A4$_{V1-4}$/B4$_{V1-4}$. A) Scheme of the pulling geometry used for each Coiled Coil (Red = A4/B4, Purple = A4$_{S1-4}$/B4$_{S1-4}$, and green = A4$_{V1-4}$/B4$_{V1-4}$). B) Helical wheel representing a heterodimeric parallel Coiled Coil. The positions modified in this section are marked with an asterisk. C) Sequences of the Coiled Coils used in this study. Sequence modifications are depicted in bold.

7.2.1. CANONICAL AMINO ACID SUBSTITUTIONS AND THEIR EFFECT ON COILED COIL MECHANICS

It is known that specific hydrophobic core amino acids as well as the α-helix propensity of the individual helices affect the thermodynamic stability of CCs [45]; however, the relationship between sequence, thermodynamics and mechanics has not yet been established. Towards this goal, this work focuses on the thermodynamic and mechanical characterization of CCs with different α-helix propensity and hydrophobic core packing.

The design of these CCs was based on the work of Thomas et al. [44] and Litowski *et al.* [45], following the standard rules of CC design (Figure 19). A4/B4 was defined as the reference sequence due to its high thermodynamic stability and well-characterized mechanics [108]. To investigate how α-helix propensity affects the thermodynamic and mechanic stability of the CC, A4$_{S1-4}$/B4$_{S1-4}$ was designed. Ser was included in the *b* position of each heptad (ISALXXX). It has a lower helical propensity than Ala [76] because of its slightly bulkier side chain. The second CC, A4$_{V1-4}$/B4$_{V1-4}$, contains another β-branched amino acid in position *a*. Ile was replaced with the less bulky amino acid Val (VAALXX) to loosen the packing of the hydrophobic core and to decrease the overall hydrophobicity of the CC interface [52]. To define the pulling geometry, Cys was located at the N-terminus of each A-peptide and at the C-terminus of each B-peptide (Figure 19C).

To investigate the secondary structure and thermodynamic stability of these sequences, CD spectroscopy as well as thermal denaturation experiments were performed. All three CCs showed two characteristic minima at 208 and 222 nm, representing a formed α-helical structure and, therefore, a heterodimeric CC. The α-helical content, predicted for each monomer with AGADIR [78], is also correlated to the ellipticity of the CD spectra. As expected [65], A4/B4 was the most stable CC showing a T_m of 77.5 °C, while A4$_{S1-4}$/B4$_{S1-4}$ (T_m = 53.2 °C) and A4$_{V1-4}$/B4$_{V1-4}$ (T_m = 60.5 °C) were dramatically destabilized by their corresponding mutations. The most thermodynamically stable CC A4/B4 is the CC that consists of the monomers with the highest α-helix propensity (Table 8).
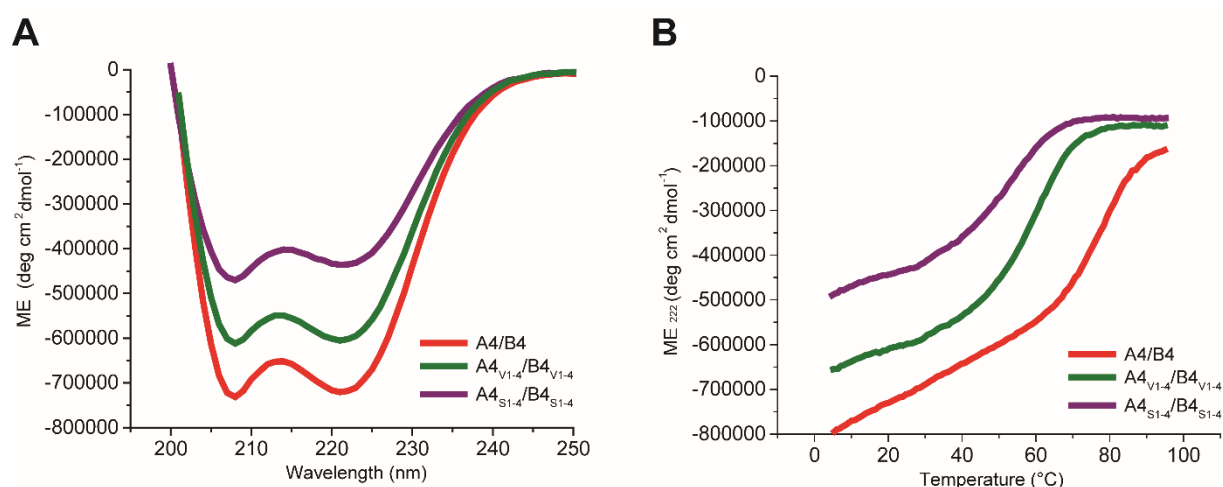

FIGURE 20 – Circular Dichroism spectroscopy of the Coiled Coils A4/B4, A4$_{S1-4}$/B4$_{S1-4}$ and A4$_{V1-4}$/B4$_{V1-4}$. A) CD spectra showing the α-helical pattern of the three CCs, characterized by their two characteristic minima at 208 and 222 nm. B) Thermal denaturation monitored at a wavelength of 222 nm.

The thermal denaturation curves (Figure 20B) further allow for calculating the free energy difference between the folded in the unfolded state, ΔG_{N-U}. First, a van't Hoff plot was generated, as described in the Methods section and shown in Figure 21. The van't Hoff analysis yields ΔH and ΔS, which was then used to calculate ΔG_{N-U} in a second step (Table 8).
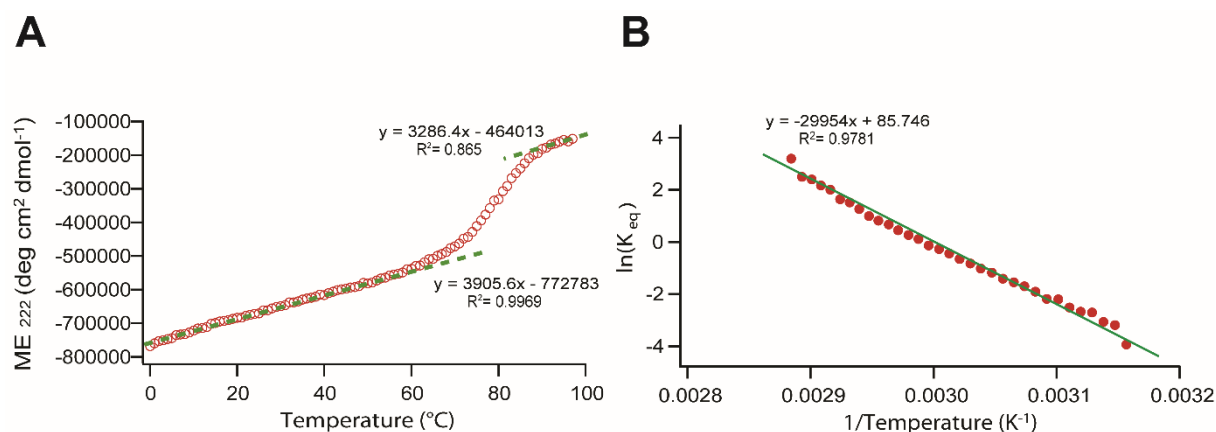

FIGURE 21 – van't Hoff plot of A4/B4. A) Determination of the upper and lower baselines (green dashed lines) of the ME 222 data. B) van't Hoff plot (0.03 < folded fraction < 0.97). From the linear fit (green solid line), ΔH and ΔS were obtained.

For both modified CCs, $A4_{S1-4}/B4_{S1-4}$ (5.3 k_BT) and $A4_{V1-4}/B4_{V1-4}$ (7.1 k_BT), the thermodynamic stability was reduced in comparison to the reference CC A4/B4 (14.2 k_BT). These results are consistent with the work of Litowski *et al.* [45], where a single Val-Ile substitution destabilized the *EK* heterodimer by 0.47 kcal mol^{-1} and a single Ala-Ser substitution destabilized the CC by 0.41 kcal mol^{-1}. Here $A4_{S1-4}/B4_{S1-4}$ is less stable than $A4_{V1-4}/B4_{V1-4}$, which can be explained with the different number of substitutions (4 Ala-Ser substitutions in contrast to 3 Ile-Val substitutions).

TABLE 8 – Thermodynamic characterization of A4/B4, $A4_{S1-4}/B4_{S1-4}$ and $A4_{V1-4}/B4_{V1-4}$. $\theta_{222}/\theta_{208} > 1$ suggests a well-established Coiled Coil structure. ΔH (difference in enthalpy) and ΔS (difference in entropy) were obtained from van't Hoff plots. To calculate ΔG_{N-U}, T = 298 K was used. The AGADIR scores reflect the α-helix propensity of each monomer at T = 298 K, ionic strength = 0.14 M, pH 7.4 [78]. All parameters are calculated as mean ± SEM (n = 3).

	AGADIR score	$\theta_{222}/\theta_{208}$	T_m (°C)	ΔG_{N-U} (k_BT)	ΔH (k_BT)	ΔS (k_B)
A4/B4	4.97/ 10.34	1.02	77.0 ± 0.3	14.2 ± 0.3	96.4 ± 2.1	0.28 ± 0.01
$A4_{S1-4}/B4_{S1-4}$	1.86/ 2.17	0.93	54.3 ± 0.3	5.3 ± 0.2	64.9 ± 2.0	0.20 ± 0.01
$A4_{V1-4}/B4_{V1-4}$	3.0/ 5.5	1.02	59.0 ± 0.6	7.1 ± 0.6	69.3 ± 3.9	0.21 ± 0.01

To address the question whether the thermodynamic and mechanical stabilities are correlated or are independent parameters, SMFS was carried out with the newly designed CCs. At one single retract speed of 400 nm s^{-1}, SMFS reveals that the *most probable rupture force* is lower for A4$_{S1-4}$/B4$_{S1-4}$ (23.6 pN) and for A4$_{V1-4}$/B4$_{V1-4}$ (28.2 pN), when compared to A4/B4 (43.1 pN; Figure 22).

For each CC, six different retract speeds in the range from 50 nm s^{-1} to 5,000 nm s^{-1} were subsequently used to establish how the most probable rupture forces depend on the loading rate (r = dF/dt). The corresponding loading rates were between 10 pN s^{-1} and 10,000 pN s^{-1}. Several hundreds of force-distance curves were collected, out of which approx. 20 to 300 displayed a single rupture event (Table A4 in the Appendix). Each experiment was performed in triplicate. As explained in the Methods section, a so-called dynamic force spectroscopy diagram was plotted, showing the most probable rupture forces vs. the most probable lading rates. Fitting the data to the Bell-Evans model [144], allows for extracting the characteristic energy landscape parameters k$_{off}$ (the dissociation rate in the absence of force) and Δx_{N-TS} (the distance from the native to the transition state) (Table 9).

These results suggest that modification of the α-helix propensity destabilizes the CC, both thermodynamically and mechanically. This modification mostly affects the k$_{off}$ (0.28 s^{-1} in contrast to 3.2 x 10^{-4} s^{-1} for A4/B4) and the height of the energy barrier (ΔG_{N-TS}). At the same time, Δx_{F-TS} becomes shorter (0.93 nm instead of 1.35 nm for A4/B4). Also, the modification at the hydrophobic interface leads to a lower mechanical stability when compared to A4/B4; however, in this case mainly Δx_{F-TS} is affected and increases to 1.71 nm. The height of the energy barrier ΔG_{N-TS} only decreases from 29.2 k$_B$T to 26.6 k$_B$T, which suggests that the lower mechanical stability mostly originates from a wider energy well.
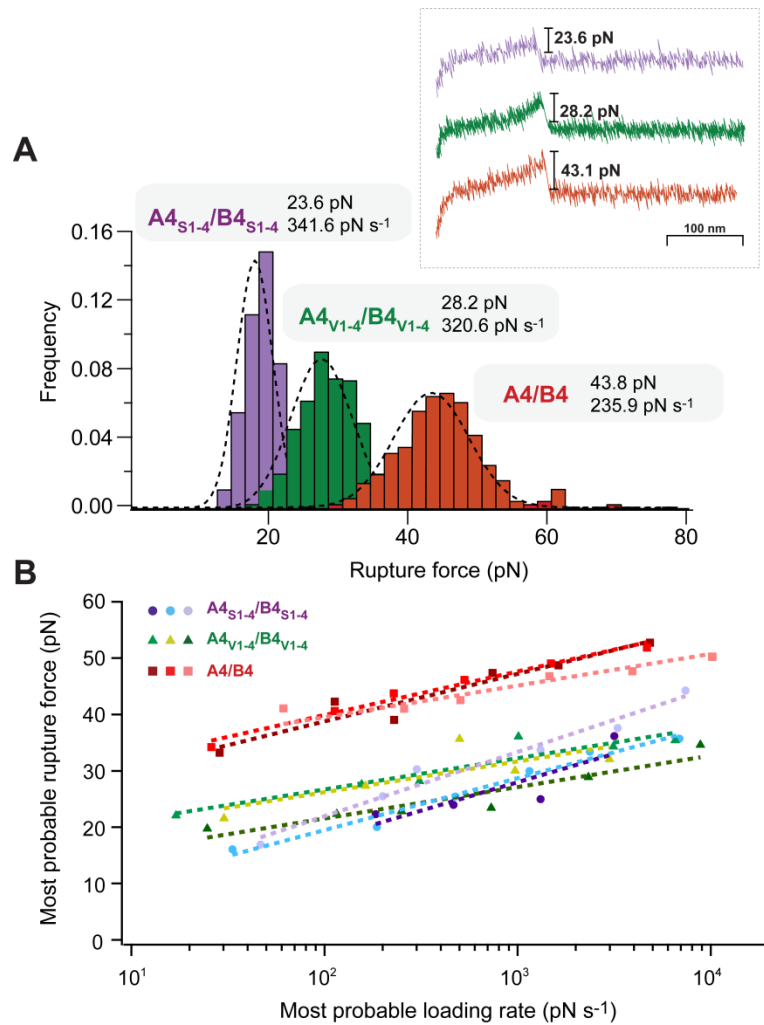
FIGURE 22 – Single-molecule force spectroscopy of A4/B4, A4$_{S1-4}$/B4$_{S1-4}$ and A4$_{V1-4}$/B4$_{V1-4}$. A) Rupture force histograms obtained at a retract speed of 400 nm s^{-1}. The *most probable rupture force* was determined using a Gaussian fit. The fit values are indicated in the figure as well as the corresponding loading rates, obtained from a Gaussian fit to the loading rate histograms (not shown). Characteristic force-distance curves of each Coiled Coil are depicted as an inset. B) Dynamic force spectroscopy diagram, incl. fits to the Bell-Evans model (dashed line). Each SMFS experiment was performed in triplicate (different shades of the same colour). The data for A4/B4 was published in [108] and was kindly provided by M. Goktas (MPIKG).

TABLE 9 - Summary of the kinetic and thermodynamic parameters obtained for A4/B4, A4$_{S1-4}$/B4$_{S1-4}$ and A4$_{V1-4}$/B4$_{V1-4}$. All parameters are depicted as mean ± SEM (n = 3).

	F* (pN)	$\Delta x_{F\text{-}TS}$ (nm)	k_{off} (s^{-1})	$\Delta G_{N\text{-}TS}$ (k$_B$T)
A4/B4	42.5	1.32 ± 0.15	(3.2 ± 2.1) x 10^{-4}	29.2 ± 1.4
A4$_{S1-4}$/B4$_{S1-4}$	25.4	0.93 ± 0.06	(2.8 ± 1.1) x 10^{-1}	21.3 ± 0.2
A4$_{V1-4}$/B4$_{V1-4}$	28.2	1.71 ± 0.01	(2.4 ± 1.7) x 10^{-3}	26.6 ± 0.7

F* = Most probable rupture force obtained at a retract speed of 400 nm s^{-1}.

CCs respond to an applied axial stretching force in three phases. Initially, the force increases linearly with extension and the helices remain intact (phase I). At a strain of 10-20

%, the individual helices start uncoiling at an almost constant force (phase II). In long CCs, the force increases sharply after the helices are uncoiled and the resulting structure is extended further (phase III).

Shearing of a 4-heptad CC initially causes the uncoiling of helical turns at the points of force application. It proceeds via the following competing processes: consecutive helix uncoiling, uncoiling-assisted sliding (refolding), and uncoiling-assisted dissociation of partially uncoiled helices (which may occur in phase I or at the transition to phase II) [108]. Uncoiling-assisted dissociation and, possibly, uncoiling-assisted sliding are the two processes that can occur in the loading rate range of a typical SMFS experiment. This mechanism has allowed for explaining the response of CCs of different length to shear forces, where it has been observed that shorter CCs are characterized by a higher k_{off} value and a shorter distance to the transition state $\Delta x_{N\text{-}TS}$.

Given the fact that the length is maintained constant in this work (4 heptads), the mechanics is entirely determined by CC sequence. The observed differences on k_{off} and $\Delta x_{N\text{-}TS}$ thus originate from the modifications in both α-helix propensity and hydrophobic core packing. The effect of these modifications will be explained in the following in relation to the mechanism explained above.

When replacing Ala in the *b* position with Ser, the α-helix propensity is lowered. Ala is the amino acid with the highest helix propensity due to its small side chain [76, 158]. For amino acids with longer side chains, the torsional angle between C_α and C_β (named X_1) causes a change in the helical Φ and Ψ angles, which can impede helix formation. In the case of Ser, helix structure is further influenced by its hydroxyl group, which can form a hydrogen bond with the carbonyl group in the next turn of the helix. This results in different torsional angles in comparison with other amino acids located in the helix.

Consequently, the Ala-Ser substitution reduces both the thermodynamic [159, 160] and mechanical stability of CCs. A reduced helix propensity thus means that the individual helices are 'easier' to uncoil. Combined with the fact that the CC is also less thermodynamically stable, this uncoiling weakens the CC even further. Overall, this causes dissociation already at smaller extensions. These underlying differences in the energy landscape are similar to what has previously been observed for CCs of different length. The deletion of one heptad (A_4B_3) increased k_{off} ($6.5 \times 10^{-3}\,s^{-1}$) and reduced the distance to the transition state (1.03 nm) in comparison with A_4B_4.

In the case of $A4_{V1\text{-}4}/B4_{V1\text{-}4}$, Val also has a lower helix propensity than Ile. Following the above line of argumentation, the k_{off} and $\Delta x_{N\text{-}TS}$ values are thus expected to lie between $A4/B4$ and $A4_{S1\text{-}4}/B4_{S1\text{-}4}$; however, this is only the case for k_{off}. $\Delta x_{N\text{-}TS}$ is larger than for $A4/B4$, suggesting an important role of the hydrophobic interface. The Ile-Val substitution loosens the core packing, as Val has a smaller side chain. It is expected that a less tightly packed hydrophobic core provides more degrees of freedom to the amino acid side chains. The contribution of this increased flexibility on the chain separation mechanism can then be explained as follows: during shearing, this pre-existing *flexibility* permits a rearrangement of

the Val side chains and possibly increases the probability of uncoiling-assisted sliding. This agrees with the so-called *mechanical softness* seen in other protein unfolding studies. Also for other proteins, it has been observed that destabilizing the hydrophobic core loosened the packed interface, thereby increasing both k_{off} and $\Delta x_{N\text{-}TS}$ [155, 161].
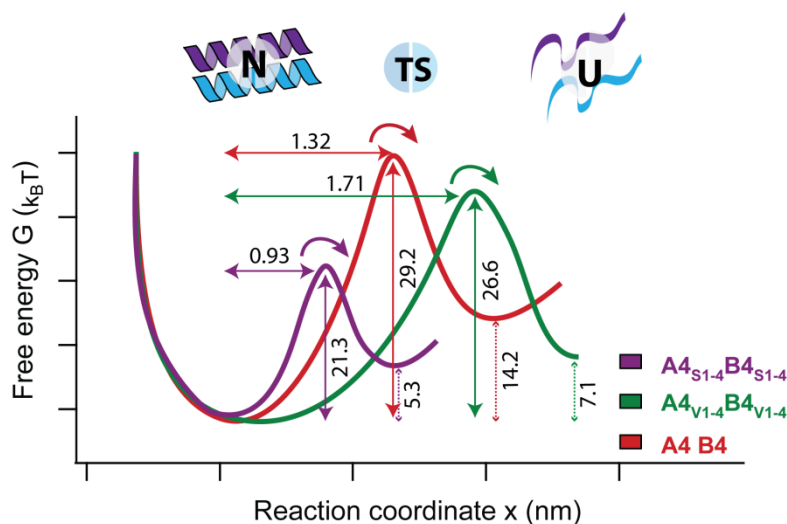

FIGURE 23 - Energy landscape of A4/B4, A4$_{S1\text{-}4}$/B4$_{S1\text{-}4}$ and A4$_{V1\text{-}4}$/B4$_{V1\text{-}4}$. Horizontal arrows represent $\Delta G_{N\text{-}TS}$, the distance from the folded (N) to the transition state (TS). Vertical solid arrows represent the energy barrier ($\Delta G_{N\text{-}TS}$) that the system has to overcome to unfold (chain separation). The dashed arrows show the free energy difference ($\Delta G_{N\text{-}U}$) between the folded and unfolded state.

In summary, the combination of helix propensity and hydrophobic core packing determines the mechanical stability of CCs; however, with different effects on the energy landscape (Figure 23). Whereas a reduced helix propensity decreases both the barrier height and the distance to the transition state, an increase in the transition state distance is obtained when decreasing the hydrophobic core packing. This part of this thesis thus establishes how the mechanical properties of a CC are specifically affected by the design parameters frequently used for tuning CC thermodynamic stability. These results are expected to allow for predicting and further tuning the mechanical stability of *de novo* designed CCs.

7.2.2. UNDERSTANDING THE ROLE OF INTERCHAIN IONIC INTERACTIONS

One additional design parameter utilized for CC design is the presence and positioning of interstrand ionic interactions that form between the *g* position of one heptad and the *e* position of the consecutive heptad in the neighboring helix [64, 128]. The relative contribution of these interstrand salt bridges to the thermodynamic stability of CCs has been debated [62]. Independent of their contribution to CC stability, they are crucial for initiating the folding process and for determining oligomerization specificity of CCs [6, 24, 62].

Here, I focus on the interstrand ionic interactions that define heterospecificity in A4/B4. Instead of modifying the CC sequence, the solvent conditions were altered to find conditions where ionic interactions are disrupted. In this way, the number of salt bridges can be modified without affecting the helix propensity of the CC. In A4 (acidic peptide), the charged amino acids are Glu in all *e* and *g* positions. In B4 (basic peptide) all *e* and *g* positions are occupied by Lys. The charged side chains possess a pK_A of 4.07 (Glu) and 10.53 (Lys). Lowering the pH below 4 thus protonates the carboxylic acid group of the Glu side chains, eliminating their negative charge. Increasing the pH above 10.5 deprotonates Lys, leaving a non-charged amino group. For a better comparison with the previous measurements of A4/B4 (PBS pH~7.4), phosphate was also used for the pH screening experiments. In particular, 10 mM phosphate pH~2.5 was used to protonate Glu. The different buffer conditions are shown in Table 6.

TABLE 10 – pH and salt screening of A4/B4. For each Coiled Coil the $\Theta_{222}/\Theta_{208}$ ratio is shown. $\Theta_{222}/\Theta_{208} > 1$ indicates a stable Coiled Coil. In some conditions, the A4 monomer shows self-assembly in the absence of B4, characterized by a prominent peak at 222 nm. The corresponding conditions are labelled with an asterisk.

Buffer	Concentration (additive)	pH~2.5	pH~7.4
PBS	-	-	1.016
10 mM NaH$_2$PO$_4$	-	0.972*	1.014
10 mM NaH$_2$PO$_4$ + NaCl	150 mM	1.097*	1.015
	5 M	1.535*	1.085
10 mM NaH$_2$PO$_4$ + NaClO$_4$	150 mM	1.194*	1.039
	5 M	1.025	0.970

In the acidic environment at pH~2.5, the amino group of Lys is positively charged and prevents homodimer formation of B4 (Figure 24). At the same time, the majority of Glu is protonated and able to form hydrogen bonds between Glu-Glu side chains. CD spectra of A4 alone show prominent minima at 222 nm (Figure 24B, D, F and H). This indicates the

formation of larger α-helical aggregates or fibril-like structures [74]. In the presence of B4, the majority of conditions yields more CC-like CD spectra even though the prominent minimum is also present in some conditions. It can thus not be concluded from these results if specific CCs are formed at pH~2.5. Altogether, it can be stated that the pH decrease leads to a destabilization of the ionic interactions between opposite charges, but also to the formation of other pH-driven structures.

To prevent the occurrence of other structures than CCs, salt screening was also performed, both at pH~2.5 and at pH~7.4. Using different concentrations of salts from the Hoffmeister series (Table 10), ionic interactions can be screened and/or hydrogen bonding between protonated Glu side chains can be prevented. The Hoffmeister series describes the ability of a series of ions to 'salt in' or 'salt out' proteins. Ions that enhance protein solubility are classified as kosmotropes. In contrast, ions leading to protein aggregation are termed chaotropes [162, 163]. Focusing on the chosen salts (NaCl and $NaClO_4$), the Na^+-cation and the Glu^- anion are kosmotropes therefore binding stronger to other kosmotropes or water than to the Cl^- anion, which is classified as chaotrope. The ClO_4^- anion is a stronger chaotrope, which binds to water or to other chaotropes (Lys^+). This results in a stronger screening of Lys^+ at pH~7.4 than is the case for the Cl^- chaotrope.

Therefore, when adding NaCl at pH~7.4, the strongest interactions that occur are between the kosmotropes Na^+ and Glu^-. This maintains A4 in a random coil conformation, except at high NaCl concentration. Under these conditions, fibers form (Figure 24G) because of the high amount of Na^+-cations, which also interact with water. B4, on the other hand, was α-helical because of the coulombic repulsions of the Lys^+ side chains in PBS pH ~7.4 conditions. At pH~2.5, Glu is not charged and Lys is positively charged. Now the strongest interaction (besides water-water) is between Cl^- or ClO_4^- and Lys^+. B4 thus adopts a more random coil conformation at low salt concentrations, whereas screening of Lys at high salt concentration leads to a α-helical structure spectrum. In all cases at pH~2.5, screening via Cl^- or ClO_4^- seemed to have little effect on the appearance of fiber-like structures. This result suggests that ClO_4^-, a strong chaotrope, has a stronger effect on CC folding than Cl^-. Most likely the Glu-Glu hydrogen bonding interactions are still stronger than the salt effect.

At high concentrations of $NaClO_4$ and pH~2.5, where the ionic interactions seem to be disrupted, both monomers and the CC were α-helical (Figure 24J). The CD spectrum of A4/B4 shows the two minima at 208 and 222 nm, with a ratio characteristic for a CC. Nevertheless, it remains unclear if the sample only contains A4/B4 heterodimers or if other species are present. This prohibits any further mechanical experiments.
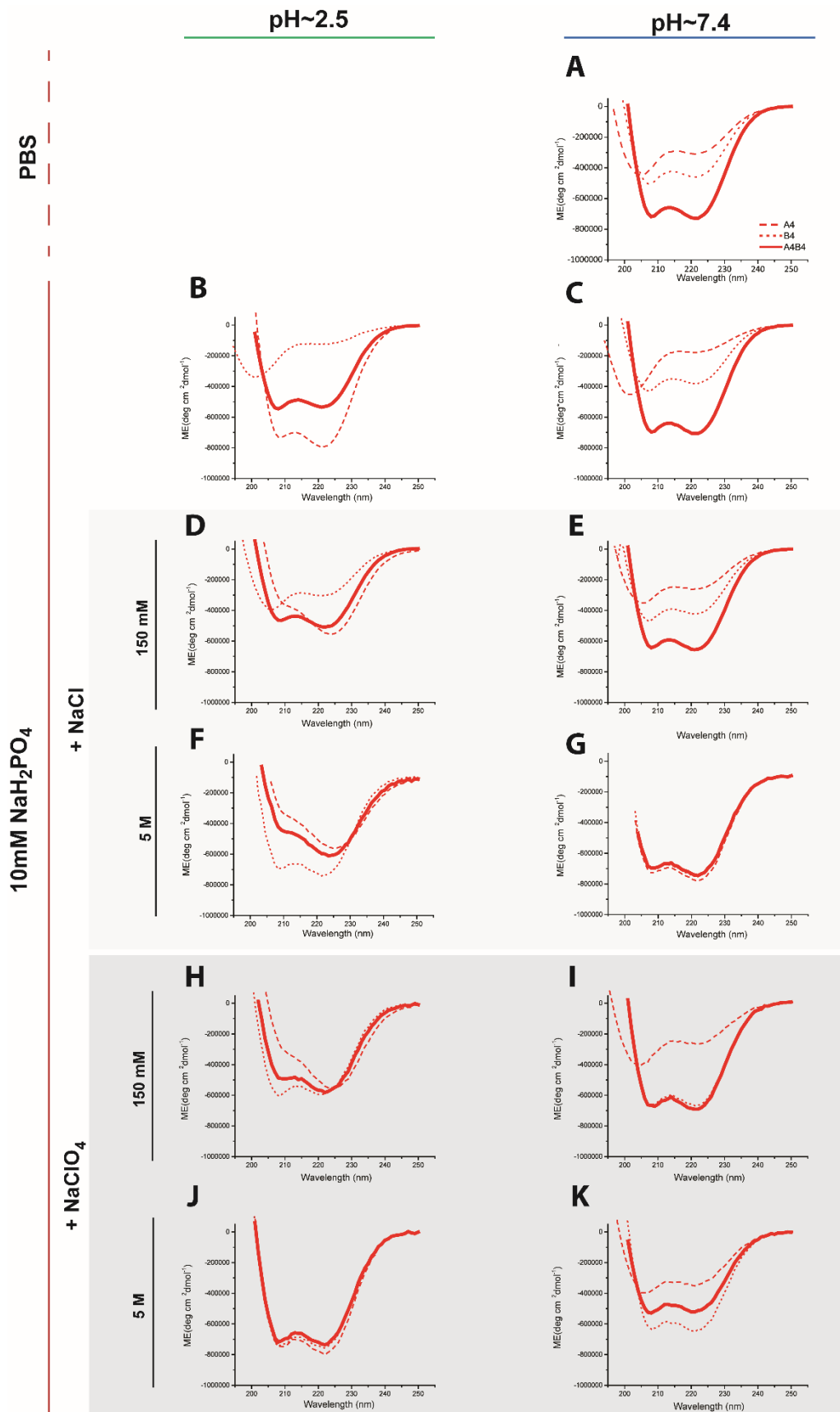
FIGURE 24 – CD spectra of A4/B4 in different buffers A-K) Comparison of the individual peptides (A4 - dashed line and B4 - dotted line) and a 1:1 mixture of A4 and B4 (solid line). Grey areas display the salt addition.

The modulation of the α-helical structure of a CC via altered environmental conditions (pH and salt type) is a well stablished strategy for the investigation of CC structural transitions [74]. Salt screening and pH modulation was, for example, investigated with the GCN4 leucine zipper. CC dimer formation was directed via protonation of Glu at pH≤6 or when introducing kosmotropic salts, which screen the Glu⁻ side chains at neutral pH [71]. Similarly, the addition of kosmotropes to a CC induced folding via changes in peptide-water interactions, leading to a stronger hydrophobic core.

Although no mechanical measurements were possible, various examples can be found in the literature that describe how ionic interactions determine protein mechanics. For instance, pH affects an ionic cluster in the GB1 protein, which is crucial for mechanical stability [164]. In another example, engineering an ionic cluster from a hyperthermophilic homologue into a protein with lower thermodynamic stability mechanically softened the structure (larger Δx_{N-TS}) [157]. It can be argued that ionic interactions contribute to the CC chain separation mechanism in a similar manner as the hydrophobic core. On the other hand, the salt bridges are partially solvent-exposed, most likely making a less strong contribution. Ionic interactions may, however, influence the process of (uncoiling-assisted) sliding. Upon sliding, the salt bridges in one heptad are broken and the charged side chains face new interactions in the neighboring heptad. If these new interactions are attractive or repulsive may have a large influence on the relative probability of sliding vs. uncoiling-assisted dissociation. Whether interhelical ionic interactions affect CC mechanical stability remains unanswered. Other strategies that could be followed to answer this question are the substitution of Glu for Gln, the chemical modification of Glu and Lys (e.g. using acetylation) or the repositioning of attractive and repulsive ionic interactions in the sequence.

Overall, ionic interactions are of fundamental importance for *de novo* CC design. Ionic interactions are frequently used for enhancing the thermodynamic stability of CCs [79] and for the development of specific pairs of orthogonal CCs, e.g. using charged blocks [70]. Charged amino acids are further involved in the formation of fibril-like structures [165] and in switching between CCs and amyloids as a function of pH [74]. Ionic interactions should therefore be considered for altering CC mechanical stability in future designs.

7.3. UNDERSTANDING THE INFLUENCE OF THE PULLING GEOMETRY ON COILED COIL MECHANICS

Having investigated how helix propensity and hydrophobic core packing affect CC mechanics, important parameters for the design of CCs with defined mechanical properties can be established. Another important design parameter is the pulling geometry. Depending on the points of force application, possible geometries that can be created are shearing, unzipping or tensile stretching. Moreover, for shearing and unzipping two different configurations exist. When the same sequence is maintained (Figure 25), the pulling geometry determines the force propagation pathway through the structure and thus the sequence of events leading to chain separation. In other words, the shape of the CC energy landscape is maintained, but chain separation follows a different path on the energy landscape. Hence, the following will be discussed in this section:

(1)   Comparison of the two possible shear geometries for the same sequence to investigate if and how the rupture forces and unfolding pathways differ when the points of force application are exchanged.

(2)   Comparison of the shear and unzip geometries for one and the same sequence to investigate how the altered pulling geometry affects the mechanical stability of the CC.
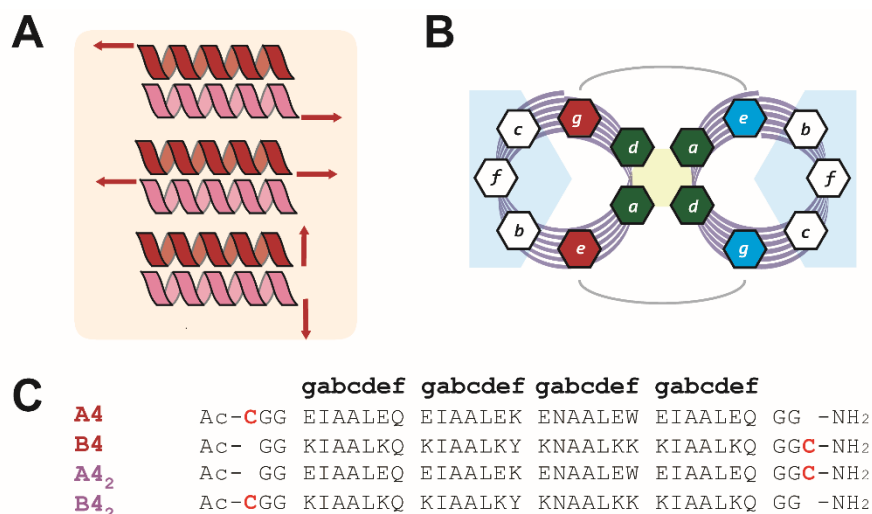


```
                gabcdef gabcdef gabcdef gabcdef
A4      Ac-CGG EIAALEQ EIAALEK ENAALEW EIAALEQ GG -NH2
B4      Ac- GG KIAALKQ KIAALKY KNAALKK KIAALKQ GGC-NH2
A42     Ac- GG EIAALEQ EIAALEK ENAALEW EIAALEQ GGC-NH2
B42     Ac-CGG KIAALKQ KIAALKY KNAALKK KIAALKQ GG -NH2
```

FIGURE 25 - Rational design of the Coiled Coils A4/B4, A4$_2$/B4$_2$ and A4$_2$/B4. A) Scheme of the pulling geometry used for each Coiled Coil (top: shear geometries A4/B4 and A4$_2$/B4$_2$; bottom: unzip geometry A4$_2$/B4). B) Helical wheel representing the front view of a heterodimeric parallel Coiled Coil. C) Sequences of the monomers included in this study. The pulling geometry is defined by the location of the terminal Cys residues.

7.3.1. EXCHANGE OF FORCE APPLICATION POINTS AT THE COILED COIL TERMINI (WHILE MAINTAINING SHEAR GEOMETRY)

When studying the effect of different pulling geometries on CC mechanical stability, the orientation of helix stabilizing hydrogen bonds and hydrophobic contacts with respect to the force vector needs to be considered. When comparing the two shear geometries, the overall orientation is not altered; however, CCs are asymmetric structures. The helices have an orientation and possess different helix propensities so that local differences in stability may be expected.

To answer the question if and how exchanging the force application points affects CC mechanics, the previously characterized sequence A4/B4 was used as the model system. The positions of the terminal cysteines were exchanged thus creating the new CC $A4_2/B4_2$: for A4, Cys was moved from the N-terminus to the C-terminus ($A4_2$), and vice versa in the case of B4 ($B4_2$). To validate that this modification does not affect the thermodynamic stability (shape of the energy landscape), the two CCs were first characterized with CD spectroscopy (Figure 26, Table 11).
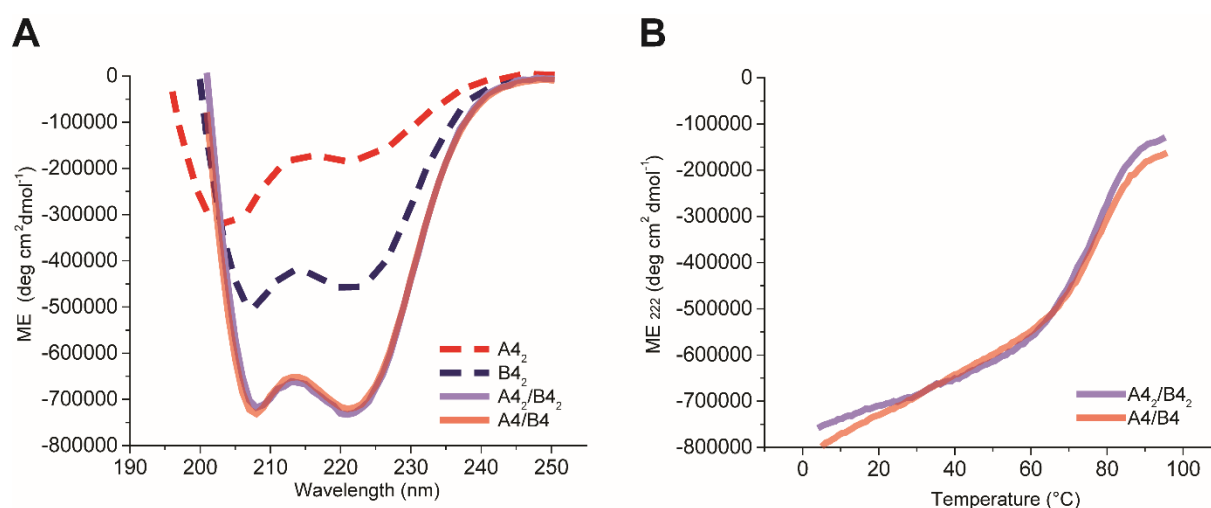

FIGURE 26 – CD spectroscopy of A4/B4 and $A4_2/B4_2$. A) CD spectra show the α-helical pattern of the two Coiled Coils (and the newly synthesized $A4_2$ and $B4_2$ peptides). The spectra, showing the characteristic minima at 208 and 222 nm, are virtually identical. B) CD melting curves measured at a wavelength of 222 nm. The curves are the average of three measurements.

As expected, both CCs show a $\theta_{222}/\theta_{208}$ ratio above 1, suggesting a well-defined CC structure. The different α-helix propensity scores given by AGADIR (Table 11) can be explained with the repositioning of the Cys residues in $A4_2/B4_2$. CD thermal denaturation experiments yield a similar melting temperature (T_m = 76.9 ˚C, in comparison with 77 ºC for A4/B4). Even though the free energy (ΔG_{N-U}) is slightly lower for $A4_2/B4_2$, it can be concluded that the two CCs possess a similar thermodynamic stability. The observed differences can most likely be attributed to the error of the measurements and the van't Hoff analysis. A comparison of all thermodynamic parameters is given in Table 11.

TABLE 11 - Thermodynamic characterization of A4/B4 and A4₂/B4₂. ΔG_{N-U}, ΔH and ΔS were obtained from van't Hoff plots. The AGADIR score reflects the α-helix propensity of each monomer (T = 298 K, ionic strength = 0.14 M, pH = 7.4 [78]). All parameters are calculated as mean ± SEM (n =3).

	AGADIR score	$\theta_{222}/\theta_{208}$	T_m (°C)	ΔG_{N-U} (k_BT)	ΔH (k_BT)	ΔS (k_B)
A4/B4	4.97/ 10.34	1.02	77.0 ± 0.3	14.2 ± 0.3	96.4 ± 2.1	0.28 ± 0.01
A4₂/B4₂	5.00/ 10.20	1.04	76.9 ± 0.9	10.7 ± 0.7	77.0 ± 5.3	0.22 ± 0.02

In contrast, the characterization of A4₂/B4₂ with SMFS yields significantly lower rupture forces in comparison with A4/B4 (Figure 27). For example, at a retract speed of 400 nm s⁻¹ the most probable rupture force decreases by ~15 pN. The Bell-Evans fit (Table 12) yields a similar k_{off} and a larger Δx_{N-TS} value (~0.6 nm). This suggests that the pathway leading to chain separation is indeed altered for the second shear pulling geometry. Interestingly, only the distance to the transition state is affected, while the barrier height is not changed.
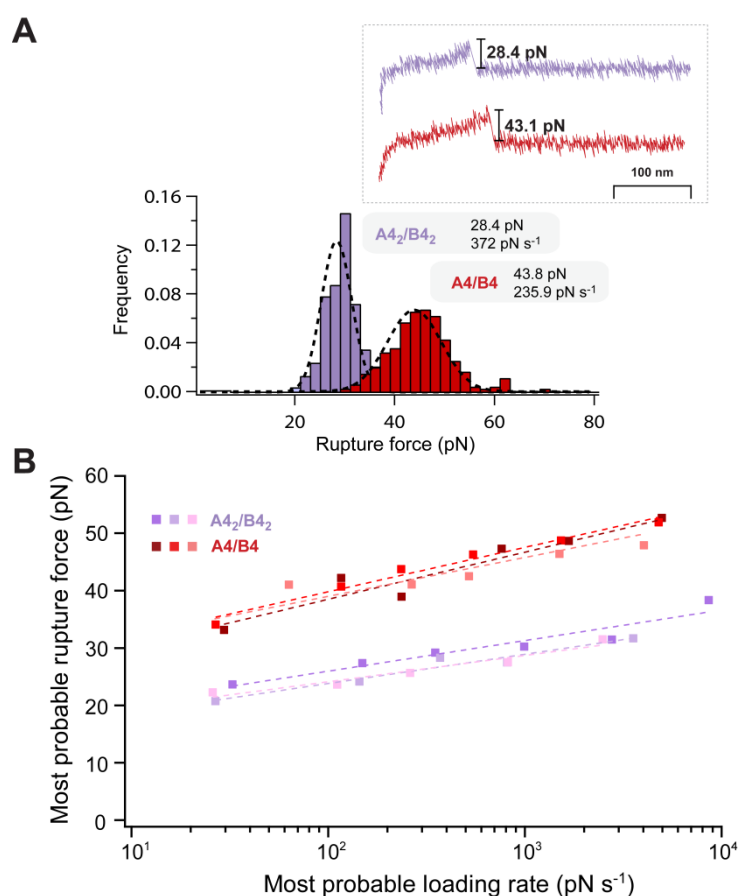

FIGURE 27 – Single-molecule force spectroscopy of A4/B4 and A4₂/B4₂. A) Rupture force histograms, obtained at a retract speed of 400 nm s⁻¹. The *most probable rupture force* is determined using a Gaussian fit (black dashed line). Characteristic force-distance curves for each Coiled Coil are depicted on top. B) Dynamic force spectroscopy diagram showing the Bell-Evans fit (dashed line). Each system was measured in triplicate, shown as different shades of the same colour. The data for A4/B4 was published in [108] and was kindly provided by M. Goktas (MPIKG).

It has been suggested earlier that proteins with closely related structure and function unfold at similar forces when mechanically loaded in the same geometry [99]. This does not appear to be the case for $A4_2/B4_2$ and A4/B4, two CCs that possess an identical energy landscape.

TABLE 12 - **Summary of the kinetic and thermodynamic parameters obtained for A4/B4 and $A4_2/B4_2$.** All parameters are depicted as mean ± SEM. Each system was measured in triplicate.

	$F^\star$ (pN)	$\Delta x_{N\text{-}TS}$ (nm)	k_{off} (s^{-1})	$\Delta G_{N\text{-}TS}$ ($k_B T$)
A4/B4	42.5	1.32 ± 0.15	(3.2 ± 2.1) x 10^{-4}	29.2 ± 1.4
$A4_2/B4_2$	28.4	1.89 ± 0.09	(6.0 ± 1.9) x 10^{-4}	27.6 ± 0.4

$F^\star$ = Most probable rupture force of one data set measured at a retract speed of 400 nm s^{-1}.

But how does this unfolding pathway differ between A4/B4 and $A4_2/B4_2$? As can be seen in Figure 28, the A- and B-peptides show clear differences in their α-helix propensities with local variations along the helices. The α-helix propensity is lowest in the proximity of the polar Asn-Asn pair, which in addition also destabilizes the hydrophobic core [57]. The Asn-Asn pair is located at position 18, which is closer to the C-terminus. Although the Asn-Asn pair compromises stability it may act as a *mechanical lock*, preventing a relative displacement of the helices in response to the applied force. It can be hypothesized that this *lock* crucially determines force propagation throughout the structure, leading to different unfolding pathways when the points of force application are exchanged. This in turn involves the rupture of different hydrogen bonds and hydrophobic contacts.
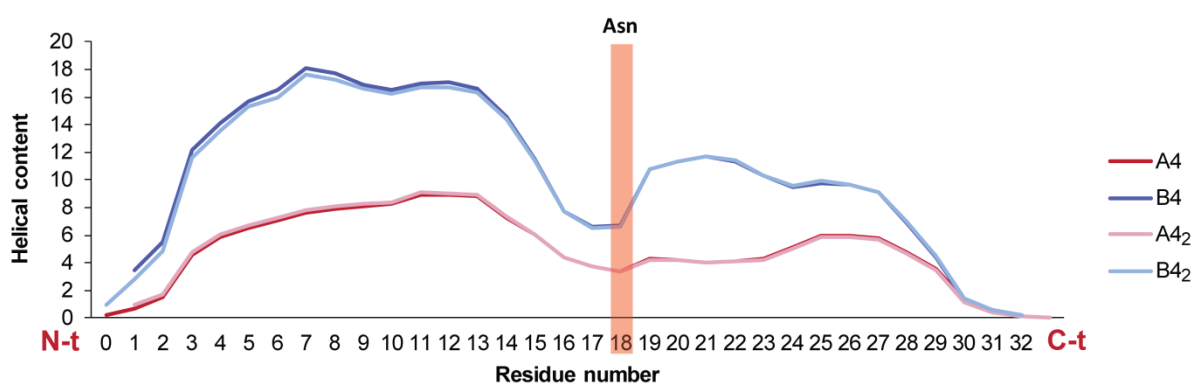

FIGURE 28 – Helical content per residue of A4, $A4_2$, B4 and $B4_2$ The Asn-Asn pair is located at position 18 in the 33 residue sequence. The helical content was calculated with AGADIR [78], using the following conditions: T = 298 K, ionic strength = 0.14 M, pH = 7.4.

Here, the A4-series peptides have a lower helix propensity than the B4-series peptides. In the case of $A4_2/B4_2$, the force is applied at the N-terminus of $B4_2$, which has a

very high helix propensity. At the same time, the force acts on the C-terminus of A4$_2$, which is the region with the lowest helix propensity. It appears likely that uncoiling initiates with a much higher probability at the C-terminus of A4$_2$ as less force is required to uncoil this part of the structure (compare to the Ala-Ser substitution). Uncoiling at the C-terminus then quickly propagates towards the Asn-Asn *lock*, affecting its stability. Increasing dynamics in this crucial position is expected to favor a relative displacement of the helices, which in turn leads to a larger Δx_{N-TS}. In the case of A4/B4, both termini have a similar helix propensity, suggesting equal probabilities for the uncoiling of A4 and B4.

In the same manner as chemical and mechanical denaturation can involve different and distinct unfolding barriers [166], two proteins with similar thermodynamic stabilities do not always unfold via the same pathways when a mechanical load is applied [167]. Moreover, research has already focused on how different pulling geometries (shear, unzip or tensile geometries) affect protein unfolding, involving different intermediates, rupture forces [97] and unfolding pathways [99]. For example, it has been observed that the direction of the applied force stabilizes different intermediates on the energy landscape of maltose binding protein (MBP). For this protein the unfolding forces range from 50 to 100 pN, depending on the amino acids where the force is applied [168].

Thus, it is clear that not only the amino acid sequence but also the pulling geometry determine the mechanical stability of CCs. Whereas the sequence defines the overall shape of energy landscape, the applied force determines the pathway leading to chain separation. Whether the decreased mechanical stability is the result of the non-symmetrical amino acid sequence (including the position of the Asn-Asn *mechanical lock*) can only be hypothesized and will need further experiments. Removing or relocating the Asn-Asn pair may ultimately answer this question in future experiments.

7.3.2. HOW DOES THE UNZIP PULLING GEOMETRY AFFECT COILED COIL MECHANICS?

As previously demonstrated, the shearing of a 4-heptad CC heterodimer requires forces between 15-50 pN for chain separation, depending on CC sequence and the points of force application. For a number of different CCs (GCN4 leucine zipper, vimentin, kinesin neck, LZ10 homodimer, etc.), unzipping forces were reported to be <15 pN. The question thus arises whether these low forces are a result of the pulling geometry or originated from the different sequences of these CC model systems. Therefore, using the well-established A4/B4 model system, a comparison between the shear and unzip geometries was performed. For this purpose, the A4$_2$ and B4 peptides were utilized, which both possess a Cys at the C-terminus. This new A4$_2$/B4 combination shows a similar thermodynamic stability compared to both A4/B4 and A4$_2$/B4$_2$, as expected (T_m = 76.7 °C; Figure 29 and Table 13).
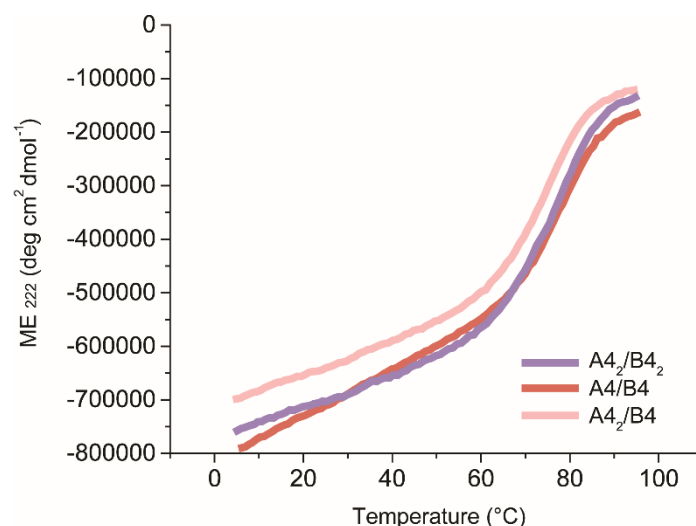
FIGURE 29 - Thermal denaturation curves of A4$_2$/B4$_2$, A4/B4 and A4$_2$/B4, measured at a wavelength of 222 nm. The curves show the average of 3 measurements.

SMFS of A4$_2$/B4 was difficult, as only a very small number of rupture events could be detected in the force-distance curves. Data collection was easier at the slowest retract speeds, whereas only very few rupture events were obtained at the highest retract speeds. Focusing on a retract speed of 50 nm s^{-1}, the most probable rupture force was 17.2 pN. When compared with A4/B4 and A4$_2$/B4$_2$ at the same retract speed, the rupture force is clearly lower (34.2 pN for A4/B4 and 20.8 pN for A4$_2$/B4$_2$, respectively). This result, although preliminary, is consistent with the work of Bornschlögl *et al.*, which showed that the unzipping of a GCN4 derivative with 10 helical turns (~5 heptads) fluctuates between 9 and 15 pN [129], while the tensile stretching of the same sequence reached a plateau of 25 pN [103]. Moreover, increasing the number of heptads or the loading rate did not significantly affect the unzipping force [129]. This is different for CC shearing, where a clear dependence on CC length and loading rate was observed [108]. This suggests that CC unzipping occurs closer to equilibrium, where the rupture forces are less strongly influenced by the loading rate.

TABLE 13 - Thermodynamic characterization of A4/B4, A4$_2$/B4$_2$ and A4$_2$/B4. ΔG_{N-U}, ΔH and ΔS were calculated from van't Hoff plots. The AGADIR score reflects the α-helix propensity of each monomer (A-series/B-series) for T = 298 K, ionic strength = 0.14 M, pH = 7.4 [78]. All parameters are calculated as mean ± SEM (n = 3).

	AGADIR score	$\theta_{222}/\theta_{208}$	T_m (^{0}C)	ΔG_{N-U} (k$_B$T)	ΔH (k$_B$T)	ΔS (k$_B$)
A4/B4	4.97/ 10.34	1.02	77.0 ± 0.3	14.2 ± 0.3	96.4 ± 2.1	0.28 ± 0.01
A4$_2$/B4$_2$	5.00/ 10.20	1.04	76.9 ± 0.9	10.7 ± 0.7	77.0 ± 5.3	0.22 ± 0.02
A4$_2$/B4	5.00/ 10.34	1.00	76.6 ± 0.9	12.3 ± 0.8	88.5 ± 5.5	0.25 ± 0.02

The current data thus reveals clear differences in the forces required for chain separation for shear vs. unzip geometries; however, this conclusion is only valid for the range of loading rates tested. It remains an open question if the chain separation forces would also be different when the CC structures are mechanically loaded under equilibrium conditions. For unzipping and shearing DNA molecules of a given sequence and thermodynamic stability, different forces are required at equilibrium. In the DNA case, the length gained upon shearing and unzipping is different and as a direct result also the forces are different. In other words, the work needed to rupture the DNA is the same so that a larger length increase automatically means that less force is required ($W = Fx$).

Turning back to the CC case, the data does not allow for answering this question, as neither the equilibrium force nor the length increase is known for the different pulling geometries. It is highly likely that the length increase is different, considering that the stabilizing interactions (hydrogen bonds and hydrophobic interactions) are aligned differently with respect to the force vector. In both cases, hydrogen bonds are probably broken before the rupture of a hydrophobic contact [111]; however, a force-induced relative displacement of the helices is most likely absent in the unzip geometry.
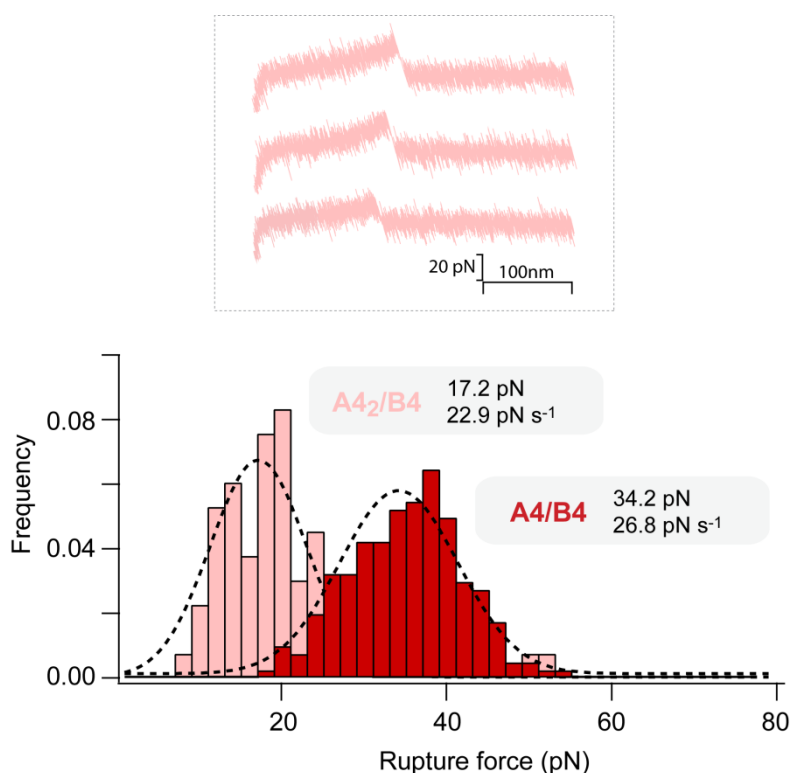

FIGURE 30 – Rupture force histograms of A4/B4 and A4$_2$/B4, measured at a retract speed of 50 nm s^{-1}. The *most probable rupture force* was determined using a Gaussian fit (black dashed line). Characteristic force-distance curves for the *unzipping* of A4$_2$/B4 are depicted on top. The data for A4/B4 was published in [108] and was kindly provided by M. Goktas (MPIKG).

Overall, even though this question remains unanswered, it has clearly been shown that the dynamic mechanical stability of one and the same CC sequence varies depending on

the pulling geometry. The pulling geometry determines the order of interactions that are broken, as well as the probability of helix sliding. These differences in the chain separation pathway can be used as an additional parameter when designing mechanically calibrated CCs for applications.

The previous sections have shown that α-helix propensity plays an important role in determining the thermodynamic and mechanical stability of CCs. Introducing amino acids with a lower α-helix propensity destabilized the CC and the local α-helix propensity may affect the sequence of events leading to chain separation. The next question that arises is how this knowledge can be used for designing CCs with increased stability. The A4/B4 reference system does already possess a high α-helix propensity as it contains Ala and Gln (i.e. amino acids with a high α-helix propensity) in most solvent exposed *b*, *c* and *f* positions. Substitutions with any other of the 20 natural amino acids are thus not expected to increase the global α-helix propensity of the CC any further. Instead, non-canonical modifications were used for increasing the helix stability in the A4/B4 model.
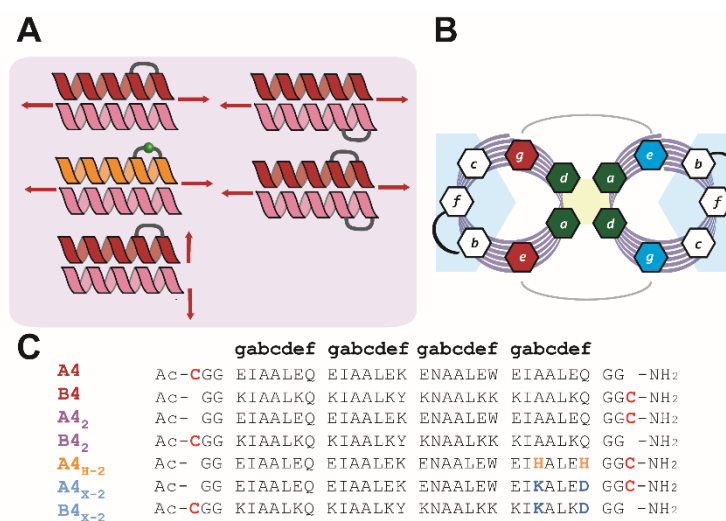
FIGURE 31 - Rational design of the Coiled Coils A4/B4, A4₂/B4₂, A4ₕ₋₂/B4₂, A4ₓ₋₂/B4₂, A4₂/B4ₓ₋₂, A4ₓ₋₂/B4ₓ₋₂, and A4ₓ₋₂/B4. A) Scheme of the additional Coiled Coils measured in this study (from top left to bottom right: A4ₓ₋₂/B4₂, A4₂/B4ₓ₋₂, A4ₕ₋₂/B4₂, A4ₓ₋₂/B4ₓ₋₂, and A4ₓ₋₂/B4). B) Helical wheel representing the front view of a heterodimeric parallel Coiled Coil. *Staples* are inserted at the b and f positions, shown as a solid black line. C) Sequences of the monomers included in this study. Modifications are depicted in bold.

External *staples* were inserted in the solvent-exposed residues of the helices (Figure 31) with the goal of locally stabilizing the helices against fraying (thermodynamic stability) and force-induced uncoiling (mechanical stability). A *staple* is an external linker coupled to the amino acid side chains at positions *i*, *i+4*. This linker thus bridges one helical turn and constrains the helix locally [88, 169]. Covalent and dynamic *staples* were compared with the goal of investigating their effect on the force-induced chain separation and ultimately of tuning CC mechanics in both shear and unzipping geometries. This section is divided as follows:

(1) Using A4₂/B4₂ as the starting point, a covalent lactam bridge was introduced to join two side chains in positions *i*, *i+4*. Focusing on the shear geometry, this staple was inserted at the force application point of the less helical peptide (C-terminus of A4₂). In a

second experiment, the staple was also inserted at the C-terminus of B4$_2$, which did not directly experience the applied shear force. This allowed for testing if the increased helix stability is transferred across the CC interface thereby stabilizing A4$_2$ in an indirect manner. In addition, the staple was inserted in both monomers to test for a possible synergistic effect.

(2) Again focusing on the shear geometry, the covalent bridge at the C-terminus of A4$_2$ was replaced with a reversible and dynamic metal-coordinating bridge (His-Ni^{2+}). This allowed for testing how the staple affects the chain separation mechanism and the energy landscape parameters of the CC under study.

(3) In addition to the shear geometry, the influence of the covalent lactam-bridge was also tested in the unzip geometry to evaluate possible differences between these pulling geometries when one helix is constrained at the force application point.

7.4.1. INSERTION OF COVALENT *STAPLES*

Covalent s*taples* were initially introduced with the goal of stabilizing α-helical peptides developed for medical applications. It is crucial that α-helices retain their conformation upon binding to a receptor [170]. Unfortunately, short helices are usually random coil in solution. The insertion of the *staple* thus increases the helicity of these peptides, thereby improving their binding kinetics. Reduced proteolytic cleavage and an increased cell permeability [171, 172] are additional benefits of this strategy.

The most frequently used *staples* [88, 173] are **all-hydrocarbon linkers** (Figure 34B), which were first synthesized by Verdine *et al.* [169]. To synthesize these linkers, O-allyl serine residues were introduced into the peptide sequence. In a second step, the side chains were crosslinked via ruthenium-catalysed ring closing metathesis (RCM) [174]. In addition to all-hydrocarbon linkers, other *staples* include photo-switchable **azobenzenes** [175], the palladium-catalysed crosslinking of aromatic amino acids [176] or non-natural side chains for **thiol-ene/thiol-yne** reactions [177, 178]. Also, **disulphide bridges** have been used [179]. In this work, the focus is on **lactam bridges** (Figure 32A), which form when crosslinking Asp and Lys residues (Figure 32B) [180]. The lactam bridge has been chosen, as it is formed from two natural amino acids and Lys-Asp (K-D) cyclisation can be performed on the resin during solid-phase peptide synthesis [181]. Combined with good water solubility, the K-D lactam bridge was further shown to be a good inducer of helicity in aqueous solvents [182].
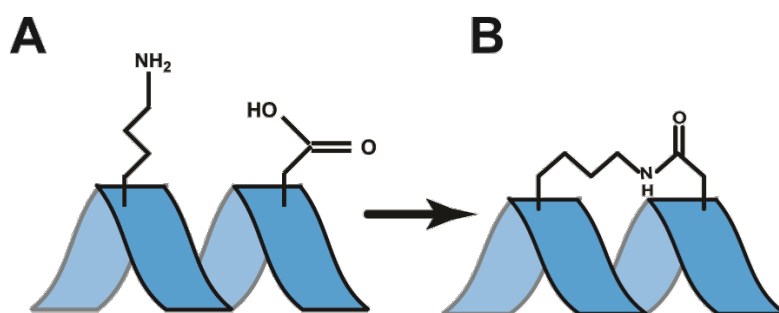
FIGURE 32 – Example of a *stapled* peptide. A) Lys and Asp side chains are displayed in one helical turn in (i, i+4) positions. Closing these side chains results in B), a Lys-Asp lactam bridge in (i, i+4) positions, therefore constraining one helical turn.

Considering that helix uncoiling is predicted to be the initial step leading to mechanically induced chain separation in the shear geometry [111], it was hypothesized that maintaining helicity imposes a higher energy barrier for this initial step and can, consequently, be used for tuning CC mechanics. To understand the exact role of the K-D lactam bridge [180, 182] in the chain separation mechanism, it was inserted at different positions of CC $A4_2$/$B4_2$ (Figure 31A): (1) the staple was placed directly at the point of force application (C-terminus of $A4_2$); (2) the staple was positioned at the C-terminus of the complementary monomer (C-terminus of $B4_2$), which is not feeling the force directly; and (3) both *staples* were combined to test for possible synergistic effects.
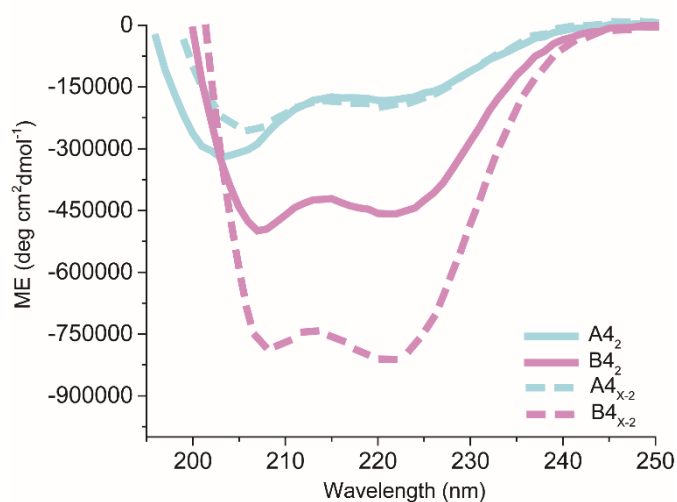

FIGURE 33 – CD spectra of $A4_2$, $B4_2$ and their *stapled* derivatives ($A4_{x-2}$ and $B4_{x-2}$). The *stapled* monomers show a more defined α-helical structure, as indicated by the shift of the first minimum to 208 nm.

To include the lactam bridge, the overall sequence of $A4_2$/$B4_2$ was maintained, except for the *b* and *f* positions (*i*, *i*+4) in the fourth heptad. Lys was inserted in the *b* position and Asp in the *f* position of the $A4_2$ and $B4_2$ peptides. The resulting *stapled* monomers are designated as $A4_{x-2}$ and $B4_{x-2}$. The helical content of the newly synthesized peptides was determined

with CD spectroscopy and compared to A4$_2$ and B4$_2$. The helical content of both peptides increases when the lactam bridge is inserted (Figure 33).
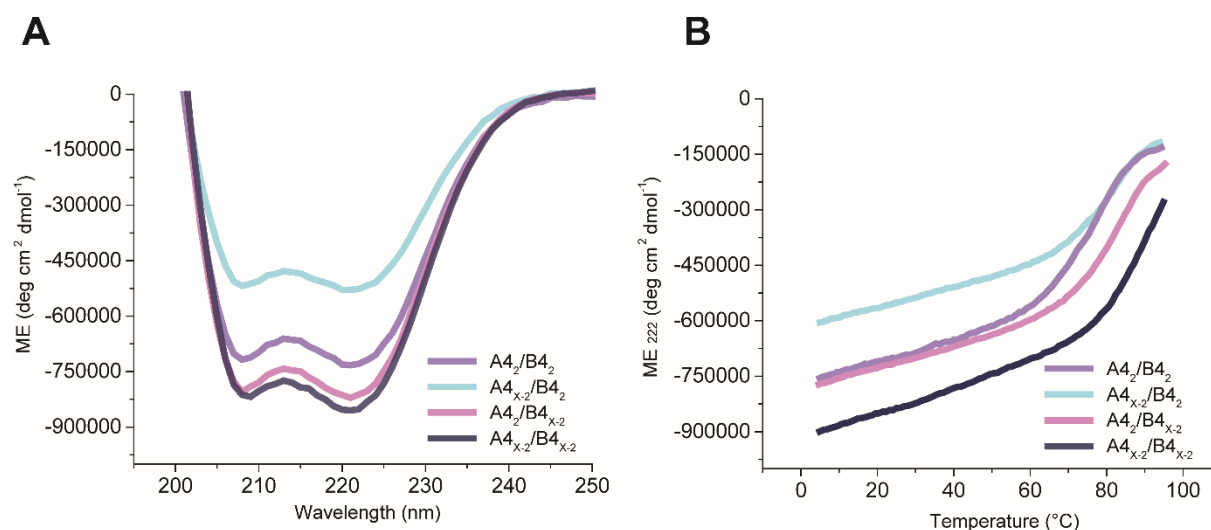

FIGURE 34 – CD spectroscopy of the A4$_2$/B4$_2$, A4$_{X-2}$/B4$_2$, A4$_2$/B4$_{X-2}$, and A4$_{X-2}$/B4$_{X-2}$ Coiled Coils. A) CD spectra show the α-helical pattern (characteristic minima at 208 and 222 nm) of the reference A4$_2$/B4$_2$ and the three *stapled* Coiled Coils. B) Temperature ramps measured at a wavelength of 222 nm.

TABLE 14 - Thermodynamic parameters of A4$_2$/B4$_2$, A4$_{X-2}$/B4$_2$, A4$_2$/B4$_{X-2}$, and A4$_{X-2}$/B4$_{X-2}$ Coiled Coils. ΔG_{N-U}, ΔH and ΔS were obtained from van't Hoff plots. The AGADIR score reflects the α-helix propensity of each monomer (A-series/B-series) for the conditions T = 298 K, ionic strength = 0.14 M, pH = 7.4 [78]. All parameters were calculated as mean ± SEM (n = 3).

	AGADIR score	T_m (^{0}C)	ΔG_{N-U} (k$_B$T)	ΔH (k$_B$T)	ΔS (k$_B$)
A4$_2$/B4$_2$	5.0/ 10.2	76.9 ± 0.9	10.7 ± 0.7	77.0 ± 5.3	0.22 ± 0.02
A4$_{X-2}$/B4$_2$	-	81.1 ± 0.0	14.2 ± 1.5	92.5 ± 8.5	0.26 ± 0.02
A4$_2$/B4$_{X-2}$	-	83.1 ± 0.9	14.9 ± 0.3	95.6 ± 4.0	0.27 ± 0.01
A4$_{X-2}$/B4$_{X-2}$	-	>95	16.5 ± 2.5	88.2 ± 13.0	0.24 ± 0.04

CD thermal denaturation further showed a higher thermodynamic stability (higher T_m) in the case of A4$_{X-2}$/B4$_2$, when compared with A4$_2$/B4$_2$. Likewise, the thermodynamic stability also increases for A4$_{X-2}$/B4$_{X-2}$ and A4$_2$/B4$_{X-2}$. This stability increase originates from the loss of conformational entropy at the termini (fraying) [183]. As expected, the CC with two *staples* (A4$_{X-2}$/B4$_{X-2}$) displays a higher stability (T$_m$ > 95 ºC), than the CCs with one staple (Table 14 and Figure 34B).

To test if preventing uncoiling at the terminus where the force is applied affects CC mechanics in the shear geometry, A4$_{X-2}$/B4$_2$ was investigated with SMFS. At one single retract speed of 400 nm s^{-1} the rupture force increased ~13 pN. The dissociation rate k_{off} was

slightly lower compared to the un*stapled* A4$_2$/B4$_2$ control, showing a small increase in the energy barrier height. At the same time, the distance to the transition state (Δx_{N-TS}) was reduced by ~0.5 nm. This suggests that constraining the helix at the force application point has an effect on the chain separation mechanism.
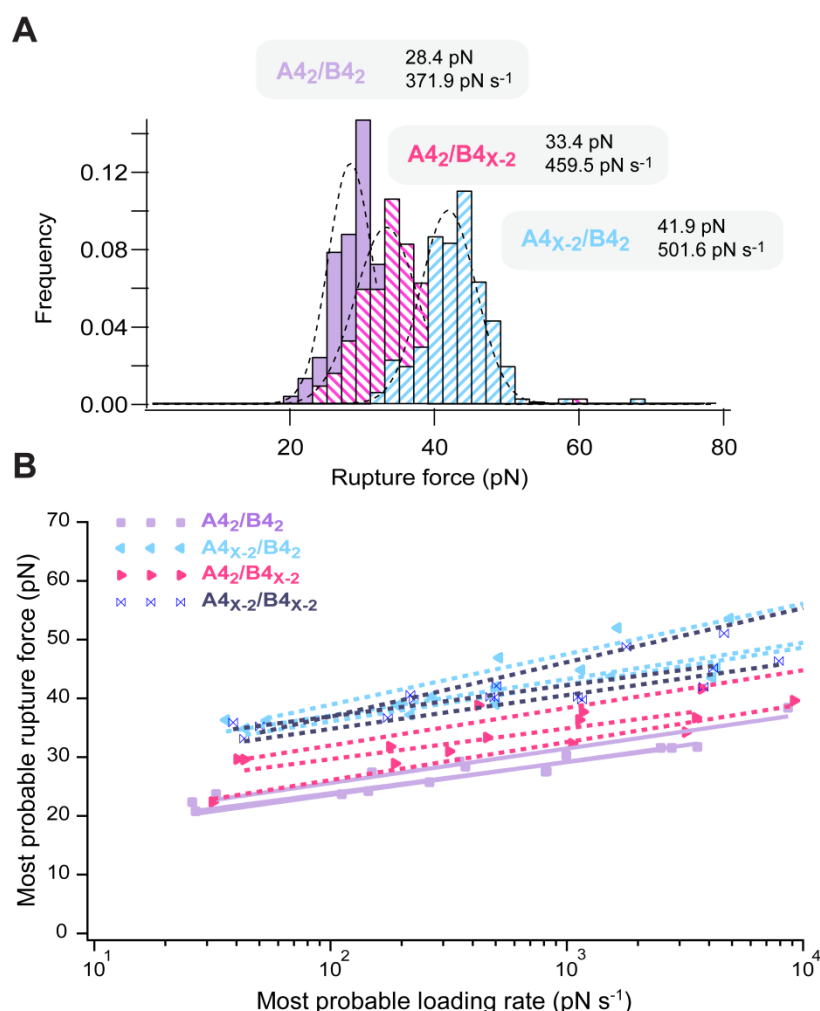

FIGURE 35 – SMFS of A4$_2$/B4$_2$, A4$_{X-2}$/B4$_2$, A4$_2$/B4$_{X-2}$ and A4$_{X-2}$/B4$_{X-2}$. A) Rupture force histograms obtained at a retract speed of 400 nm s^{-1}. The *most probable rupture force* was determined by a Gaussian fit (black dashed line). The histogram for A4$_{X-2}$/B4$_{X-2}$ is not shown as it largely overlaps with the histogram of A4$_{X-2}$/B4$_2$. B) Dynamic force spectroscopy diagram showing the Bell-Evans fit (dashed line for *stapled* systems, solid line for the non-*stapled* control). Each system was measured in triplicate.

When the force is applied at the *stapled* helical turn, helix uncoiling is prevented. This constraint forces the hydrophobic contacts to break without a preceding uncoiling step. This makes the structure less deformable and shortens the distance to the transition state. This mechanism was also observed in a molecular dynamics study by Bergues-Pupo *et al.* [130]. Constraining all dihedral angles of a heterotrimeric Coiled Coil, it was observed that preventing helix uncoiling increased the rupture force and reduced toughness when sheared. As k_{off} was much less affected when inserting the staple, this suggests that the increased CC stability observed for A4$_{X-2}$/B4$_2$ mostly originates from a shorter distance to the transition

state. Also in the experimentally investigated CC, the increased mechanical stability thus comes at the cost of a more brittle structure (Figure 35 and Table 15).

Having shown that the insertion of a covalent staple at the point of force application affects the unfolding mechanism, the next question was if the stabilizing effect of the staple only acts on the *stapled* helix or if it is also transferred to its binding partner. To answer this question, the staple was inserted at the C-terminus of the $B4_2$ peptide. In other words, does the staple in $B4_{X-2}$ maintain the helical structure of $A4_2$?

At a retract speed of 400 nm s^{-1}, the rupture force increased ~5 pN when compared to the non-*stapled* control $A4_2/B4_2$. This is a first indication that the staple does indeed have an indirect stabilizing effect on the CC, even though it is lower as when the staple is inserted directly at the force application point (Figure 35A). Also, the Δx_{N-TS} is shorter than in the control CC, but larger than for $A4_2/B4_{X-2}$, where the staple constrains the helix at the force application point. The dissociation rate k_{off} was a factor 1.5 higher than for the control $A4_2/B4_2$; however, this difference appears to be within the range of the error.

TABLE 15 - Summary of the kinetic and thermodynamic parameters obtained for $A4_2/B4_2$, $A4_{X-2}/B4_2$, $A4_2/B4_{X-2}$ and $A4_{X-2}/B4_{X-2}$. All parameters are depicted as mean ± SEM (n = 3).

	$F^\star$ (pN)	Δx_{N-TS} (nm)	k_{off} (s^{-1})	ΔG_{N-TS} (k_BT)
$A4_2/B4_2$	28.4	1.89 ± 0.09	(6.0 ± 1.9) x 10^{-4}	27.6 ± 0.4
$A4_{X-2}/B4_2$	41.9	1.37 ± 0.15	(2.4 ± 2.2) x 10^{-4}	28.9 ± 0.8
$A4_2/B4_{X-2}$	33.4	1.58 ± 0.12	(1.0 ± 0.9) x 10^{-3}	27.7 ± 1.1
$A4_{X-2}/B4_{X-2}$	40.2	1.48 ± 0.24	(9.0 ± 8.8) x 10^{-4}	29.5 ± 1.9

$F^\star$ = Most probable rupture force of one data set measured at 400 nm s^{-1}.

The observed trend suggests that both *staples* act via a similar mechanism, even though directly constraining the helix is more efficient. Most probably, the effect of the staple in $B4_{X-2}$ is transmitted to $A4_2$ via the hydrophobic core. It can be argued that the constrained C-terminus of $B4_{X-2}$, reduces the dynamics of the hydrophobic amino acids at the interface, which "is felt" by both the $B4_{X-2}$ and the $A4_2$ peptide. This in turn also stabilizes the C-terminal helical turns of $A4_2$, where the force is applied.

Finally, CC $A4_{X-2}/B4_{X-2}$ with two covalently *stapled* helices was tested to determine if these *staples* have any synergistic effect. In this case ΔF was ~12 pN in comparison to $A4_2/B4_2$. No further increase in the rupture force was seen in relation to $A4_{X-2}/B4_2$ (Figure 35). Also, the distance to the transition state and the dissociation rate were similar (Table 15). This shows that the second staple in $B4_{X-2}$ does not increase the mechanical stability any further than what can already be achieved with one staple inserted at the point of force application. Interestingly, the presence of a second staple did have an additional effect on the thermodynamic stability of these CCs. From a mechanical point of view, it thus appears

that the number of *staples* is not as important as their strategic position (e.g. their insertion directly at the force application points). It is thus expected that the mechanical stability can be further increased when the helices are *stapled* directly at both points of force application.

Comparing the staple with the use of canonical amino acids with different helix propensity, an apparent discrepancy is observed when considering the effect of the substitutions used on the distance to the transition state. In Section 7.2.1., the CC with the higher helix propensity (Ala vs. Ser) showed the larger distance to the transition state. Here, an increase in helix stability reduces the distance to the transition state. This seemingly contradicting result can be explained with the rather short CC length, so that helix uncoiling and sliding compete with dissociation perpendicular to the force axis. In comparison to A4/B4, $A4_{S1-4}/B4_{S1-4}$ has a low thermodynamic stability so that dissociation is highly likely already at very small deformations (increased k_{off} and reduced Δx_{N-TS}). In contrast, $A4_2/B4_2$ and its *stapled* derivatives do possess a high thermodynamic stability and chain separation requires larger deformations. This deformation is prevented by the staple, which alters the chain separation mechanism. Most likely, Ala would have a similar effect as a covalent staple in long CC sequences.

7.4.2. INSERTION OF METAL-COORDINATING *STAPLES*

The results obtained with the K-D lactam bridge prove that *staples* can be used for manipulating CC helicity and tuning CC mechanically stability. The largest effect was observed when the staple was used to constrain the CC at the force application point. Proof-of-concept experiments have already shown that the covalent staple can be replaced with a specific metal-coordination bond [184]. This non-covalent staple consists of two **histidines** in positions (i, i+4), which are able to coordinate transition metal ions, such as Ni^{2+}, Zn^{2+}, Co^{2+}, Cu^{2+}, etc. Using Ni^{2+} as the coordinating ion, it was shown that this non-covalent staple decreases k_{off}, while Δx_{N-TS} was not significantly reduced. As the metal-coordinating *staples* were inserted into a different CC sequence and their effect was investigated in a different buffer system, the goal of this section is thus to integrate these different observations and to understand possible differences between covalent and dynamic *staples*.

$A4_2$ was therefore used as a model for inserting the metal-coordinating staple, placing two histidines in the *b* and *f* positions of the fourth heptad (i.e. the same positions where the lactam bridge was located in $A4_{X-2}$). The newly designed peptide was named $A4_{H-2}$ (Figure 31). The bridge was formed when adding Ni^{2+} (in the form of $NiCl_2$) to the buffer. As phosphate ions in the previously used PBS buffer can coordinate metals, it became necessary to exchange the buffer into a non-coordinating buffer: piperazine-N,N'-*bis*(3-propanesulfonic acid (PIPPS-BS). The ionic strength and the pH of the buffer were maintained. As a control, $A4_2/B4_2$ was also measured in PIPPS buffer to determine possible buffer effects on CC properties.

To investigate the presence of the metal coordinating staple on the thermodynamic stability of $A4_{H-2}/B4_2$ and $A4_2/B4_2$, thermal denaturation experiments were performed in the

absence and presence of NiCl$_2$. Figure 36 shows two transitions for A4$_2$/B4$_2$. Most likely the first transition originates from weakly interacting homodimers, whereas the second transition represents the A4$_2$/B4$_2$ heterodimer. The T_m is difficult to extract for the second transition as the CC does not completely unfold in the accessible temperature range; however, it is clear that the T_m is higher in PIPPS-BS than in PBS.
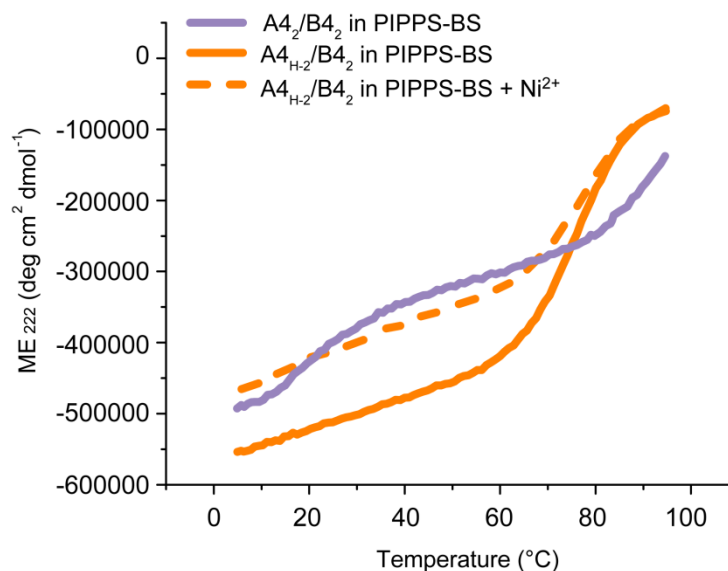

FIGURE 36 – Thermal denaturation of A4$_{H-2}$/B4$_2$ in the absence and presence of Ni^{2+}. For the measurement with Ni^{2+}, a NiCl$_2$ concentration of 150 µM was used. As a control, A4$_2$/B4$_2$ was measured in PIPPS buffer without Ni^{2+}. For A4$_2$/B4$_2$, the second transition was fitted to determine the T$_m$.

As a control for the *metal-coordinating staple,* the comparison between A4$_{H-2}$/B4$_2$ with and without Ni^{2+} is clearly most relevant (Figure 36) as it also considers the reduced helix propensity resulting from the incorporation of His (lower helix propensity score as shown in AGADIR, Table 16). When Ni^{2+} was added, the T_m increased ~2.5 °C (Table 16). Hence, from a thermodynamic point of view, the metal-coordinating staple adds a similar helix constraint in the fourth heptad of A4$_{H-2}$.

TABLE 16 - Thermodynamic characterization of A4$_{H-2}$/B4$_2$ in the absence and presence of Ni^{2+}. For the measurement with Ni^{2+}, a NiCl$_2$ concentration of 150 µM was used. A4$_2$/B4$_2$, measured in PBS and PIPPS-BS without Ni^{2+}, is shown as a control. ΔG_{N-U}, ΔH and ΔS were obtained from van't Hoff plots. The AGADIR score reflects the α-helix propensity of each monomer (A-series/B-series) for the conditions T = 298 K, ionic strength = 0.14 M, pH = 7.4 [78]. All parameters were calculated as mean ± SEM (n = 3).

	Buffer	AGADIR score	T_m (^{0}C)	ΔG_{N-U} (k_BT)	ΔH (k_BT)	ΔS (k_B)
A4$_2$/B4$_2$	PBS	5.0/ 10.2	76.9 ± 0.9	10.7 ± 0.7	77.0 ± 5.3	0.22 ± 0.02
A4$_2$/B4$_2$	PIPPS-BS	5.0/ 10.2	>95	-	-	-
A4$_{H-2}$/B4$_2$	PIPPS-BS	3.9/ 10.2	76.1 ± 0.1	12.5 ± 0.3	88.5 ± 1.6	0.25 ± 0.00
A4$_{H-2}$/B4$_2$	PIPPS-BS +Ni^{2+}	3.9/ 10.2	78.8 ± 1.1	15.0 ± 0.7	103.2 ± 6.1	0.29 ± 0.02

SMFS shows that the mechanical stability of A4$_{H-2}$/B4$_2$ increased ~9.5 pN in the presence of Ni^{2+} (400 nm s^{-1}), when compared to A4$_2$/B4$_2$ measured in PIPPS-BS (Figure 37 and Table 17). In contrast, the force increased ~13.5 pN for the covalently *stapled* peptide (A4$_{X-2}$/B4$_2$ vs. A4$_2$/B4$_2$, both measured in PBS; Table 17). The *metal-coordinating staple* thus acts in a similar manner as the covalent staple, even though the effect is less pronounced. The Bell-Evans fits (Table 17) also yield a shorter distance to the transition state (Δx_{N-TS}) and a decreased k_{off} in comparison to A4$_2$/B4$_2$, measured in PIPPS-BS.
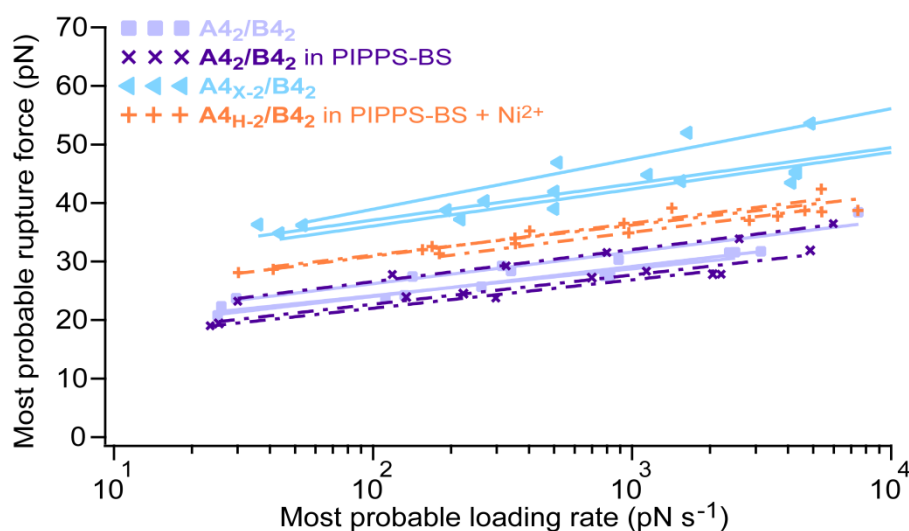

FIGURE 37 - Dynamic force spectroscopy diagram showing the Bell-Evans fit comparing lactam-bridge and metal-coordination staple (dashed line for Coiled Coils in PIPPS buffer, solid lines in PBS buffer). There is no mechanical difference when measuring A4$_2$/B4$_2$ in the different buffers. The mechanical stability of A4$_{H-2}$/B4$_2$ (measured in the presence of 1 mM NiCl$_2$) can thus be compared to both A4$_2$/B4$_2$ and A4$_{X-2}$/B4$_2$. Each system was measured in triplicate.

A quantitative comparison of the obtained fit values is difficult as the differences are not statistically significant in many cases. In addition, the covalent and the dynamic staple had to be measured in different buffers, which seemed to have an effect on the thermodynamic stability of the CC. Despite these uncertainties, both *staples* reduced the distance to the transition state (Δx_{N-TS}) in comparison to their controls and this reduction appears to be smaller for the dynamic staple. This can be explained as follows: the dynamic nature of the metal-coordinating staple allows opening while the CC is under load, subsequently facilitating helix uncoiling. Some CCs may thus rupture with an intact metal-coordinating staple, while the staple may have opened in other cases. The obtained Δx_{N-TS} value is thus derived from these two populations. It remains an open question whether staple opening and closing is a fast process in thermodynamic equilibrium or if the staple is ruptured mechanically. The latter would most likely result in an increased energy barrier (lower k_{off}), which cannot be unambiguously concluded from the data at hand. Taking into account the change of buffer, and the intrinsic dynamics of the metal-coordination bond, further experiments are needed to obtain better statistics.

TABLE 17 - **Summary of the kinetic and thermodynamic parameters obtained for $A4_{H-2}/B4_2 + Ni^{2+}$ and $A4_2/B4_2 - Ni^{2+}$.** The $NiCl_2$ concentration used was 1 mM. $A4_2/B4_2$ and $A4_{X-2}/B4_2$ (measured in PBS) are shown for comparison. All parameters are depicted as mean ± SEM (n = 3).

	Buffer	F* (pN)	Δx_{N-TS} (nm)	k_{off} (s^{-1})	ΔG_{N-TS} (k_BT)
$A4_2/B4_2$	PBS	28.4	1.89 ± 0.09	(6.0 ± 1.9) x 10^{-4}	27.6 ± 0.4
$A4_{X-2}/B4_2$	PBS	42.0	1.37 ± 0.15	(2.4 ± 2.2) x 10^{-4}	28.9 ± 0.8
$A4_2/B4_2$	PIPPS-BS	24.5	1.86 ± 0.07	(1.1 ± 0.2) x 10^{-3}	26.9 ± 0.3
$A4_{H-2}/B4_2$	PIPPS-BS + Ni^{2+}	34.0	1.74 ± 0.05	(1.3 ± 0.5) x 10^{-4}	29.2 ± 0.5

F* = Most probable rupture force of one data set measured at 400 nm s^{-1}.

Overall, these results again confirm that external *staples* can be used to tune CC mechanics. Comparing the dynamic metal-coordinating staple with a *covalent* staple suggests that both act in a similar manner, with the dynamic staple being opened while the CC is under load. This study thus represents direct proof that the initiation of helix uncoiling at the points of force application is the initial step leading to chain separation. It further shows that metal-coordination bonds are more dynamic and less mechanically stable than previously thought (e.g. rupture forces up to 300 pN have been proposed [185]) and that the nature of the staple can be used to alter the structural response of CCs to an externally applied force.

7.4.3. UNZIPPING OF A COVALENTLY *STAPLED* COILED COIL

By constraining individual helices at the point of force application, it has been demonstrated that the forces required for CC shearing can be tuned. This section focusses

on the effect of a covalent staple on CC unzipping. Using the same C-terminal force application points as in Section 7.3.2., the *covalent* lactam-bridge was inserted into A4$_{X-2}$. Considering that helix uncoiling also precedes the rupture of hydrophobic contacts in the unzip geometry, an increase in the rupture force is expected.
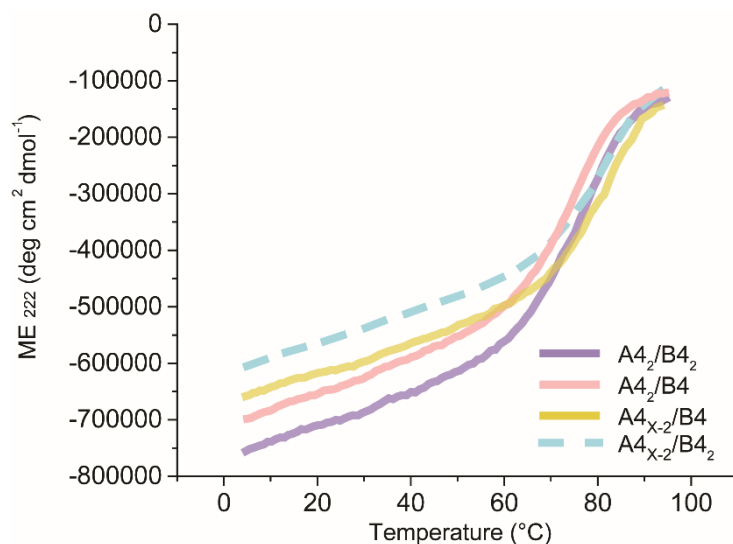

FIGURE 38 – Thermal denaturation of A4$_{X-2}$/B4 in comparison to A4$_2$/B4 (unzip geometry). For comparison, also the corresponding shear geometries (A4$_2$/B4$_2$ and A4$_{X-2}$/B4$_2$) are shown.

As expected, the insertion of the lactam bridge increased the T_m of A4$_{X-2}$/B4, in comparison to A4$_2$/B4 (Figure 38 and Table 18). Although the free energy ΔG_{N-U} seems to be slightly lower in the case of A4$_{X-2}$/B4, the error is high and suggests similar thermodynamic stabilities. Just as in Section 7.3.2, SMFS data was collected at the slowest retract speed only (50 nm s^{-1}). Preliminary results are shown in Figure 39. The most probable rupture force for this *stapled* CC was ~30 pN, while the same CC without staple ruptured at a force of ~17 pN (Table A9). The shape of the A4$_{X-2}$/B4 histogram displayed a second population, which coincides with the A4$_2$/B4 maximum. This might be a result of a small fraction of un*stapled* peptides in the A4$_{X-2}$ preparation (the fitted histogram is shown in Figure A13).

TABLE 18 - Thermodynamic characterization of A4/B4, A4$_2$/B4, A4$_{X-2}$/B4 and A4$_{X-2}$/B4$_2$. ΔG_{N-U}, ΔH and ΔS were obtained from Van't Hoff plots. All parameters were calculated as the mean ± SEM (n = 3).

	T_m (^{0}C)	ΔG_{N-U} (k$_B$T)	ΔH (k$_B$T)	ΔS (k$_B$)
A4/B4	77.0 ± 0.3	14.2 ± 0.3	96.4 ± 2.1	0.28 ± 0.01
A4$_2$/B4	76.6 ± 0.9	12.3 ± 0.8	88.5 ± 5.5	0.25 ± 0.02
A4$_{X-2}$/B4	82.5 ± 0.4	11.0 ± 1.2	74.7 ± 6.6	0.21 ± 0.02
A4$_{X-2}$/B4$_2$	81.1 ± 0.0	14.2 ± 1.5	92.5 ± 8.5	0.26 ± 0.02

The rupture force of A4$_{X-2}$/B4 (~30 pN) is similar to the rupture force of A4/B4 (~34 pN, shear, Figure 39) and A4$_2$/B4$_2$ (20.8 pN, Figure A7A), measured at the same retract

speed. Further, the shearing of the same *stapled* CC ($A4_{X-2}/B4_2$) occurred at ~35 pN (Table A9). Unzipping of a *stapled* CC thus requires much higher forces than unzipping its non-*stapled* counterpart. Surprisingly, these forces are almost identical with the forces required for shearing of the same CC. This outcome suggests once again that the resistance of the structure to helix uncoiling is highly crucial in both pulling geometries.
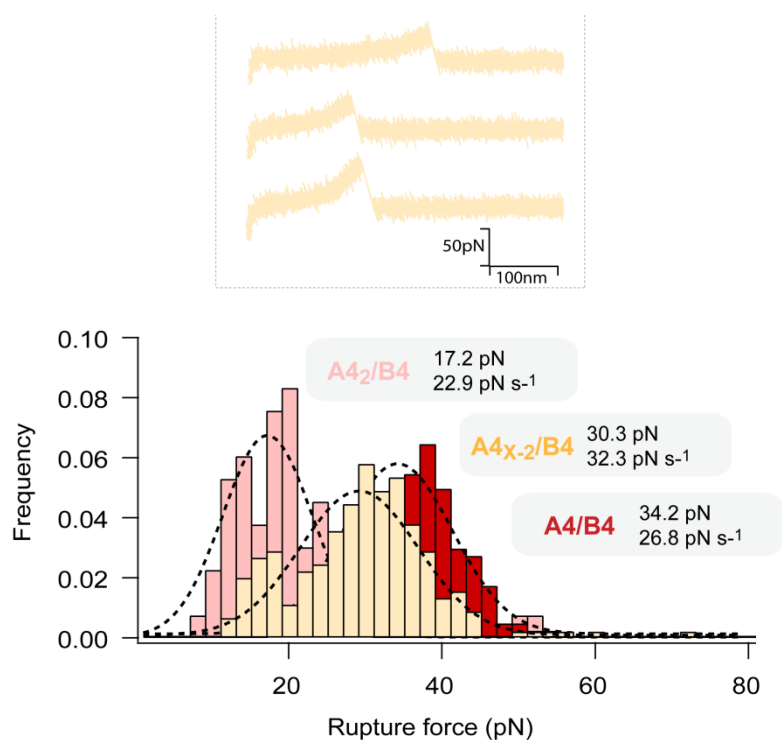

FIGURE 39 – Rupture force histograms of $A4_2/B4$, $A4_{X-2}/B4$ and $A4/B4$, measured at 50 nm s^{-1}. The *most probable rupture force* was determined using a Gaussian fit (black dashed lines). Characteristic force-distance curves of the *unzipping* of $A4_{X-2}/B4$ are depicted on top.

In more detail, the strong stabilizing effect of the staple confirms that also CC unzipping initiates with the unraveling of the helices at the force application points, followed by the rupture of the first hydrophobic contact [111]. The covalent staple prevents uncoiling of the $A4_{X-2}$ peptide (at least until the next heptad), which is the weakest point in the structure. In combination with the high local α-helix propensity of the C-terminus of B4 this part of the structure is strongly stabilized against uncoiling. One may even speculate that the insertion of the staple forces the simultaneous rupture of two hydrophobic contacts, which would otherwise break in a sequential manner. This should be different for metal-coordinating *staples*, provided that they dynamically open while the CC is under load. Measuring the metal-coordinating staple in the unzip geometry would thus be an additional test to confirm its dynamic nature.

7.5.   TUNING COILED COIL MECHANICS WITH FLUORINATED AMINO ACIDS

Using canonical amino acids, it was shown in Section 7.2.1 how modifications in the hydrophobic core affect CC mechanics. Specifically, the amino acids Val and Ile were compared in the *a* position. The hydrophobicity of the Val side chain is $\Delta g_t = 1.69$ kcal mol^{-1} while the Ile side chain has a hydrophobicity of $\Delta g_t = 2.97$ kcal mol^{-1} [186]. It was shown that the Ile-Val substitution loosened the packing at the hydrophobic interface. In combination with (de)solvation effects, the increased conformational degrees of freedom softened the CC structure [149] (increased distance to the transition state). In this section, non-canonical amino acids were inserted in the hydrophobic core with the goal of increasing the hydrophobicity at the CC interface. For this purpose, **fluorinated amino acids** were used, where hydrogen atoms are substituted by fluorine (Figure 40). It has already been shown that these modifications can increase the thermodynamic stability of CCs, even though steric packing effects seem to play an additional role [90, 187].
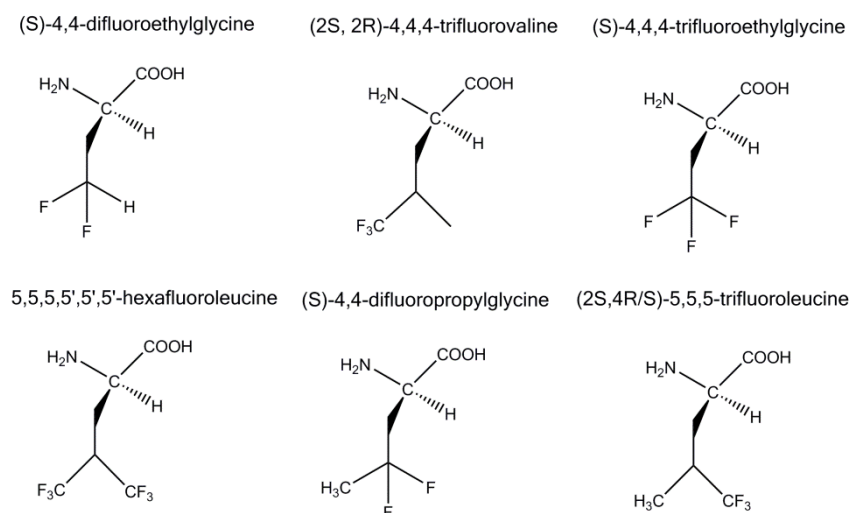
FIGURE 40 – **Examples of fluorinated amino acids**. Table 19 summarizes their effect on the properties of Coiled Coils.

Just as the development of *staples*, also amino acid fluorination was originally introduced with the goal of increasing the binding affinity in protein-protein interactions, e.g. by enhancing the hydrophobic segment of a helix. As the number of canonical hydrophobic amino acids is limited, the use of fluorinated analogues is a powerful strategy to increase and fine tune the hydrophobicity of binding motifs. Beyond hydrophobicity, additional parameters can be tuned, depending on the exact structure of the fluorinated amino acid. These include acidity, membrane permeability, reactivity and peptide conformation [90]. Fluorinated amino acids can be inserted into peptides via solid-phase peptide synthesis and into proteins during *in vivo* or *in vitro* expression [188].

Despite increasing interest, the effects of fluorine substitutions are not fully understood and depend on the functional group where the substitutions are carried out as well as on the number of substitutions. In general, it can be assumed that fluorine substitutions conserve the steric size of an amino acid side chain while increasing the hydrophobicity [189, 190]. Nevertheless, the C-F bond is slightly longer (0.4 Å) than the C-H bond [191] so that the volume does slightly increase, depending on the number of fluorine substitutions made. For example, the van der Waals volume of a fully substituted methyl side chain (CF_3) is twice the volume of CH_3 [192]. The observed increase in the thermodynamic stability seen for several proteins and peptides [90, 190, 193, 194] may be better explained with the *fluorous* effect, i.e. the tendency of fluorine to interact with another fluorine. In other words, fluorine atoms avoid interactions with other elements when other fluorine atoms are present. The reason for this effect is the low polarizability of fluorine [195].

When considering the structure of CCs, where fluorinated amino acids become part of the hydrophobic core, different effects may be observed (Table 19). These will again depend on the number of fluorine substitutions and their location. Clearly, the hydrophobicity and the fluorous effect will contribute. It also needs to be taken into account, however, that the incorporation of fluorinated amino acids may destabilize the core packing [194]. For example, a sole fluorine substitution was found to thermodynamically destabilize a CC, possibly because of the additional steric space occupied by this particular fluorinated amino acid [196]. In this context, also the position of the fluorinated amino acid (*a* or *d* position, central vs. terminal heptad) can be relevant. The local environment of a substitution [187] and the orientation of the side chains [89] is hence of utmost importance when introducing fluorinated amino acids into CCs.

TABLE 19 – Examples of fluorinated amino acid substitutions in different CC structures. The ΔT$_m$ values are obtained from a comparison to the non-fluorinated wildtype (negative values indicate destabilization).

Amino acid substitution [*original amino acid*]	Position (Number of substitutions/Length)	Structure	Thermostability (ΔT$_m$ in °C)	Reference
(2S, 4S/R)-5,5,5-Trifluoroleucine [*Leu*]	D (4/4 heptads)	bZIP GCN4 homodimer	13	[197]
(2S,3R)-4,4,4-Trifluorovaline [*Val*]	A (4/5 heptads)	bZIP GCN4 homodimer	4	[198]
(2S,3R)-5,5,5-Trifluoroisoleucine [*lle*]	A (4/5 heptads)	bZIP GCN4 homodimer	27	[198]
(3R)-4,4,4-Trifluorovaline [*Val*]	A (1/5 heptads)	VPE/VPK heterodimer	0.1	[193]
(3S)-4,4,4-Trifluorovaline [*Val*]	A (1/5 heptads)	VPE/VPK heterodimer	-3.2	[193]
(S)-4,4-difluoroethylglycine [*Val* if A] [*Leu* if D]	A (1/5 heptads) D (1/5 heptads)	VPE/VPK heterodimer VPE/VPK heterodimer	-11 -14.4	[89] [89]
(S)-4,4,4-trifluoroethylglycine [*Val* if A] [*Leu* if D]	A (1/5 heptads) D (1/5 heptads)	VPE/VPK heterodimer VPE/VPK heterodimer	-8.9 -16	[89] [89]
(S)-4,4,4-trifluoroethylglycine [*Leu*]	A (1/3 heptads)	homodimer	-14.9	[196]
(S)-4,4-difluoropropylglycine [*Val* if A] [*Leu* if D]	A (1/5 heptads) D (1/5 heptads)	VPE/VPK heterodimer VPE/VPK heterodimer	-8.6 -13.8	[89] [89]
5,5,5,5',5',5'-hexafluoroleucine [*Leu*]	D (1/5 heptads)	VPE/VPK heterodimer	3.7	[193]
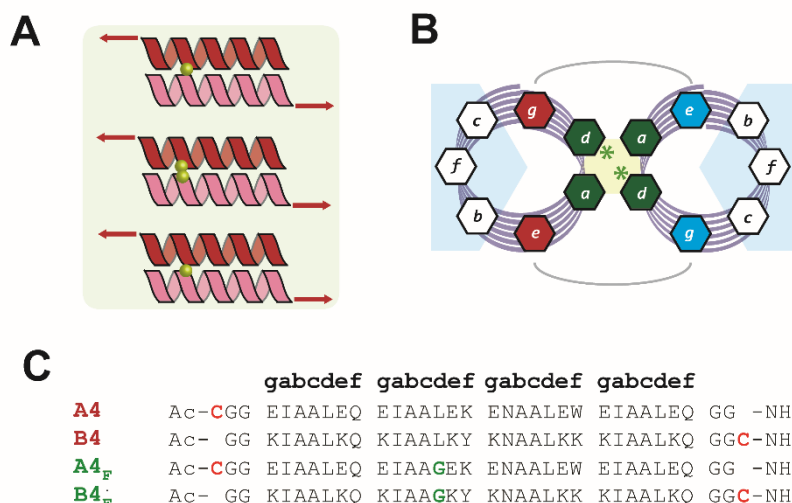
FIGURE 41 - Rational design of A4/B4, A4$_F$/B4, A4/B4$_F$ and A4$_F$/B4$_F$ Coiled Coils. A) Scheme of the Coiled Coils measured in this study (from top to bottom: A4$_F$/B4, A4$_F$/B4$_F$ and A4/B4$_F$). B) Helical wheel representing the front view of a heterodimeric parallel Coiled Coil, where (*) represents the location of the fluorinated amino acid. C) Sequences of the monomers included in this study. Modifications are depicted in bold. **G** = TFeGly.

In this section, the focus was on deciphering the effect of fluorinated amino acid insertion on the mechanical stability of the model CC A4/B4. The non-canonical fluorinated amino acid was used to replace Leu in position *d* of the second heptad of both A4 and B4. The amino acid chosen was **(S)-4,4,4-trifluoroethylglycine (TfeGly)**, which is similar in steric size to valine [199]. The new monomers were named A4$_F$ and B4$_F$, respectively.

Despite the higher hydrophobicity of TfeGly, all CCs containing either one (A4$_F$/B4 and A4/B4$_F$) or two (A4$_F$/B4$_F$) fluorinated amino acids were thermodynamically destabilized (Figure 42 and Table 20). Comparing A4$_F$/B4$_F$ with A4/B4, the TfeGly substitution decreases the T_m by 20.7 ºC. This result suggests that the *flourous effect* is small compared to a strong steric contribution, which destabilizes the hydrophobic core packing and makes the structure more dynamic. This may be further enhanced by the direct proximity to the Asn-Asn pair. When the substitution is made in only one monomer, the structure is destabilized less, confirming that the steric effect is the main factor. If the fluorous effect was the major contribution, the Leu/TfeGly pairings in A4$_F$/B4 and A4/B4$_F$ should be the least stable interactions.

The most stable fluorinated derivative A4/B4$_F$ (ΔT_m = -8 ºC with respect to A4/B4) was chosen for SMFS measurements to determine how the incorporation of TfeGly influences the mechanical stability of the CC and the chain separation mechanism. At one single pulling velocity of 400 nm s^{-1}, TFeGly incorporation decreased the mechanical stability by ~20 pN (Figure 43). As a direct result of the thermodynamic destabilization, the dissociation rate k_{off} increased by one order of magnitude in comparison to A4/B4 and the energy barrier height decreased by ~4 k$_B$T. The distance to the transition state increased ~0.4 nm in

comparison to A4/B4. In line with previous results, this is considered to originate from an increased preexisting *flexibility* at the CC interface.
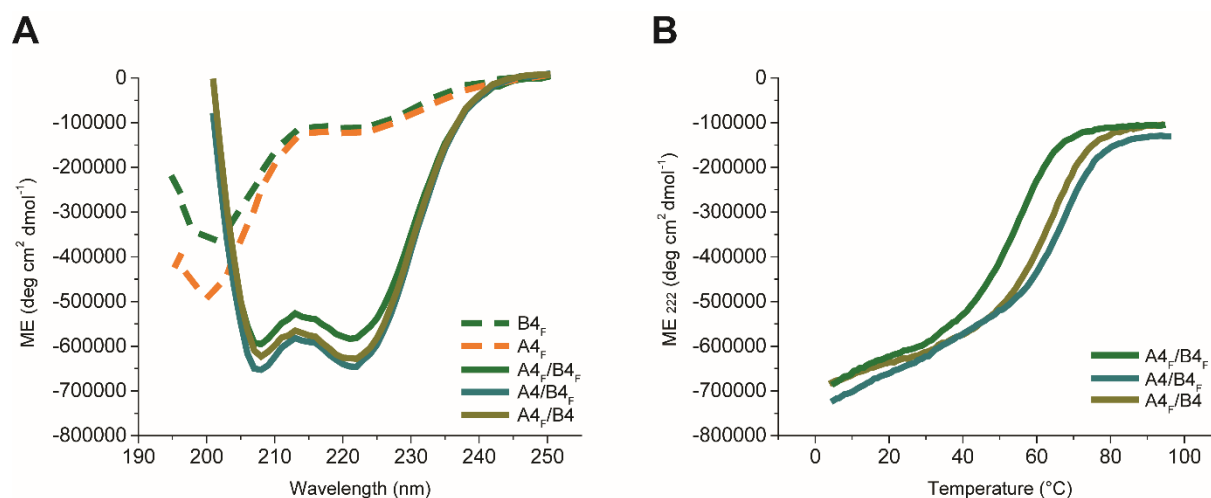

FIGURE 42 – Circular dichroism spectroscopy of A4/B4, A4$_F$/B4, A4/B4$_F$ and A4$_F$/B4$_F$. A) CD spectra show the random coil pattern of the fluorinated monomers and the α-helical pattern of the respective Coiled Coils. B) Thermal denaturation curves measured at a wavelength of 222 nm.

TABLE 20 - Thermodynamic parameters of A4/B4, A4$_F$/B4, A4/B4$_F$ and A4$_F$/B4$_F$. ΔG_{N-U}, ΔH and ΔS were obtained from van't Hoff plots. All parameters were calculated as mean ± SEM (n = 3).

	$\theta_{222}/\theta_{208}$	T_m (^{0}C)	ΔG_{N-U} (k_BT)	ΔH (k_BT)	ΔS (k_B)
A4/B4	1.016	77.0 ± 0.3	14.2 ± 0.3	96.4 ± 2.1	0.28 ± 0.01
A4$_F$/B4$_F$	0.977	56.3 ± 0.1	6.2 ± 0.2	68.3 ± 2.6	0.21 ± 0.01
A4$_F$/B4	1.008	65.3 ± 0.3	7.6 ± 0.3	69.4 ± 2.2	0.21 ± 0.01
A4/B4$_F$	0.990	68.9 ± 0.6	11.4 ± 0.9	92.1 ± 5.9	0.27 ± 0.02

Considering the k_{off} and Δx_{N-TS} values, it appears that the TfeGly substitution and the Ile-Val substitution in Section 7.2.1 (A4$_{v1-4}$/B4$_{v1-4}$) have a similar destabilizing effect on the hydrophobic core even though the number and nature of the substitutions is very different. In both cases, the energy barrier height is ~2 k_BT lower, the Δk_{off} increases by one order of magnitude and Δx_{N-TS} is ~0.4 nm larger. Even though a direct comparison is difficult, this suggests that a single TFeGly substitution in the *d* position of one chain is more destabilizing than six Ile-Val substitutions in the *a* positions of both chains.
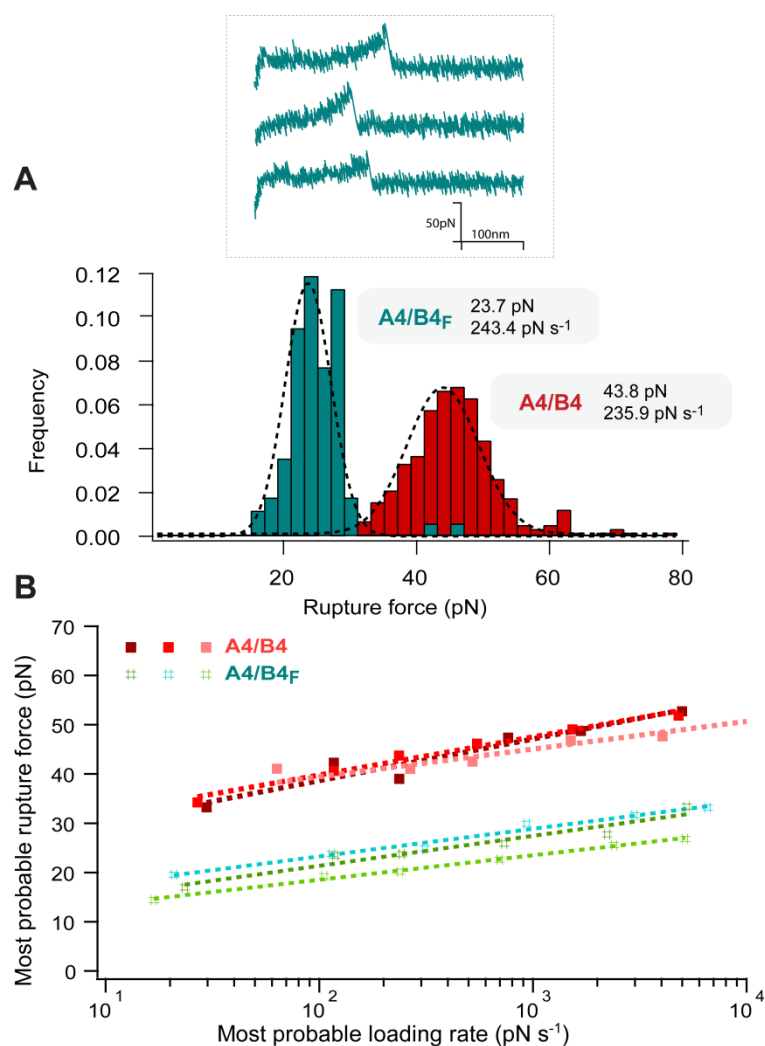
FIGURE 43 – Single-molecule force spectroscopy of A4/B4 and A4/B4_F. A) Rupture force histograms measured at a retract speed of 400 nm s^{-1}. The *most probable rupture force* is determined by a Gaussian fit (black dashed line). Characteristic force-distance curves for A4_F/B4 are depicted on top. B) Bell-Evans fit of the most probable rupture force vs. most probable loading rate. The data for A4/B4 was published in [108] and was kindly provided by M. Goktas (MPIKG).

Considering all thermodynamic and kinetic parameters, it is clear that the TfeGly-Leu substitution did not yield the desired outcome. Even though the substitution may have increased the hydrophobicity of the CC interface, this did not result in the thermodynamic and mechanical stabilization of the structure. Obviously other destabilizing factors overruled the fluorous and hydrophobic effects: (1) The steric shape and size of TfeGly does not fit the *d* position. With its three F substitutions, TfeGly possesses a similar steric size as Val [89, 187]. The van der Waals (vdW) volume of Val is 59.1 Å^3. In contrast, Leu has a vdW volume of 76.4 Å^3 [193]. TfeGly with a vdW of 42.8 Å^3 [89] is thus a better substitute for Val than for Leu, as it was performed here. Furthermore, Val is a β-branched amino acid, that usually occupies the *a* position in CC dimers. Hence, placing TfeGly in the *d* position may indeed be destabilizing [193]. (2) The environment of the fluorinated amino acid is critical. Here, TfeGly is sandwiched between a very strong hydrophobic contact (Ile-Ile) and the polar, hydrogen bonding Asn-Asn pair. In this environment, the fluorinated amino acid may

not be accommodated well so that the interface becomes destabilized. (3) The TfeGly-Leu pairing may contribute to this mechanical destabilization even further. Even though A4/B4$_F$ was more thermodynamically stable than A4$_F$/B4$_F$, its effect on the structural response to the applied shear force is unknown. This highly incompatible local environment may affect the conformational dynamics and relative displacement of the helices, thereby further contributing to the observed effect. Taken together, these three factors explain the large effect of one single TfeGly substitution on the stability of A4/B4$_F$.

TABLE 21 - Summary of the kinetic and thermodynamic parameters obtained from A4/B4, A4/B4F Coiled Coils. All parameters are depicted as the mean ± SEM (n = 3).

	F* (pN)	$\Delta x_{N\text{-}TS}$ (nm)	k_{off} (s^{-1})	$\Delta G_{N\text{-}TS}$ (k$_B$T)
A4/B4	42.5	1.32 ± 0.15	(3.2 ± 2.1) x 10^{-4}	29.2 ± 1.4
A4/B4$_F$	23.7	1.72 ± 0.10	(7.8 ± 2.6) x 10^{-3}	25.0 ± 0.4

F* = Most probable rupture force of one data set measured at 400 nm s^{-1}.

In summary, it can be concluded that the hydrophobicity is not the only parameter that determines the stability of the hydrophobic core. Tight interface packing (caused by favorable van der Waals contributions to hydrophobicity and lower access of water molecules to the interface [149]) is at least equally important and appears to be controlled more easily with canonical amino acid substitutions [200]. The insertion of non-canonical amino acids, which is much less studied, is much less predictable and may ultimately lead to destabilization. To further investigate the relative contribution of hydrophobic/fluorous and steric effects, global substitutions with fluorinated amino acids need to be carried out (i.e. in all *a* or *d* positions). Further, in the existing A4/B4$_F$ CC TfeGly should be moved to the *a* position. This will be the sterically more conserved substitution and will move the fluorinated amino acid further away from the Asn-Asn pair. Further research is required to understand the interplay between packing and the hydrophobic/fluorous effect on CC mechanics.

8. CONCLUSIONS

Over many years, Coiled Coils (CCs) have served as model systems for understanding protein folding and stability. Moreover, various applications have been developed, e.g using CCs as highly specific binding partners in biotechnological and therapeutic applications or as building blocks in biomaterials. Considering their natural function as structural and mechanical building blocks, it is highly crucial to extend previous studies and to understand how CC sequence and structure determine the mechanical properties of CCs. This information will aid a more detailed understanding of their function in tissues. It will also establish CCs as nanomechanical building blocks, in a similar manner as DNA [118, 201, 202]. To date, no systematic mutation analysis has been performed to establish the **sequence-structure-mechanics relationship** of CCs. In this work, different substitutions with canonical and non-canonical amino acids have been performed to determine their effect on the mechanical stability of CCs and to establish if and how thermodynamic and mechanical stability are correlated. Mechanically loading the CC in the shear or unzip geometry, it was tested how helix stability, hydrophobic core packing and ionic interactions determine the response of the CC to the externally applied force:

$\Rightarrow$ Using well-characterized canonical sequence modifications and buffer exchange, the influence of the helix propensity, hydrophobic core packing and ionic interactions was investigated. Using the shear pulling geometry, it was shown that a reduced helix propensity and a less densely packed core affect the thermodynamic stability similarly; however, that the underlying energy landscape is different. A reduced helix propensity increased the dissociation rate k_{off}, accompanied by a decrease in the distance to the transition state Δx_{N-TS}. In contrast, a less densely packed hydrophobic core had a smaller effect on k_{off} while Δx_{N-TS} was increased. The effect of salt bridges could not be measured as modifications in the charged amino acid lead to a loss of heterodimer specificity.

$\Rightarrow$ Using the same sequence, the role of the force application point was investigated. Repositioning the Cys residues used for immobilization, two shear geometries and one unzip geometry were compared. It was confirmed that CCs rupture at lower forces when loaded in the unzip geometry. Focusing on the shear geometries, it was shown that shearing from different termini proceeds via different pathways. The most likely explanation is the asymmetry of the CC, defined by different helix propensities of the individual chains as well as the position of the Asn-Asn pair. It appears likely that the Asn-Asn pair plays a critical role in the mechanical displacement of the CC chains when sheared.

$\Rightarrow$ Assuming that uncoiling of both helices is the first step towards mechanical chain separation, the force-loaded termini were reinforced with covalent and dynamic *staples*. This increased the mechanical stability of the CC in the shear geometry, mostly

originating from a shortened $\Delta x_{N\text{-}TS}$. The covalent staple caused a larger decrease in $\Delta x_{N\text{-}TS}$, suggesting that the dynamic, metal-coordination staple opens up while the CC is under load. The covalent staple further increased the mechanical stability of the CC in the unzip geometry, confirming that helix uncoiling proceeds the rupture of hydrophobic contacts in both pulling geometries.

$\Rightarrow$ Using fluorinated amino acids, it was investigated if an increased hydrophobicity at the hydrophobic core (combined with the fluorous effect), can mechanically stabilize the CC. Replacing Leu in the *d* position of the second heptad with TfeGly, the desired increase in the mechanical stability was not obtained. Instead, it was observed that this particular substitution destabilized the tightly packed core, as evidenced by an increased $\Delta x_{N\text{-}TS}$. Similar to what was observed for the substitution with less tightly packed canonical amino acids, the dynamics at the interface was increased, which allows larger deformations prior to chain separation.

To generalize these findings and to establish a relationship between sequence, structure and mechanics, the results were divided into three categories: helix propensity, hydrophobic core and pulling geometry. The differences in k_{off} and $\Delta x_{N\text{-}TS}$ were calculated with respect to their specific control (Table 22 and Figure 44).

TABLE 22 – Summary of the kinetic parameters of all CCs. The values show the relative difference between the Coiled Coil mentioned and its respective control. The colour code refers to the respective design parameter: Orange, helix propensity; green, hydrophobic core; blue, pulling geometry.

Sequence	Control	$\Delta k_{off}(s^{-1})$	$\Delta\Delta x_{N\text{-}TS}$ (nm)	$\Delta F^{\star}$ (pN)	ΔT_m (°C)
$A4_{S1\text{-}4}/B4_{S1\text{-}4}$	A4/B4	0.28282	-0.39	-17.1	-22.7
$A4_{X\text{-}2}/B4_2$	$A4_2/B4_2$	-0.00030	-0.52	13.6	4.2
$A4_2/B4_{X\text{-}2}$	$A4_2/B4_2$	0.00064	-0.32	5.0	6.1
$A4_{X\text{-}2}/B4_{X\text{-}2}$	$A4_2/B4_2$	0.00030	-0.42	11.8	19.5
$A4_{H\text{-}2}/B_2$ PIPPS-BS $+Ni^{2+}$	$A4_{H\text{-}2}/B_2$ PIPPS-BS	-	-	-	2.8
$A4_{H\text{-}2}/B_2$ PIPPS-BS $+Ni^{2+}$	$A4_2/B4_2$ PIPPS-BS	-0.00096	-0.12	9.5	-
$A4_{V1\text{-}4}/B4_{V1\text{-}4}$	A4/B4	0.00214	0.39	-14.4	-18.0
$A4/B4_F$	A4/B4	0.00743	0.40	-18.8	-8.0
$A4_2/B4_2$	A4/B4	0.00028	0.58	-14.2	-0.1

$\Delta F^{\star}$ = Difference in the most probable rupture force at 400 nm s^{-1}.

The results show that increasing the **stability of the individual helices** stabilizes the overall CC. This can either be achieved with substituting amino acids with a higher helix propensity or with the insertion of *staples* at the points of force application. As the staple makes helix uncoiling less likely or even prohibited, this makes the structure more brittle as

evidenced by a shorter distance to the transition state. The dissociation rate is either unaffected or slightly reduced as the higher helix stability increases the energy barrier height. This general observation is confirmed by molecular dynamics simulations carried out for a CC heterotrimer, where the dihedral angles of all peptide bonds were constrained [130].

Interestingly, a shortening of the distance to the transition state can also occur for CCs with a very low helix propensity (Ala-Ser substitution), even though a longer distance to the transition state may be expected. In the 4-heptad CC used, the lower helix propensity significantly reduced the thermodynamic stability (see the significantly increased k_{off} in Table 22 and Figure 44). As a result, dissociation without significant uncoiling became more likely, as also observed when the same CC was shortened from 4 to 3 heptads [108]. In summary, increasing the helix stability thus has two different competing effects: (1) it enhances the thermodynamic stability, leading to a higher k_{off} and longer Δx_{N-TS}. (2) At the same time, it affects the process of helix uncoiling. Above a certain stability threshold, this effect becomes visible as a shorter Δx_{N-TS}, as observed for the *stapled* CCs.
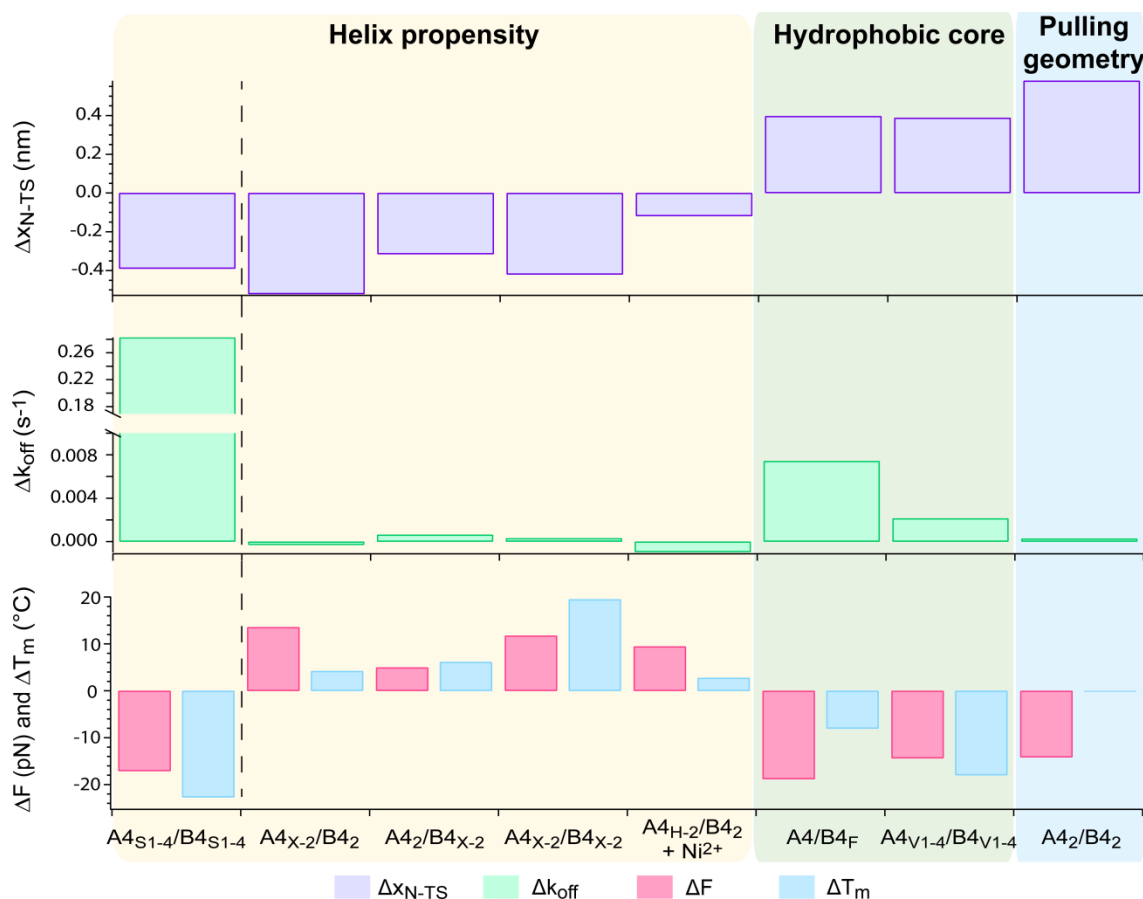
FIGURE 44 – Summary of the relative differences in kinetic values, split into different categories: modulation of the helix stability, hydrophobic core modifications, and pulling geometry.

Substitutions that destabilize the **hydrophobic core** lead to a longer distance to the transition state Δx_{N-TS} and a slightly increased dissociation rate k_{off}. This result is independent of the exact nature of the modification (canonical Ile-Val substitution vs.

insertion of TfeGly). This suggests that the chemical nature of the substituted amino acids affects the hydrophobic core less than possible consequences on side chain packing and dynamics. A less tight and/or ordered core packing leads to more flexibility at the interface and allows larger rearrangements of the side chains when shearing the CC. As a result, a larger relative displacement of the helices is facilitated than with a more ideal knobs-into-holes-packing. This may be accompanied by (de)solvation effects, affecting the access of water to the hydrophobic core. A well-ordered hydrophobic core thus has a similar effect as a high helix stability. Both parameters reduce the probability of helix uncoiling and displacement, thereby causing the structure to become more brittle.

When changing the **pulling geometry** while conserving the CC sequence, different rupture forces were observed. The mechanical chain separation pathways are different even though helix uncoiling precedes the rupture of the first hydrophobic contact in all cases. In the shear geometry, the local helix propensity at the points of force application appears to be crucial. This is combined with the probability of sliding, which is affected by the Asn-Asn lock. Its destabilization facilitates a higher relative displacement of the helices and thus increases the distance to the transition state. In the unzip geometry, hydrogen bonds and hydrophobic contacts are arranged differently with respect to the force vector. It is not fully clear how this affects the differences in the rupture forces measured due to the different loading rate dependence of the two systems. Nevertheless, when constraining one helix at the force application point, the rupture force increased and reached almost the level of the shear geometry.

Focusing on the A4/B4 reference sequence, it appears to be most thermodynamically and mechanically stable 4-heptad CC heterodimer that can be designed with the use of canonical amino acids. It combines a high helix stability with a tight hydrophobic core packing. It appears likely that the helix stability can be increased further with the insertion of additional *staples*; however, it remains an open question if the packing of the hydrophobic core can be improved. The most promising strategy to achieve this goal is the substitution of the entire hydrophobic core with fluorinated amino acids to fully harness the *fluorous effect*. Possible steric problems could be ruled out by modelling the structure with different fluorinated amino acids to optimize the steric space each amino acid occupies.

In summary, when designing a CC heterodimer with predefined thermodynamic and mechanical characteristics, the following interconnected parameters need to be considered: (1) amino acid hydrophobicity (2) optimized packing of these amino acids in the hydrophobic core, (3) amino acid helix propensity, (4) position of the Asn-Asn pair, (5) pulling geometry and (6) CC length. In combination, these parameters determine the chain separation mechanism and thus the mechanical stability of the CC. It will be interesting to investigate the effect of these parameters on the stability of higher order oligomers, which are predicted to possess a different chain separation mechanism (no relative displacement of the helices), which is accompanied by a higher mechanical stability [130].

9. FUTURE OUTLOOK

Having investigated a series of 4-heptad CC heterodimers with different modifications, a small library of CCs with different mechanical stabilities is now available, which can be used for applications. In the last part of this work, I will discuss how these CCs can be used as molecular force sensors or as dynamic mechanosensitive crosslinks in ECM-mimetic materials (in addition to the applications already given in Section 4.4.).

Coiled Coils as molecular force sensors (MFSs)

In recent years, many proteins involved in cellular mechanosensing and mechanotransduction have been identified; however, little is known about the forces required to activate these processes. There is a strong need for measuring these forces *in situ*. At the cell-ECM interface, integrins are key players transmitting forces between the cytoskeleton and the ECM. Thus, there is a strong interest to determine the mechanical stability of integrin-ligand interactions. Using SMFS, the rupture forces between α5β1 integrin and fibronectin were determined to be in the order of 39-100 pN in the loading rate range from 100-10000 pN s^{-1} [203, 204]. The SMFS setup is highly artificial, however, and other techniques such as traction force microscopy and molecular force sensors (MFSs) have been developed. MFSs are able to convert the force into a fluorescence signal so that the molecularly applied forces can be visualized and quantified (Figure 45) [205-207].
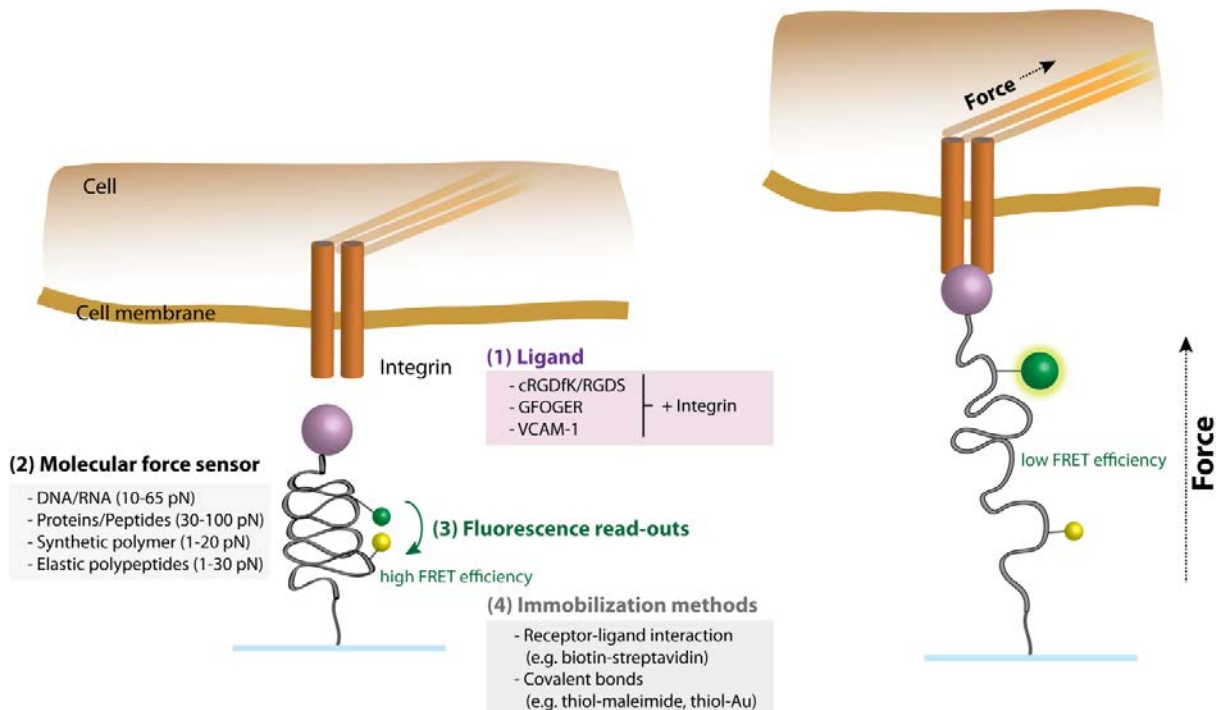
FIGURE 45 – General concept of a molecular force sensor (MFS). The MFS is equipped with an integrin ligand, allowing the cell to engage with the force sensor. Once the cell has bound to the MFSs, the MFSs experiences traction forces generated in the cytoskeleton. The applied force activates the sensor thereby generating an optical signal. In the example shown, the signal is a change in FRET (Förster resonance energy transfer) efficiency.

Just as DNA, the CCs can be tuned mechanically using sequence [208], length [209, 210] and pulling geometry [207] as parameters. Using DNA in different pulling geometries, Wang *et al* [211] demonstrated that integrins applied a force of at least ~40 pN during the initial stage of cell adhesion. When using DNA, the cell-binding ligand (an adhesive peptide, e.g. RGDS) needs to be coupled to the DNA-based MFSs [212]. As these ligands are frequently peptides, these ligands can simply be added to the CC during solid-phase peptide synthesis thereby greatly simplifying the process of MFSs preparation. More importantly, CCs have mechanical function in nature and are frequent building blocks of the ECM, whereas DNA is not usually present in the extracellular environment.

Coiled Coils as mechanosensitive crosslinks in 3D hydrogel-based materials

These newly created CC-based MFSs cannot only be used in 2D cell culture applications. They can also be used as mechanosensitive hydrogel crosslinks. Before such hydrogels can be utilized as smart ECM-inspired biomaterials, it needs to be understood how the molecular properties of the CC crosslinks determine the bulk mechanical behaviour of the hydrogel.

The CCs characterized in this work are currently being used to crosslink 4-arm PEG. To correlate single-molecule and bulk mechanics, each arm has the same molecular weight (10 kDa) as in the SMFS experiments (Figure 46). Maleimide-functionalized 4-arm PEG is independently functionalized with a peptide of the A- and B-series. When mixed, both peptides A and B interact to form the CC, hence inducing hydrogel formation. The resulting hydrogels are characterized with oscillatory shear **rheology** to obtain information about the bulk mechanical properties of the material (Figure 46).
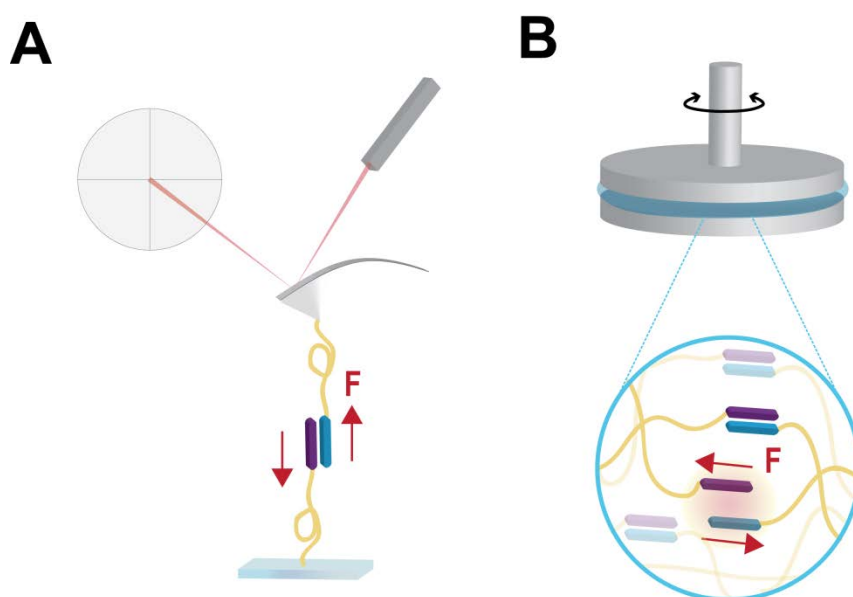
FIGURE 46 – Experimental design to compare the single-molecule properties of the Coiled Coil-crosslinks with the bulk properties of the PEG-based hydrogel. (A) Single-molecule force spectroscopy of Coiled Coils. (B) Oscillatory shear rheology of the Coiled Coil-crosslinked material.

Unpublished preliminary results obtained in collaboration with Alberto Sanz de León show that the CC does indeed determine the viscoelastic properties of the hydrogel. Equipping the CC with an optical readout will thus allow for observing the mechanical state of the CC during material deformation, first induced in the rheometer and later by cells growing in this mechanosensitive hydrogel.

10. BIBLIOGRAPHY

1.   Crick, F. H. C., (1953). The packing of α-helices: simple coiled-coils. Acta Crystallographica, **6**: 689-697.

2.   Pauling, L., and Corey, R. B., (1953). Compound Helical Configurations of Polypeptide Chains: Structure of Proteins of the α-Keratin Type. Nature, **171**: 59.

3.   Astbury, W. T., (1947). Croonian Lecture - On the structure of biological fibres and the problem of muscle. Proceedings of the Royal Society of London. Series B - Biological Sciences, **134**: 303-328.

4.   Lutolf, M. P., and Hubbell, J. A., (2005). Synthetic biomaterials as instructive extracellular microenvironments for morphogenesis in tissue engineering. Nature Biotechnology, **23**: 47.

5.   Rackham, O. J. L., Madera, M., Armstrong, C. T., Vincent, T. s. L., Woolfson, D. N., and Gough, J., (2010). The Evolution and Structure Prediction of Coiled Coils across All Genomes. Journal of Molecular Biology, **403**: 480-493.

6.   Lupas, A. N. and Bassler, J., (2017). Coiled Coils – A Model System for the 21st Century. Trends in Biochemical Sciences, **42**: 130-140.

7.   Moran, L. A., Horton, R. A., Scrimgeour, G., Perry, M., and Rawn, D., (2013), Principles of Biochemistry: Pearson New International Edition. 5th Edition ed.: Pearson Education Limited

8.   Woolfson, D. N., (2017). Coiled-Coil Design: Updated and Upgraded. Subcellular Biochemistry, **82**: 35-61.

9.   Su, J. Y., Hodges, R. S., and Kay, C. M., (1994). Effect of Chain Length on the Formation and Stability of Synthetic alpha-Helical Coiled Coils. Biochemistry, **33**: 15501-15510.

10.   Burkhard, P., Stetefeld, J., and Strelkov, S. V., (2001). Coiled coils: a highly versatile protein folding motif. Trends in Cell Biology, **11**: 82-88.

11.   Cohen, C. and Parry, D. A. D., (1986). Alpha-Helical coiled coils, a widespread motif in proteins. Trends in Biochemical Sciences, **11**: 245-248.

12.   Testa, O. D., Moutevelis, E., and Woolfson, D. N., (2009). CC+: a relational database of coiled-coil structures. Nucleic Acids Research, **37**: 315-322.

13.   Wood, C. W., Bruning, M., Ibarra, A. A., Bartlett, G. J., Thomson, A. R., Sessions, R. B., Brady, R. L., and Woolfson, D. N., (2014). CCBuilder: an interactive web-based tool for building, designing and assessing coiled-coil protein assemblies. Bioinformatics, **30**: 3029-3035.

14.   Vincent, T. L., Green, P. J., and Woolfson, D. N., (2013). LOGICOIL—multi-state prediction of coiled-coil oligomeric state. Bioinformatics, **29**: 69-76.

15.   Mason, J. M., Schmitz, M. A., Müller, K. M., and Arndt, K. M., (2006). Semirational design of Jun-Fos coiled coils with increased affinity: Universal implications for leucine zipper prediction and design. Proceedings of the National Academy of Sciences, **103**: 8989-8994.

16.   Walshaw, J. and Woolfson, D. N., (2001). Socket: a program for identifying and analysing coiled-coil motifs within protein structures. Journal of Molecular Biology, **307**: 1427-1450.

17.   ExPASy: SIB Bioinformatics Resource Portal. 2018; Available from: https://www.expasy.org/structural_bioinformatics.

18.   Lupas, A., Van Dyke, M., and Stock, J., (1991). Predicting coiled coils from protein sequences. Science, **252**: 1162-1164.

19.   Delorenzi, M. and Speed, T., (2002). An HMM model for coiled-coil domains and a comparison with PSSM-based predictions. Bioinformatics, **18**: 617-625.

20.   Zoete, V., Cuendet, M. A., Grosdidier, A., and Michielin, O., (2011). SwissParam: a fast force field generation tool for small organic molecules. Journal of Computational Chemistry, **32**: 2359-2368.

21.   Krogh, A., Larsson, B., von Heijne, G., and Sonnhammer, E. L., (2001). Predicting transmembrane protein topology with a hidden Markov model: application to complete genomes. Journal of Molecular Biology, **305**: 567-580.

22.   Chernyatina, A. A., Guzenko, D., and Strelkov, S. V., (2015). Intermediate filament structure: the bottom-up approach. Current Opinion on Cell Biology, **32**: 65-72.

23.   Macarthur, I. A. N., (1943). Structure of α-Keratin. Nature, **152**: 38.

24.   Lupas, A. N., Bassler, J., and Dunin-Horkawicz, S., (2017), The Structure and Topology of α-Helical Coiled Coils, in Fibrous Proteins: Structures and Mechanisms, D.A.D. Parry and J.M. Squire, Editors. Springer International Publishing. 95-129.

25.   Wu, K. C., Bryan, J. T., Morasso, M. I., Jang, S.-I., Lee, J.-H., Yang, J.-M., Marekov, L. N., Parry, D. A. D., and Steinert, P. M., (2000). Coiled-Coil Trigger Motifs in the 1B and 2B Rod Domain Segments Are Required for the Stability of Keratin Intermediate Filaments. Molecular Biology of the Cell, **11**: 3539-3558.

26.   Herrmann, H., Strelkov, S. V., Feja, B., Rogers, K. R., Brettel, M., Lustig, A., Haner, M., Parry, D. A., Steinert, P. M., Burkhard, P., and Aebi, U., (2000). The intermediate filament protein consensus motif of helix 2B: its atomic structure and contribution to assembly. Journal of Molecular Biology, **298**: 817-832.

27.   Squire, J. M., Paul, D. M., and Morris, E. P., (2017), Myosin and Actin Filaments in Muscle: Structures and Interactions, in Fibrous Proteins: Structures and Mechanisms, D.A.D. Parry and J.M. Squire, Editors. Springer International Publishing. 319-371.

28.   Schwaiger, I., Sattler, C., Hostetter, D. R., and Rief, M., (2002). The myosin coiled-coil is a truly elastic protein structure. Nature Materials, **1**: 232-235.

29.   Root, D. D., Yadavalli, V. K., Forbes, J. G., and Wang, K., (2006). Coiled-coil nanomechanics and uncoiling and unfolding of the superhelix and alpha-helices of myosin. Biophysical Journal, **90**: 2852-2866.

30.   Marx, A., Hoenger, A., and Mandelkow, E., (2009). Structures of Kinesin Motor Proteins. Cell motility and the cytoskeleton, **66**: 958-966.

31.   McLachlan, A. D. and Stewart, M., (1975). Tropomyosin coiled-coil interactions: Evidence for an unstaggered structure. Journal of Molecular Biology, **98**: 293-304.

32.   Collier, J. H., Rudra, J. S., Gasiorowski, J. Z., and Jung, J. P., (2010). Multi-Component Extracellular Matrices Based on Peptide Self-Assembly. Chemical Society Reviews, **39**: 3413-3424.

33.   Kammerer, R. A., (1997). Alpha-helical coiled-coil oligomerization domains in extracellular proteins. Journal of the International Society for Matrix Biology, **15**: 555-565.

34.   Kohler, S., Schmid, F., and Settanni, G., (2015). The Internal Dynamics of Fibrinogen and Its Implications for Coagulation and Adsorption. PLoS Computational Biology, **11**: e1004346.

35. Armony, G., Jacob, E., Moran, T., Levin, Y., Mehlman, T., Levy, Y., and Fass, D., (2016). Cross-linking reveals laminin coiled-coil architecture. Proceedings of the National Academy of Sciences, **113**: 13384-13389.

36. Guo, Y., Bozic, D., Malashkevich, V. N., Kammerer, R. A., Schulthess, T., and Engel, J., (1998). All-trans retinol, vitamin D and other hydrophobic compounds bind in the axial pore of the five-stranded coiled-coil domain of cartilage oligomeric matrix protein. The EMBO journal, **17**: 5265-5272.

37. Ozbek, S., Engel, J., and Stetefeld, J., (2002). Storage function of cartilage oligomeric matrix protein: the crystal structure of the coiled-coil domain in complex with vitamin D(3). EMBO Journal, **21**: 5960-5968.

38. Puklin-Faucher, E. and Sheetz, M. P., (2009). The mechanical integrin cycle. Journal of Cell Science, **122**: 179-186.

39. Iskratsch, T., Wolfenson, H., and Sheetz, M. P., (2014). Appreciating force and shape — the rise of mechanotransduction in cell biology. Nature Reviews Molecular Cell Biology, **15**: 825-833.

40. Lupas, A., (1996). Coiled coils: new structures and new functions. Trends in Biochemical Sciences, **21**: 375-382.

41. Woolfson, D. N., (2005). The Design of Coiled-Coil Structures and Assemblies. Advances in Protein Chemistry, **70**: 79-112.

42. Fletcher, J. M., Boyle, A. L., Bruning, M., Bartlett, G. J., Vincent, T. L., Zaccai, N. R., Armstrong, C. T., Bromley, E. H. C., Booth, P. J., Brady, R. L., Thomson, A. R., and Woolfson, D. N., (2012). A Basis Set of de Novo Coiled-Coil Peptide Oligomers for Rational Protein Design and Synthetic Biology. ACS Synthetic Biology, **1**: 240-250.

43. Fletcher, J. M., Bartlett, G. J., Boyle, A. L., Danon, J. J., Rush, L. E., Lupas, A. N., and Woolfson, D. N., (2017). N@a and N@d: Oligomer and Partner Specification by Asparagine in Coiled-Coil Interfaces. ACS Chemical Biology, **12**: 528-538.

44. Thomas, F., Boyle, A. L., Burton, A. J., and Woolfson, D. N., (2013). A set of de novo designed parallel heterodimeric coiled coils with quantified dissociation constants in the micromolar to sub-nanomolar regime. Journal of the American Chemical Society, **135**: 5161-5166.

45. Litowski, J. R. and Hodges, R. S., (2002). Designing heterodimeric two-stranded alpha-helical coiled-coils. Effects of hydrophobicity and alpha-helical propensity on protein folding, stability, and specificity. Journal of Biological Chemistry, **277**: 37272-37279.

46. Wagschal, K., Tripet, B., Lavigne, P., Mant, C., and Hodges, R. S., (1999). The role of position a in determining the stability and oligomerization state of alpha-helical coiled coils: 20 amino acid stability coefficients in the hydrophobic core of proteins. Protein Science, **8**: 2312-2329.

47. Potapov, V., Kaplan, J. B., and Keating, A. E., (2015). Data-driven prediction and design of bZIP coiled-coil interactions. PLoS Computational Biology, **11**: e1004046.

48. Meier, M., Stetefeld, J., and Burkhard, P., (2010). The many types of interhelical ionic interactions in coiled coils - an overview. Journal of Structural Biology, **170**: 192-201.

49. Surkont, J. and Pereira-Leal, J. B., (2015). Evolutionary Patterns in Coiled-Coils. Genome Biology and Evolution, **7**: 545-556.

50.   Litowski, J. R. and Hodges, R. S., (**2001**). Designing heterodimeric two-stranded α-helical coiled-coils: the effect of chain length on protein folding, stability and specificity. The Journal of Peptide Research, **58**: 477-492.

51.   O'Shea, E. K., Klemm, J. D., Kim, P. S., and Alber, T., (1991). X-ray structure of the GCN4 leucine zipper, a two-stranded, parallel coiled coil. Science, **254**: 539-544.

52.   Zhu, B. Y., Zhou, N. E., Kay, C. M., and Hodges, R. S., (1993). Packing and hydrophobicity effects on protein folding and stability: effects of beta-branched amino acids, valine and isoleucine, on the formation and stability of two-stranded alpha-helical coiled coils/leucine zippers. Protein Science, **2**: 383-394.

53.   Jelesarov I, B. H., (1996). Thermodynamic characterization of the coupled folding and association of heterodimeric coiled coils (leucine zipper). Journal of Molecular Biology, **263**: 344-358.

54.   Harbury, P. B., Zhang, T., Kim, P. S., and Alber, T., (1993). A switch between two-, three-, and four-stranded coiled coils in GCN4 leucine zipper mutants. Science, **262**: 1401-1407.

55.   Gonzalez, L. J., Brown, R. A., Richardson, D., and Alber, T., (1996). Crystal structures of a single coiled-coil peptide in two oligomeric states reveal the basis for structural polymorphism. Nature Structural & Molecular Biology, **3**: 1002-1010.

56.   Tripet, B., Wagschal, K., Lavigne, P., Mant, C. T., and Hodges, R. S., (2000). Effects of side-chain characteristics on stability and oligomerization state of a de novo-designed model coiled-coil: 20 amino acid substitutions in position "d". Journal of Molecular Biology, **300**: 377-402.

57.   Thomas, F., Niitsu, A., Oregioni, A., Bartlett, G. J., and Woolfson, D. N., (2017). Conformational Dynamics of Asparagine at Coiled-Coil Interfaces. Biochemistry, **56**: 6544-6554.

58.   Oakley, M. G. and Kim, P. S., (1998). A Buried Polar Interaction Can Direct the Relative Orientation of Helices in a Coiled Coil. Biochemistry, **37**: 12603-12610.

59.   Zhou, N. E., Kay, C. M., and Hodges, R. S., (1994). The Role of Interhelical Ionic Interactions in Controlling Protein Folding and Stability: De Novo Designed Synthetic Two-stranded α-Helical Coiled-Coils. Journal of Molecular Biology, **237**: 500-512.

60.   Zhuravlev, P. I., Hinczewski, M., Chakrabarti, S., Marqusee, S., and Thirumalai, D., (2016). Force-dependent switch in protein unfolding pathways and transition-state movements. Proceedings of the National Academy of Sciences, **113**: E715-E724.

61.   Baker, E. G., Bartlett, G. J., Crump, M. P., Sessions, R. B., Linden, N., Faul, C. F., and Woolfson, D. N., (2015). Local and macroscopic electrostatic interactions in single alpha-helices. Nature Chemical Biology, **11**: 221-228.

62.   Meuzelaar, H., Vreede, J., and Woutersen, S., (2016). Influence of Glu/Arg, Asp/Arg, and Glu/Lys Salt Bridges on alpha-Helical Stability and Folding Kinetics. Biophysical Journal, **110**: 2328-2341.

63.   Kammerer, R. A., Jaravine, V. A., Frank, S., Schulthess, T., Landwehr, R., Lustig, A., Garcia-Echeverria, C., Alexandrescu, A. T., Engel, J., and Steinmetz, M. O., (2001). An intrahelical salt bridge within the trigger site stabilizes the GCN4 leucine zipper. Journal of Biological Chemistry, **276**: 13685-13688.

64.   Matousek, W. M., Ciani, B., Fitch, C. A., Garcia-Moreno, B., Kammerer, R. A., and Alexandrescu, A. T., (2007). Electrostatic contributions to the stability of the GCN4 leucine zipper structure. Journal of Molecular Biology, **374**: 206-219.

65. Aronsson, C., Danmark, S., Zhou, F., Oberg, P., Enander, K., Su, H., and Aili, D., (2015). Self-sorting heterodimeric coiled coil peptides with defined and tuneable self-assembly properties. Scientific Reports, **5**: 14063.

66. Dånmark, S., Aronsson, C., and Aili, D., (2016). Tailoring Supramolecular Peptide–Poly(ethylene glycol) Hydrogels by Coiled Coil Self-Assembly and Self-Sorting. Biomacromolecules, **17**: 2260-2267.

67. Gradišar, H. and Jerala, R., (2011). De novo design of orthogonal peptide pairs forming parallel coiled-coil heterodimers. Journal of Peptide Science, **17**: 100-106.

68. Lapenta, F., Aupic, J., Strmsek, Z., and Jerala, R., (2018). Coiled coil protein origami: from modular design principles towards biotechnological applications. Chemical Society Reviews, **47**: 3530-3542.

69. Bromley, E. H. C., Sessions, R. B., Thomson, A. R., and Woolfson, D. N., (2009). Designed α-Helical Tectons for Constructing Multicomponent Synthetic Biological Systems. Journal of the American Chemical Society, **131**: 928-930.

70. Crooks, R. O., Lathbridge, A., Panek, A. S., and Mason, J. M., (2017). Computational Prediction and Design for Creating Iteratively Larger Heterospecific Coiled Coil Sets. Biochemistry, **56**: 1573-1584.

71. Jelesarov, I., Durr, E., Thomas, R. M., and Bosshard, H. R., (1998). Salt effects on hydrophobic interaction and charge screening in the folding of a negatively charged peptide to a coiled coil (leucine zipper). Biochemistry, **37**: 7539-7550.

72. Lizatovic, R., Aurelius, O., Stenstrom, O., Drakenberg, T., Akke, M., Logan, D. T., and Andre, I., (2016). A De Novo Designed Coiled-Coil Peptide with a Reversible pH-Induced Oligomerization Switch. Structure, **24**: 946-955.

73. Kaplan, A. R., Brady, M. R., Maciejewski, M. W., Kammerer, R. A., and Alexandrescu, A. T., (2017). Nuclear Magnetic Resonance Structures of GCN4p Are Largely Conserved When Ion Pairs Are Disrupted at Acidic pH but Show a Relaxation of the Coiled Coil Superhelix. Biochemistry, **56**: 1604-1619.

74. Pagel, K., Wagner, S. C., Rezaei Araghi, R., von Berlepsch, H., Bottcher, C., and Koksch, B., (2008). Intramolecular charge interactions as a tool to control the coiled-coil-to-amyloid transformation. Chemistry, **14**: 11442-11451.

75. Wolny, M., Batchelor, M., Bartlett, G. J., Baker, E. G., Kurzawa, M., Knight, P. J., Dougan, L., Woolfson, D. N., Paci, E., and Peckham, M., (2017). Characterization of long and stable de novo single alpha-helix domains provides novel insight into their stability. Scientific Reports, **7**: 44341.

76. Pace, C. N. and Scholtz, J. M., (1998). A helix propensity scale based on experimental studies of peptides and proteins. Biophysical Journal, **75**: 422-427.

77. Dahiyat, B. I., Gordon, D. B., and Mayo, S. L., (1997). Automated design of the surface positions of protein helices. Protein Science, **6**: 1333-1337.

78. Lacroix, E., Viguera, A. R., and Serrano, L., (1998). Elucidating the folding problem of α-helices: local motifs, long-range electrostatics, ionic-strength dependence and prediction of NMR parameters. Journal of Molecular Biology, **284**: 173-191.

79. Drobnak, I., Gradisar, H., Ljubetic, A., Merljak, E., and Jerala, R., (2017). Modulation of Coiled-Coil Dimer Stability through Surface Residues while Preserving Pairing Specificity. Journal of the American Chemical Society, **139**: 8229-8236.

80.   Leaver-Fay, A., Tyka, M., Lewis, S. M., Lange, O. F., Thompson, J., Jacak, R., Kaufman, K. W., Renfrew, P. D., Smith, C. A., Sheffler, W., Davis, I. W., Cooper, S., Treuille, A., Mandell, D. J., Richter, F., Ban, Y.-E. A., Fleishman, S. J., Corn, J. E., Kim, D. E., Lyskov, S., Berrondo, M., Mentzer, S., Popović, Z., Havranek, J. J., Karanicolas, J., Das, R., Meiler, J., Kortemme, T., Gray, J. J., Kuhlman, B., Baker, D., and Bradley, P., (2011), Chapter nineteen - Rosetta3: An Object-Oriented Software Suite for the Simulation and Design of Macromolecules, in Methods in Enzymology, M.L. Johnson and L. Brand, Editors. Academic Press. 545-574.

81.   Hartmann, M. D., Ridderbusch, O., Zeth, K., Albrecht, R., Testa, O., Woolfson, D. N., Sauer, G., Dunin-Horkawicz, S., Lupas, A. N., and Alvarez, B. H., (2009). A coiled-coil motif that sequesters ions to the hydrophobic core. Proceedings of the National Academy of Sciences, **106**: 16950-16955.

82.   Walshaw, J. and Woolfson, D. N., (2003). Extended knobs-into-holes packing in classical and complex coiled-coil assemblies. Journal of Structural Biology, **144**: 349-361.

83.   Thomas, F., Dawson, W. M., Lang, E. J. M., Burton, A. J., Bartlett, G. J., Rhys, G. G., Mulholland, A. J., and Woolfson, D. N., (2018). De Novo-Designed α-Helical Barrels as Receptors for Small Molecules. ACS Synthetic Biology, **7**: 1808–1816.

84.   Burton, A. J., Thomson, A. R., Dawson, W. M., Brady, R. L., and Woolfson, D. N., (2016). Installing hydrolytic activity into a completely de novo protein framework. Nature Chemistry, **8**: 837-844.

85.   Thompson, K. E., Bashor, C. J., Lim, W. A., and Keating, A. E., (2012). SYNZIP Protein Interaction Toolbox: in Vitro and in Vivo Specifications of Heterospecific Coiled-Coil Interaction Domains. ACS Synthetic Biology, **1**: 118-129.

86.   Negron, C. and Keating, A. E., (2014). A Set of Computationally Designed Orthogonal Antiparallel Homodimers that Expands the Synthetic Coiled-Coil Toolkit. Journal of the American Chemical Society, **136**: 16544-16556.

87.   Gradisar, H., Bozic, S., Doles, T., Vengust, D., Hafner-Bratkovic, I., Mertelj, A., Webb, B., Sali, A., Klavzar, S., and Jerala, R., (2013). Design of a single-chain polypeptide tetrahedron assembled from coiled-coil segments. Nature Chemical Biology, **9**: 362-366.

88.   Walensky, L. D. and Bird, G. H., (2014). Hydrocarbon-stapled peptides: principles, practice, and progress. Journal of Medicinal Chemistry, **57**: 6275-6288.

89.   Salwiczek, M., Samsonov, S., Vag, T., Nyakatura, E., Fleige, E., Numata, J., Cölfen, H., Pisabarro, M. T., and Koksch, B., (2009). Position-Dependent Effects of Fluorinated Amino Acids on the Hydrophobic Core Formation of a Heterodimeric Coiled Coil. Chemistry: A European Journal, **15**: 7628-7636.

90.   Salwiczek, M., Nyakatura, E. K., Gerling, U. I., Ye, S., and Koksch, B., (2012). Fluorinated amino acids: compatibility with native protein structures and effects on protein-protein interactions. Chemical Society Reviews, **41**: 2135-2171.

91.   Schnarr, N. A. and Kennan, A. J., (2002). Peptide Tic-Tac-Toe: Heterotrimeric Coiled-Coil Specificity from Steric Matching of Multiple Hydrophobic Side Chains. Journal of the American Chemical Society, **124**: 9779-9783.

92.   Chen, Y., Radford, S. E., and Brockwell, D. J., (2015). Force-induced remodelling of proteins and their complexes. Current Opinion in Structural Biology, **30**: 89-99.

93.   Paci, E. and Karplus, M., (2000). Unfolding proteins by external forces and temperature: The importance of topology and energetics. Proceedings of the National Academy of Sciences, **97** 6521-6526.

94. Ainavarapu, S. R., Brujic, J., Huang, H. H., Wiita, A. P., Lu, H., Li, L., Walther, K. A., Carrion-Vazquez, M., Li, H., and Fernandez, J. M., (2007). Contour length and refolding rate of a small protein controlled by engineered disulfide bonds. Biophysical Journal, **92**: 225-233.

95. Hoffmann, T., Tych, K. M., Hughes, M. L., Brockwell, D. J., and Dougan, L., (2013). Towards design principles for determining the mechanical stability of proteins. Physical Chemistry Chemical Physics, **15**: 15767-15780.

96. Dietz, H., Berkemeier, F., Bertz, M., and Rief, M., (2006). Anisotropic deformation response of single protein molecules. Proceedings of the National Academy of Sciences, **103**: 12724-12728.

97. Dietz, H. and Rief, M., (2006). Protein structure by mechanical triangulation. Proceedings of the National Academy of Sciences, **103**: 1244-1247.

98. Bornschlogl, T. and Rief, M., (2008). Single-molecule dynamics of mechanical coiled-coil unzipping. Langmuir, **24**: 1338-1342.

99. Brockwell, D. J., Paci, E., Zinober, R. C., Beddard, G. S., Olmsted, P. D., Smith, D. A., Perham, R. N., and Radford, S. E., (2003). Pulling geometry defines the mechanical resistance of a beta-sheet protein. Nature Structural Biology, **10**: 731-737.

100. Yao, M., Qiu, W., Liu, R., Efremov, A. K., Cong, P., Seddiki, R., Payre, M., Lim, C. T., Ladoux, B., Mege, R. M., and Yan, J., (2014). Force-dependent conformational switch of alpha-catenin controls vinculin binding. Nature Communications, **5**: 4525.

101. Rief, M., Pascual, J., Saraste, M., and Gaub, H. E., (1999). Single molecule force spectroscopy of spectrin repeats: low unfolding forces in helix bundles. Journal of Molecular Biology, **286**: 553-561.

102. Brown, A. E., Litvinov, R. I., Discher, D. E., and Weisel, J. W., (2007). Forced unfolding of coiled-coils in fibrinogen by single-molecule AFM. Biophysical Journal, **92**: L39-41.

103. Dietz, H., Bornschlögl, T., Heym, R., König, F., and Rief, M., (2007). Programming protein self assembly with coiled coils. New Journal of Physics, **9**: 424-424.

104. Junker, J. P., Ziegler, F., and Rief, M., (2009). Ligand-dependent equilibrium fluctuations of single calmodulin molecules. Science, **323**: 633-637.

105. Gebhardt, J. C. M., Bornschlögl, T., and Rief, M., (2010). Full distance-resolved folding energy landscape of one single protein molecule. Proceedings of the National Academy of Sciences, **107**: 2013-2018.

106. Bornschlögl, T., Woehlke, G., and Rief, M., (2009). Single molecule mechanics of the kinesin neck. Proceedings of the National Academy of Sciences, **106**: 6992-6997.

107. del Rio, A., Perez-Jimenez, R., Liu, R., Roca-Cusachs, P., Fernandez, J. M., and Sheetz, M. P., (2009). Stretching single talin rod molecules activates vinculin binding. Science, **323**: 638-641.

108. Goktas, M., Luo, C., Sullan, R. M. A., Bergues-Pupo, A. E., Lipowsky, R., Vila Verde, A., and Blank, K., (2018). Molecular Mechanics of Coiled Coils Loaded in the Shear Geometry. Chemical Science, **9**: 4610-4621

109. Falkovich, S. G., Neelov, I. M., and Darinskii, A. A., (2010). Mechanism of shear deformation of a coiled myosin coil: Computer simulation. Polymer Science, Series A: Polymer Physics, **52**: 662-670.

110.   Ackbarow, T. and Buehler, M. J., (2007). Superelasticity, energy dissipation and strain hardening of vimentin coiled-coil intermediate filaments: atomistic and continuum studies. Journal of Materials Science, **42**: 8771-8787.

111.   Hamed, E. and Keten, S., (2014). Hierarchical cascades of instability govern the mechanics of coiled coils: helix unfolding precedes coil unzipping. Biophysical Journal, **107**: 477-484.

112.   Strauss, H. M. and Keller, S., (2008), Pharmacological Interference with Protein-Protein Interactions Mediated by Coiled-Coil Motifs, in Protein-Protein Interactions as New Drug Targets, E. Klussmann and J. Scott, Editors. Springer 461-482.

113.   Robson Marsden, H., Elbers, N. A., Bomans, P. H., Sommerdijk, N. A., and Kros, A., (2009). A reduced SNARE model for membrane fusion. Angewandte Chemie International Edition in English, **48**: 2330-2333.

114.   Ljubetic, A., Lapenta, F., Gradisar, H., Drobnak, I., Aupic, J., Strmsek, Z., Lainscek, D., Hafner-Bratkovic, I., Majerle, A., Krivec, N., Bencina, M., Pisanski, T., Velickovic, T. C., Round, A., Carazo, J. M., Melero, R., and Jerala, R., (2017). Design of coiled-coil protein-origami cages that self-assemble in vitro and in vivo. Nature Biotechnology, **35**: 1094–1101.

115.   Jing, P., Rudra, J. S., Herr, A. B., and Collier, J. H., (2008). Self-Assembling Peptide-Polymer Hydrogels Designed From the Coiled Coil Region of Fibrin. Biomacromolecules, **9**: 2438-2446.

116.   Chao, H., Bautista, D. L., Litowski, J. R., Irvin, R. T., and Hodges, R. S., (1998). Use of a heterodimeric coiled-coil system for biosensor application and affinity purification. Journal of Chromatography B: Biomedical Sciences and Applications, **715**: 307-329.

117.   Zheng, T., Bulacu, M., Daudey, G., Versluis, F., Voskuhl, J., Martelli, G., Raap, J., Sevink, G. J. A., Kros, A., and Boyle, A. L., (2016). A non-zipper-like tetrameric coiled coil promotes membrane fusion. RSC Advances, **6**: 7990-7998

118.   Hong, F., Zhang, F., Liu, Y., and Yan, H., (2017). DNA Origami: Scaffolds for Creating Higher Order Structures. Chemical Reviews, **117**: 12584-12640.

119.   Huang, P.-S., Boyken, S. E., and Baker, D., (2016). The coming of age of de novo protein design. Nature, **537**: 320-327.

120.   Kobayashi, N. and Arai, R., (2017). Design and construction of self-assembling supramolecular protein complexes using artificial and fusion proteins as nanoscale building blocks. Current Opinion in Biotechnology, **46**: 57-65.

121.   Boyle, A. L., Bromley, E. H. C., Bartlett, G. J., Sessions, R. B., Sharp, T. H., Williams, C. L., Curmi, P. M. G., Forde, N. R., Linke, H., and Woolfson, D. N., (2012). Squaring the Circle in Peptide Assembly: From Fibers to Discrete Nanostructures by de Novo Design. Journal of the American Chemical Society, **134**: 15457-15467.

122.   Banwell, E. F., Abelardo, E. S., Adams, D. J., Birchall, M. A., Corrigan, A., Donald, A. M., Kirkland, M., Serpell, L. C., Butler, M. F., and Woolfson, D. N., (2009). Rational design and application of responsive alpha-helical peptide hydrogels. Nature Materials, **8**: 596-600.

123.   Deacon, S. P., Apostolovic, B., Carbajo, R. J., Schott, A. K., Beck, K., Vicent, M. J., Pineda-Lucena, A., Klok, H. A., and Duncan, R., (2011). Polymer coiled-coil conjugates: potential for development as a new class of therapeutic "molecular switch". Biomacromolecules, **12**: 19-27.

124.   Altunbas, A. and Pochan, D. J., (2012). Peptide-based and polypeptide-based hydrogels for drug delivery and tissue engineering. Topics in Current Chemistry, **310**: 135-167.

125.   Cai, P., Hu, B., Leow, W. R., Wang, X., Loh, X. J., Wu, Y.-L., and Chen, X.). Biomechano-Interactive Materials and Interfaces. Advanced Materials, **30**: e1800572.

126.   Krylov, D., Mikhailenko, I., and Vinson, C., (1994). A thermodynamic scale for leucine zipper stability and dimerization specificity: e and g interhelical interactions. EMBO Journal, **13**: 2849-2861.

127.   Monera, O. D., Sereda, T. J., Zhou, N. E., Kay, C. M., and Hodges, R. S., (1995). Relationship of sidechain hydrophobicity and alpha-helical propensity on the stability of the single-stranded amphipathic alpha-helix. Journal of Peptide Science, **1**: 319-329.

128.   Thompson, K. S., Vinson, C. R., and Freire, E., (1993). Thermodynamic characterization of the structural stability of the coiled-coil region of the bZIP transcription factor GCN4. Biochemistry, **32**: 5491-5496.

129.   Bornschlogl, T. and Rief, M., (2006). Single molecule unzipping of coiled coils: sequence resolved stability profiles. Physical Review Letters, **96**: 118102.

130.   Bergues-Pupo, A. E., Blank, K., Lipowsky, R., and Vila Verde, A., (2018). Trimeric coiled coils expand the range of strength, toughness and dynamics of coiled coil motifs under shear. Physical Chemistry Chemical Physics, **20**: 29105-29115.

131.   Yu, C. H., Law, J. B., Suryana, M., Low, H. Y., and Sheetz, M. P., (2011). Early integrin binding to Arg-Gly-Asp peptide activates actin polymerization and contractile movement that stimulates outward translocation. Proceedings of the National Academy of Sciences, **108**: 20585-20590.

132.   Gasteiger, E., Hoogland, C., Gattiker, A., Duvaud, S., Wilkins, M. R., Appel, R. D., and Bairoch, A., (2005), Protein Identification and Analysis Tools on the ExPASy Server. The Proteomics Protocols Handbook, Humana Press. Humana Press.

133.   Purdie, N., (1996). Circular Dichroism and the Conformational Analysis of Biomolecules. Journal of the American Chemical Society, **118**: 12871-12871.

134.   Kelly, S. M., Jess, T. J., and Price, N. C., (2005). How to study proteins by circular dichroism. Biochimica et Biophysica Acta, **1751**: 119-139.

135.   Greenfield, N. J., (2006). Using circular dichroism collected as a function of temperature to determine the thermodynamics of protein unfolding and binding interactions. Nature Protocols, **1**: 2527-2535.

136.   Mergny, J.-L. and Lacroix, L., (2001), UV Melting of G-Quadruplexes, in Current Protocols in Nucleic Acid Chemistry. John Wiley & Sons, Inc. 17.11.11-17.11.15.

137.   Neuman, K. C. and Nagy, A., (2008). Single-molecule force spectroscopy: optical tweezers, magnetic tweezers and atomic force microscopy. Nature Methods, **5**: 491-505.

138.   Binnig, G., Quate, C. F., and Gerber, C., (1986). Atomic force microscope. Physical Review Letters, **56**: 930-933.

139.   Hutter, J. L. and Bechhoefer, J., (1993). Calibration of atomic-force microscope tips. Review of Scientific Instruments, **64**: 1868-1873.

140.   JPK, A practical guide to AFM force spectroscopy and data analysis: https://www.jpk.com/app-technotes/applications_notes-single-molecule-force-spectroscopy.

141.   Noy, A., (2011). Force spectroscopy 101: how to design, perform, and analyze an AFM-based single molecule force spectroscopy experiment. Current Opinion in Chemical Biology, **15**: 710-718.

142. Oesterhelt, F., Rief, M., and Gaub, H. E., (1999). Single molecule force spectroscopy by AFM indicates helical structure of poly(ethylene-glycol) in water. New Journal of Physics, **1**: 6.

143. Giannotti, M. I. and Vancso, G. J., (2007). Interrogation of single synthetic polymer chains and polysaccharides by AFM-based force spectroscopy. Chemphyschem, **8**: 2290-2307.

144. Evans, E. and Ritchie, K., (1997). Dynamic strength of molecular adhesion bonds. Biophys. J., **72**: 1541-1555.

145. Hane, F. T., Attwood, S. J., and Leonenko, Z., (2014). Comparison of three competing dynamic force spectroscopy models to study binding forces of amyloid-beta (1-42). Soft Matter, **10**: 1924-1930.

146. Dudko, O. K., Hummer, G., and Szabo, A., (2008). Theory, analysis, and interpretation of single-molecule force spectroscopy experiments. Proceedings of the National Academy of Sciences, **105**: 15755-15760.

147. Friddle, R. W., Noy, A., and De Yoreo, J. J., (2012). Interpreting the widespread nonlinear force spectra of intermolecular bonds. Proceedings of the National Academy of Sciences, **109**: 13573-13578.

148. Schlierf, M. and Rief, M., (2005). Temperature Softening of a Protein in Single-molecule Experiments. Journal of Molecular Biology, **354**: 497-503.

149. Akmal, A. and Muñoz, V., (2004). The nature of the free energy barriers to two-state folding. Proteins: Structure, Function, Bioinformatics, **57**: 142-152.

150. Gloss, L. M. and Matthews, C. R., (1998). The barriers in the bimolecular and unimolecular folding reactions of the dimeric core domain of Escherichia coli Trp repressor are dominated by enthalpic contributions. Biochemistry, **37**: 16000-16010.

151. Milstein, J. N. and Meiners, J.-C., (2013), Worm-Like Chain (WLC) Model, in Encyclopedia of Biophysics, G.C.K. Roberts, Editor. Springer 2757-2760.

152. Zimmermann, J. L., Nicolaus, T., Neuert, G., and Blank, K., (2010). Thiol-based, site-specific and covalent immobilization of biomolecules for single-molecule experiments. Nature Protocols, **5**: 975-985.

153. Doig, A. J. and Baldwin, R. L., (1995). N- and C-capping preferences for all 20 amino acids in alpha-helical peptides. Protein Science, **4**: 1325-1336.

154. Koulechova, D. A., Tripp, K. W., Horner, G., and Marqusee, S., (2015). When the Scaffold Cannot Be Ignored: The Role of the Hydrophobic Core in Ligand Binding and Specificity. Journal of Molecular Biology, **427**: 3316-3326.

155. Bu, T., Wang, H. C., and Li, H., (2012). Single molecule force spectroscopy reveals critical roles of hydrophobic core packing in determining the mechanical stability of protein GB1. Langmuir, **28**: 12319-12325.

156. Tych, K. M., Batchelor, M., Hoffmann, T., Wilson, M. C., Hughes, M. L., Paci, E., Brockwell, D. J., and Dougan, L., (2016). Differential Effects of Hydrophobic Core Packing Residues for Thermodynamic and Mechanical Stability of a Hyperthermophilic Protein. Langmuir, **32**: 7392-7402.

157. Tych, K. M., Batchelor, M., Hoffmann, T., Wilson, M. C., Paci, E., Brockwell, D. J., and Dougan, L., (2016). Tuning protein mechanics through an ionic cluster graft from an extremophilic protein. Soft Matter, **12**: 2688-2699.

158. Chakrabartty, A., Kortemme, T., and Baldwin, R. L., (1994). Helix propensities of the amino acids measured in alanine-based peptides without helix-stabilizing side-chain interactions. Protein Science, **3**: 843-852.

159. Lin, J. C., Barua, B., and Andersen, N. H., (2004). The Helical Alanine Controversy: An (Ala)6 Insertion Dramatically Increases Helicity. Journal of the American Chemical Society, **126**: 13679–13684.

160. Scheraga, H. A., Vila, J. A., and Ripoll, D. R., (2002). Helix-coil transitions re-visited. Biophysical Chemistry, **101-102**: 255-265.

161. Sadler, D. P., Petrik, E., Taniguchi, Y., Pullen, J. R., Kawakami, M., Radford, S. E., and Brockwell, D. J., (2009). Identification of a mechanical rheostat in the hydrophobic core of protein L. Journal of Molecular Biology, **393**: 237-248.

162. Dill, K. A. and Bromberg, S., (2003), Molecular driving forces: Statistical Thermodynamics in Chemistry and Biology. Garland Science.

163. Collins, K. D., (1997). Charge density-dependent strength of hydration and biological structure. Biophysical Journal, **72**: 65-76.

164. Zheng, P., Cao, Y., Bu, T., Straus, S. K., and Li, H., (2011). Single Molecule Force Spectroscopy Reveals that Electrostatic Interactions Affect the Mechanical Stability of Proteins. Biophysical Journal, **100**: 1534-1541.

165. Pandya, M. J., Spooner, G. M., Sunde, M., Thorpe, J. R., Rodger, A., and Woolfson, D. N., (2000). Sticky-End Assembly of a Designed Peptide Fiber Provides Insight into Protein Fibrillogenesis. Biochemistry, **39**: 8728-8734.

166. Carrion-Vazquez, M., Oberhauser, A. F., Fowler, S. B., Marszalek, P. E., Broedel, S. E., Clarke, J., and Fernandez, J. M., (1999). Mechanical and chemical unfolding of a single protein: A comparison. Proceedings of the National Academy of Sciences, **96**: 3694-3699.

167. Carrion-Vazquez, M., Oberhauser, A. F., Fisher, T. E., Marszalek, P. E., Li, H., and Fernandez, J. M., (2000). Mechanical design of proteins studied by single-molecule force spectroscopy and protein engineering. Progress in Biophysics & Molecular Biology, **74**: 63-91.

168. Bertz, M. and Rief, M., (2009). Ligand binding mechanics of maltose binding protein. Journal of Molecular Biology, **393**: 1097-1105.

169. Schafmeister, C. E., Po, J., and Verdine, G. L., (2000). An All-Hydrocarbon Cross-Linking System for Enhancing the Helicity and Metabolic Stability of Peptides. Journal of the American Chemical Society, **122**: 5891-5892.

170. Madani, F., Lindberg, S., Langel, U., Futaki, S., and Graslund, A., (2011). Mechanisms of cellular uptake of cell-penetrating peptides. Journal of Biophysics: 414729.

171. Philippe, G., Huang, Y. H., Cheneval, O., Lawrence, N., Zhang, Z., Fairlie, D. P., Craik, D. J., de Araujo, A. D., and Henriques, S. T., (2016). Development of cell-penetrating peptide-based drug leads to inhibit MDMX:p53 and MDM2:p53 interactions. Biopolymers, **106**: 853-863.

172. de Araujo, A. D., Lim, J., Good, A. C., Skerlj, R. T., and Fairlie, D. P., (2017). Electrophilic Helical Peptides That Bond Covalently, Irreversibly, and Selectively in a Protein-Protein Interaction Site. ACS Medicinal Chemistry Letters, **8**: 22-26.

173. Dinh, T. T., Kim, D. H., Luong, H. X., Lee, B. J., and Kim, Y. W., (2015). Antimicrobial activity of doubly-stapled alanine/lysine-based peptides. Bioorganic & Medicinal Chemistry Letters, **25**: 4016-4019.

174. Blackwell, H. and Grubbs, R., (1998). Highly Efficient Synthesis of Covalently Cross-Linked Peptide Helices by Ring-Closing Metathesis. Angewandte Chemie International Edition in English, **37**: 3281-3284.

175.   Ali, A. M., Forbes, M. W., and Woolley, G. A., (2015). Optimizing the Photocontrol of bZIP Coiled Coils with Azobenzene Crosslinkers: Role of the Crosslinking Site. Chembiochem, **16**: 1757-1763.

176.   Mendive-Tapia, L., Preciado, S., Garcia, J., Ramon, R., Kielland, N., Albericio, F., and Lavilla, R., (2015). New peptide architectures through C-H activation stapling between tryptophan-phenylalanine/tyrosine residues. Nature Communications, **6**: 7160.

177.   Wang, Y. and Chou, H.-C. D., (2015). A Thiol–Ene Coupling Approach to Native Peptide Stapling and Macrocyclization. Angewandte Chemie International Edition in English, **127**: 11081-11084.

178.   Wang, Y., Bruno, B. J., Cheatham, T. E., Lim, C. S., Cornillie, S., Nogieira, J. M., and Chou, D. H.-C., (2017). Application of Thiol–yne/Thiol–ene Reactions for Peptide and Protein Macrocyclizations. Chemistry: A European Journal, **23**: 1 – 7.

179.   Jackson, D. Y., King, D. S., Chmielewski, J., Singh, S., and Schultz, P. G., (1991). General approach to the synthesis of short alpha-helical peptides. Journal of the American Chemical Society, **113**: 9391–9392.

180.   Houston Jr., M. E., Gannon, C. L., Kay, C. M., and Hodges, R. S., (1995). Lactam bridge stabilization of α-helical peptides: Ring size, orientation and positional effects Journal of Peptide Science, **1**: 274-282.

181.   Harrison, R. S., Shepherd, N. E., Hoang, H. N., Ruiz-Gómez, G., Hill, T. A., Driver, R. W., Desai, V. S., Young, P. R., Abbenante, G., and Fairlie, D. P., (2010). Downsizing human, bacterial, and viral proteins to short water-stable alpha helices that maintain biological potency. Proceedings of the National Academy of Sciences, **107**: 11686-11691.

182.   de Araujo, A. D., Hoang, H. N., Kok, W. M., Diness, F., Gupta, P., Hill, T. A., Driver, R. W., Price, D. A., Liras, S., and Fairlie, D. P., (2014). Comparative alpha-helicity of cyclic pentapeptides in water. Angewandte Chemie International Edition in English, **53**: 6965-6969.

183.   Houston, M. E., Jr., Wallace, A., Bianchi, E., Pessi, A., and Hodges, R. S., (1996). Use of a conformationally restricted secondary structural element to display peptide libraries: a two-stranded alpha-helical coiled-coil stabilized by lactam bridges. Journal of Molecular Biology, **262**: 270-282.

184.   Tunn, I., de Léon, A. S., Blank, K. G., and Harrington, M. J., (2018). Tuning coiled coil stability with histidine-metal coordination. Nanoscale, **10**: 22725-22729.

185.   Conti, M., Falini, G., and Samori, B., (2000). How Strong Is the Coordination Bond between a Histidine Tag and Ni - Nitrilotriacetate? An Experiment of Mechanochemistry on Single Molecules. Angewandte Chemie International Edition English, **39**: 215-218.

186.   Karshikoff, A., (2006), Non-Covalent Interactions in Proteins. Imperial College Press.

187.   Nyakatura, E. K., Reimann, O., Vagt, T., Salwiczek, M., and Koksch, B., (2013). Accommodating fluorinated amino acids in a helical peptide environment. RSC Advances, **3**: 6319-6322.

188.   Kothakota, S., Dougherty, M. J., Fournier, M. J., Mason, T. L., Yoshikawa, E., and Tirrell, D. A., (1995). Templated biological synthesis of polymers of abiological monomers. Macromolecular Symposia, **98**: 573-583.

189.   Robalo, J. R., Huhmann, S., Koksch, B., and Vila Verde, A., (2017). The Multiple Origins of the Hydrophobicity of Fluorinated Apolar Amino Acids. Chem, **3**: 881-897.

190. Buer, B. C., Levin, B. J., and Marsh, E. N., G. , (2012). Influence of Fluorination on the Thermodynamics of Protein Folding. Journal of the American Chemical Society, **134**: 13027–13034.

191. Jacobson, K. A., (1996). Fluorine-containing Amino Acids. Synthesis and Propertie. Journal of Medicinal Chemistry, **39**: 4132-4132.

192. Bott, G., Field, L. D., and Sternhell, S., (1980). Steric effects. A study of a rationally designed system. Journal of the American Chemical Society, **102**: 5618-5626.

193. Huhmann, S., Nyakatura, E. K., Erdbrink, H., Gerling, U. I. M., Czekelius, C., and Koksch, B., (2015). Effects of single substitutions with hexafluoroleucine and trifluorovaline on the hydrophobic core formation of a heterodimeric coiled coil. Journal of Fluorine Chemistry, **175**: 32-35.

194. Buer, B. C., Meagher, J. L., Stuckey, J. A., and Marsh, E. N. G., (2012). Comparison of the structures and stabilities of coiled-coil proteins containing hexafluoroleucine and t-butylalanine provides insight into the stabilizing effects of highly fluorinated amino acid side-chains. Protein Science, **21**: 1705-1715.

195. Cametti, M., Crousse, B., Metrangolo, P., Milani, R., and Resnati, G., (2012). The fluorous effect in biomolecular applications. Chemical Society Reviews, **41**: 31-42.

196. Jäckel, C., Seufert, W., Thust, S., and Koksch, B., (2004). Evaluation of the Molecular Interactions of Fluorinated Amino Acids with Native Polypeptides. Chembiochem, **5**: 717-720.

197. Tang, Y., Ghirlanda, G., Vaidehi, N., Kua, J., Mainz, D. T., Goddard, I. W., DeGrado, W. F., and Tirrell, D. A., (2001). Stabilization of coiled-coil peptide domains by introduction of trifluoroleucine. Biochemistry, **40**: 2790-2796.

198. Son, S., Tanrikulu, I. C., and Tirrell, D. A., (2006). Stabilization of bzip peptides through incorporation of fluorinated aliphatic residues. Chembiochem, **7**: 1251-1257.

199. Zhao, Y. H., Abraham, M. H., and Zissimos, A. M., (2003). Fast calculation of van der Waals volume as a sum of atomic and bond contributions and its application to drug compounds. Journal of Organic Chemistry, **68**: 7368-7373.

200. Cao, Y., Yoo, T., Zhuang, S., and Li, H., (2008). Protein-protein interaction regulates proteins' mechanical stability. Journal of Molecular Biology, **378**: 1132-1141.

201. Zhang, Y., Ge, C., Zhu, C., and Salaita, K., (2014). DNA-based digital tension probes reveal integrin forces during early cell adhesion. Nature Communications, **5**: 5167.

202. Wang, D., Hu, Y., Liu, P., and Luo, D., (2017). Bioresponsive DNA Hydrogels: Beyond the Conventional Stimuli Responsiveness. Accounts of Chemical Research, **50**: 733-739.

203. Sun, Z., Martinez-Lemus, L. A., Trache, A., Trzeciakowski, J. P., Davis, G. E., Pohl, U., and Meininger, G. A., (2005). Mechanical properties of the interaction between fibronectin and alpha5beta1-integrin on vascular smooth muscle cells studied using atomic force microscopy. American Journal of Physiology-Heart and Circulatory Physiology, **289**: H2526-2535.

204. Li, F., Redick, S. D., Erickson, H. P., and Moy, V. T., (2003). Force measurements of the alpha5beta1 integrin-fibronectin interaction. Biophysical Journal, **84**: 1252-1262.

205. Goktas, M. and Blank, K. G., (2017). Molecular Force Sensors: From Fundamental Concepts toward Applications in Cell Biology. Advanced Materials Interfaces, **4**: 1600441.

206. Liu, Y., Galior, K., Ma, V. P., and Salaita, K., (2017). Molecular Tension Probes for Imaging Forces at the Cell Surface. Accounts of Chemical Research, **50**: 2915-2924.

207. Morfill, J., Kuhner, F., Blank, K., Lugmaier, R. A., Sedlmair, J., and Gaub, H. E., (2007). B-S transition in short oligonucleotides. Biophysical Journal, **93**: 2400-2409.

208. Krautbauer, R., Rief, M., and Gaub, H. E., (2003). Unzipping DNA Oligomers. Nano Letters, **3**: 493–496.

209. Hatch, K., Danilowicz, C., Coljee, V., and Prentiss, M., (2008). Demonstration that the shear force required to separate short double-stranded DNA does not increase significantly with sequence length for sequences longer than 25 base pairs. Physical Review E, **78**: 011920.

210. Albrecht, C., Blank, K., Lalic-Multhaler, M., Hirler, S., Mai, T., Gilbert, I., Schiffmann, S., Bayer, T., Clausen-Schaumann, H., and Gaub, H. E., (2003). DNA: a programmable force sensor. Science, **301**: 367-370.

211. Wang, X. and Ha, T., (2013). Defining single molecular forces required to activate integrin and notch signaling. Science, **340**: 991-994.

212. Blakely, B. L., Dumelin, C. E., Trappmann, B., McGregor, L. M., Choi, C. K., Anthony, P. C., Duesterberg, V. K., Baker, B. M., Block, S. M., Liu, D. R., and Chen, C. S., (2014). A DNA-based molecular probe for optically reporting cellular traction forces. Nature Methods, **11**: 1229-1232.

11.   LIST OF FIGURES

12. LIST OF TABLES

13. APPENDIX

Table of Contents

1.   Peptide purification and characterization

The A4$_{H-2}$ peptide was synthesized in house. The procedure is described in Materials and Methods (Section 6.1.1.). The results of the HPLC purification and the characterization of the peptide is shown here.
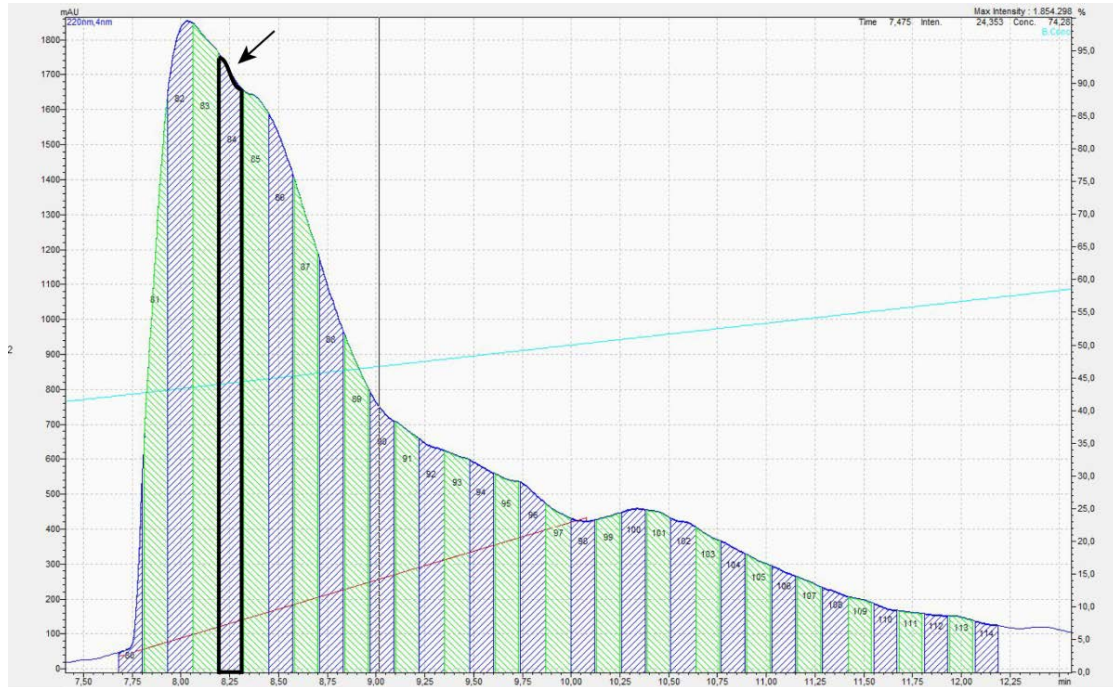
FIGURE A1 - Preparative HPLC chromatogram of the A4$_{H-2}$ fraction used in the CD and SMFS-based AFM measurements. Its corresponding measured molecular weight is shown in Figure A2. A linear gradient from 20-100 % ACN + 0.1% TFA was used at a flow rate of 25 ml min^{-1}.
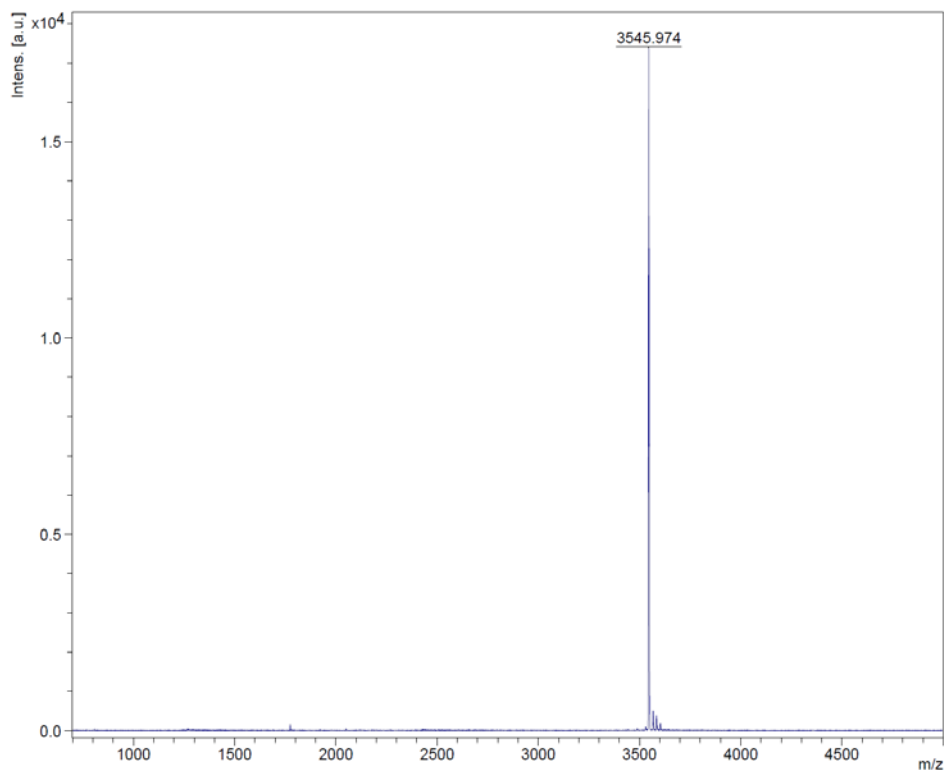
FIGURE A2 - MALDI-TOF spectrum of the purified fraction of the A4$_{H-2}$ peptide. The peptide shows a molecular weight of 3545.97 Da. It corresponds to the marked fraction in the preparative HPLC chromatogram in Figure A1. The calculated molecular weight of the peptide is 3543.89 Da.

TABLE A 1 - Sequences and origin of all the peptides used in this work. Highlighted in bold, mutations in each peptide sequences are shown. H and H form the metal-coordination staple upon addition of Ni^{2+} (A4$_{H-2}$) and K and D form the lactam-bridge staple (A4$_{x-2}$, B4$_{x-2}$). G= (S)-4,4,4-trifluoroethylglycine. nd= not determined.

| Name	Sequence	Origin	Molecular weight (g/mol)	Purity
A4	Ac–CGG EIAALEQ EIAALEK ENAALEW EIAALEQ GG –NH$_2$	Centic Biotec	3468,86	>96,57
B4	Ac– GG KIAALKY KIAALKY KNAALKW EIAALEQ GGC–NH$_2$	Centic Biotec	3438,30	>95,76
A4$_{S1-4}$	Ac–CGG EISALEQ EISALEK ENSALEW KIAALKQ GG –NH$_2$	Centic Biotec	3532,86	>95.10
B4$_{S1-4}$	Ac– GG KISALKY KNSALKK KISALKQ GGC–NH$_2$	Centic Biotec	3502,29	>95,76
A4$_{V1-4}$	Ac–CGG EVAALEQ EVAALEK ENAALEW EVAALEQ GG –NH$_2$	Centic Biotec	3426,78	>95,22
B4$_{V1-4}$	Ac– GG KVAALKY KVAALKY KNAALKK KVAALKQ GGC–NH$_2$	Centic Biotec	3396,22	>95.10
A4$_2$	Ac– GG EIAALEQ EIAALEK ENAALEW EIAALEQ GGC–NH$_2$	Collaborator 1*	3470,9	nd
B4$_2$	Ac–CGG KIAALKY KIAALKY KNAALKK KIAALKQ GG –NH$_2$	Collaborator 1*	3438,28	nd
A4$_{H-2}$	Ac– GG EIAALEW EIHALEH GGC–NH$_2$	MPIKG**	3543,89	nd
B4$_2$	Ac– GG KIAALKY KNAALKK KIAALKQ GG –NH$_2$	Collaborator 1*	3496,9	nd
A4$_{x-2}$	Ac– GG EIAALEW EIKALED GGC–NH$_2$	Collaborator 1*	3473,39	nd
B4$_{x-2}$	Ac–CGG KIAALKY KNAALKK KIKALKD GG –NH$_2$	Collaborator 2***	3438,28	nd
A4$_F$	Ac–CGG EIAALEQ EIAAGEK ENAALEW EIAALEQ GG –NH$_2$	Collaborator 2***	3493,61	nd
B4$_F$	Ac– GG KIAAGKY KNAALKK KIAALKQ GGC–NH$_2$	Collaborator 2***	3463,01	nd

3. AFM cantilever and sensitivity calibration

TABLE A2 – Post-calibration values for each SMFS experiment.

	Optical sensitivity (nm V^{-1})			Spring constant (N m^{-1})		
	Cantilever 1	Cantilever 2	Cantilever 3	Cantilever 1	Cantilever 2	Cantilever 3
A4$_{S1-4}$/B4$_{S1-4}$	55.3	57.46	55.97	0.013	0.018	0.016
A4$_{V1-4}$/B4$_{V1-4}$	61.06	54.57	39.25	0.015	0.013	0.023
A4$_{X-2}$/B4$_2$	47.13	49.82	49.51	0.018	0.019	0.018
A4$_2$/B4$_{X-2}$	52.81	42.30	46.54	0.013	0.019	0.018
A4$_{X-2}$/B4$_{X-2}$	49.42	46.73	49.54	0.017	0.019	0.017
A4$_2$/B4$_2$ in PIPPS-BS	50.89	42.04	44.69	0.015	0.016	0.013
A4$_{H-2}$/B4$_2$ in PIPPS-BS + Ni^{2+}	46.81	46.95	50.58	0.016	0.017	0.013
A4/B4$_F$	52.56	54.83	43.26	0.013	0.011	0.016
A4$_2$/B4$_2$	45.61	47.44	53.09	0.014	0.014	0.011
A4$_2$/B4	42.77	-	-	0.011	-	-
A4$_{X-2}$/B4	53.14	-	-	0.011	-	-

4. Supplementary data - Section 7.2. "Understanding Coiled Coil mechanics using a sequence-based approach"

Here, all data of the thermodynamic and mechanical measurements is shown. Each measurement was performed in triplicate. For the AFM experiments, one example data set is shown (rupture force and loading rate histograms for each retract speed). The extracted values from the CD spectroscopy and SMFS-based AFM measurements are shown for each measurement together with the mean ± SEM.

TABLE A3 – Summary of the thermodynamic values extracted from the CD-thermal denaturation measurements in Section 7.2. Experiments were performed in triplicate. All values are depicted as mean ± standard error of the mean (SEM).

		1	2	3	Mean ± SEM
A4/B4	T_m (°C)	77.6	76.6	76.9	77.0 ± 0.3
	ΔH ($k_B T$)	100.6	94.7	93.9	96.4 ± 2.1
	ΔS (k_B)	0.29	0.27	0.27	0.28 ± 0.01
	ΔG_{N-U} ($k_B T$)	14.8	13.9	13.8	14.2 ± 0.3
A4$_{S1-4}$/ B4$_{S1-4}$	T_m (°C)	54.9	53.9	54.2	54.3± 0.3
	ΔH ($k_B T$)	63.0	68.9	62.7	64.9 ± 2.0
	ΔS (k_B)	0.19	0.21	0.19	0.2 ± 0.01
	ΔG_{N-U} ($k_B T$)	5.5	4.8	5.5	5.3 ± 0.2
A4$_{V1-4}$/ B4$_{V1-4}$	T_m (°C)	60.1	58.3	58.6	59.0 ± 0.6
	ΔH ($k_B T$)	77.1	66.5	64.3	69.3 ± 3.9
	ΔS (k_B)	0.23	0.20	0.19	0.21 ± 0.01
	ΔG_{N-U} ($k_B T$)	8.2	6.7	6.3	7.1 ± 0.6

FIGURE A3 - Representative data set for A4/B4 (cantilever 1 in Table A3). The dashed lines correspond to the Gaussian fits applied to determine the most probable rupture force (A) and loading rate (B). The loading rate graphs are plotted logarithmically. n = Number of force-distance curves analyzed for each histogram.

FIGURE A4 – Representative data set for A4_{S1-4}/B4_{S1-4} (cantilever 2 in Table A3). The dashed lines correspond to the Gaussian fits applied to determine the most probable rupture force (A) and loading rate (B). The loading rate graphs are plotted logarithmically. n = Number of force-distance curves analyzed for each histogram.
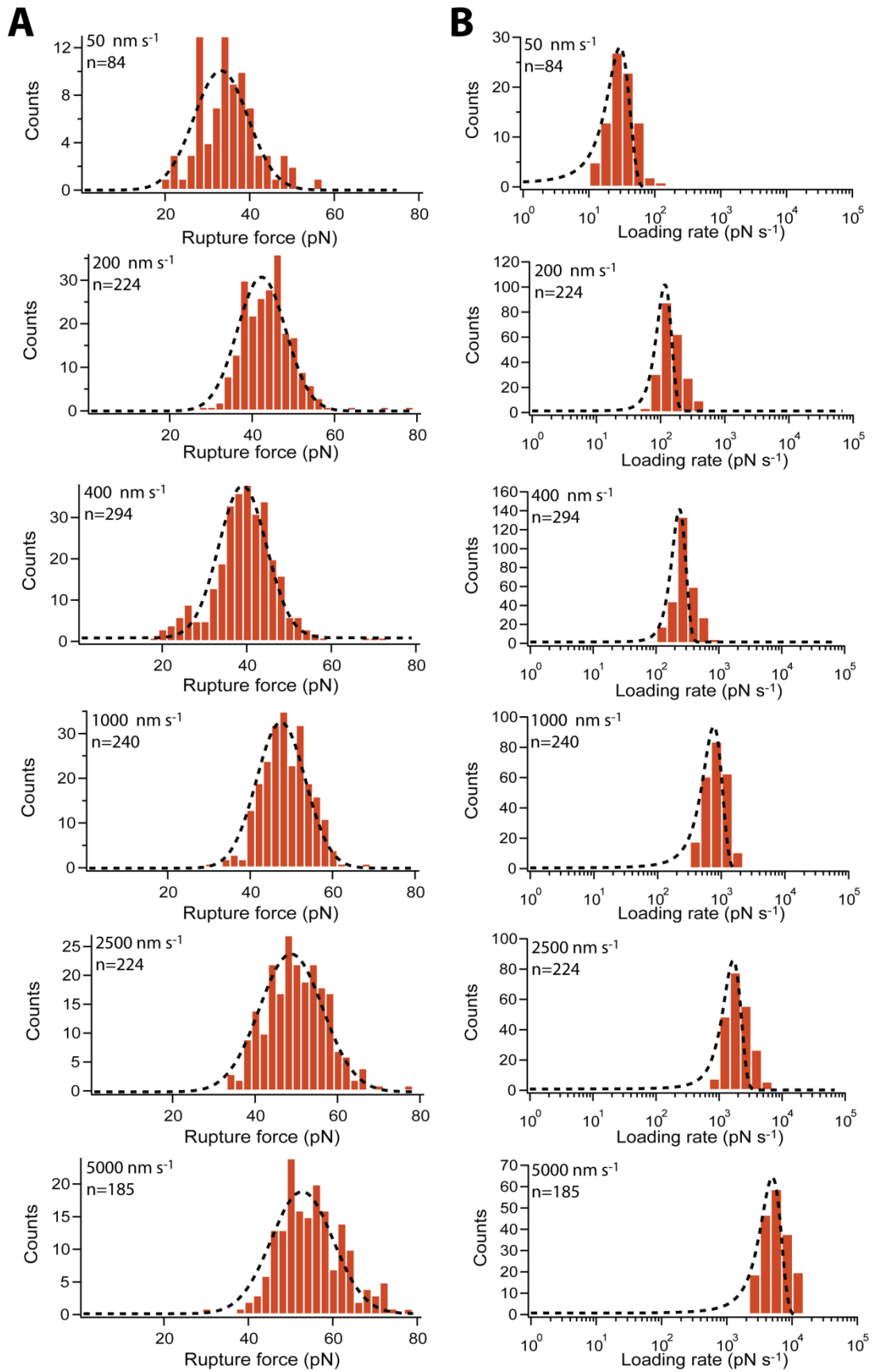
FIGURE A5 - Representative data set for A4$_{V1-4}$/B4$_{V1-4}$ (cantilever 3 in Table A3). The dashed lines correspond to the Gaussian fits applied to determine the most probable rupture force (A) and loading rate (B). The loading rate graphs are plotted logarithmically. n = Number of force-distance curves analyzed for each histogram.
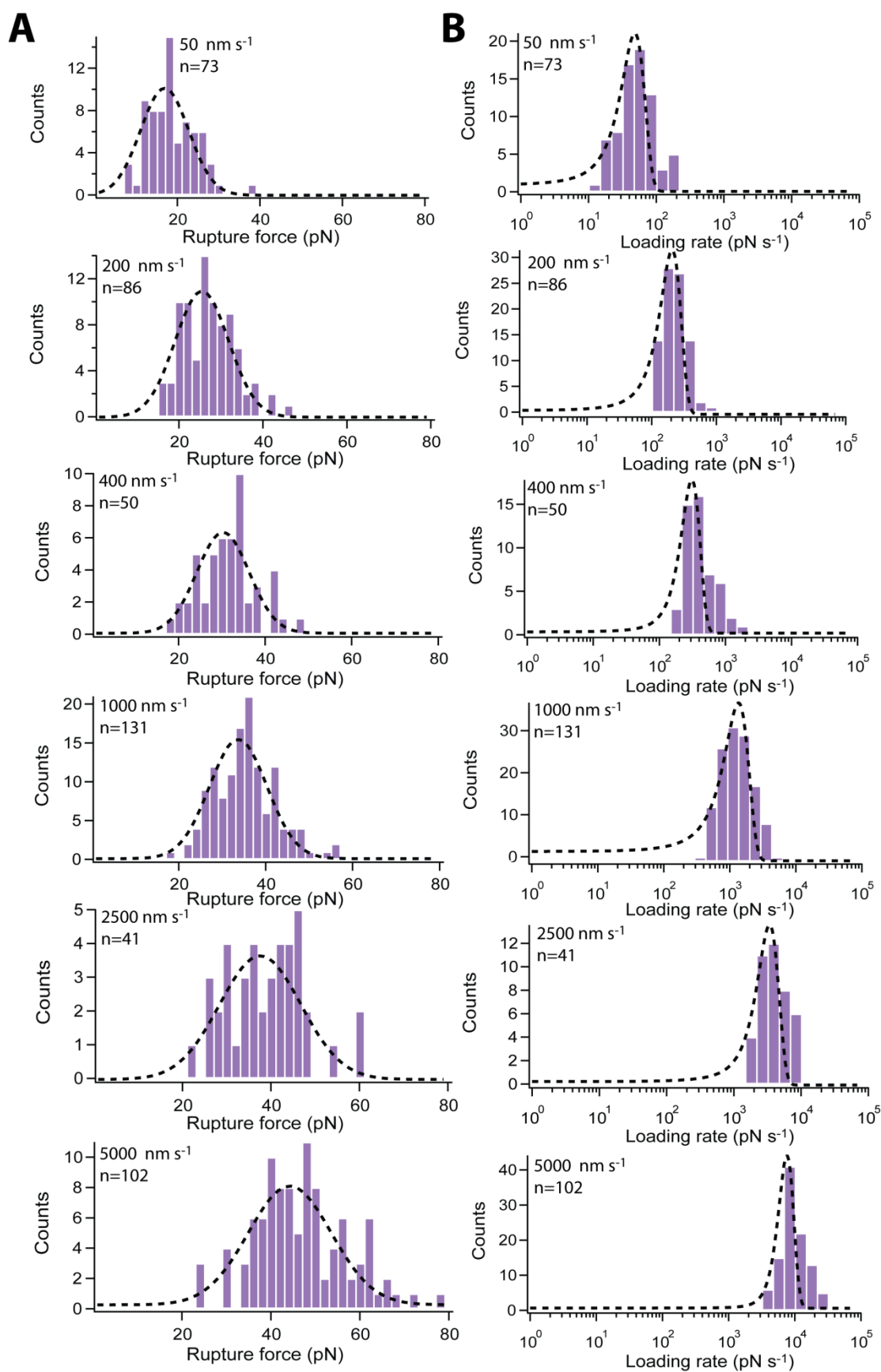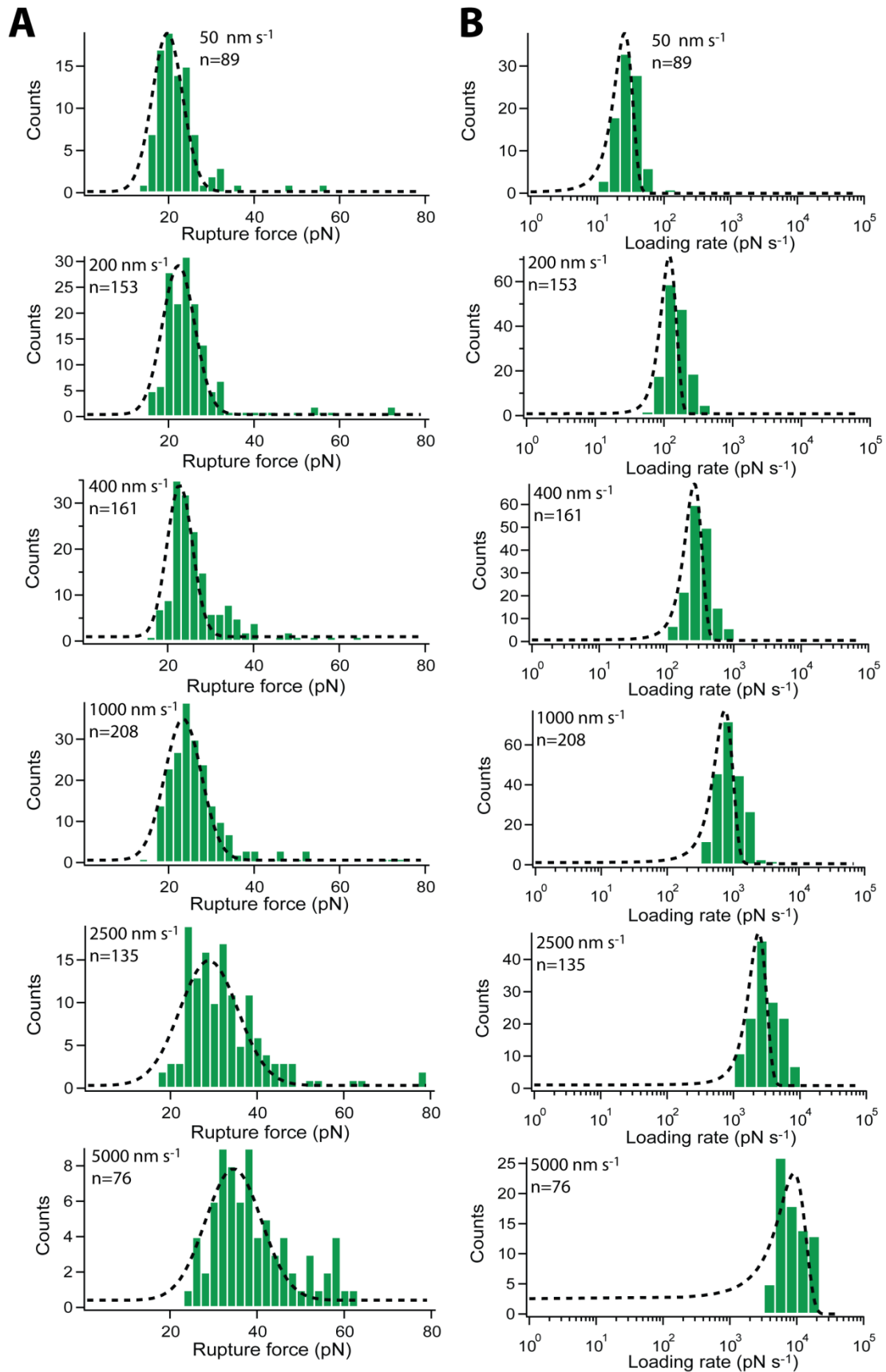
TABLE A4 - Values of the most probable rupture forces (*F*) and loading rates (*r*), obtained for the different retract speeds. n = number of force-distance included in the analysis. The data sets shown in figures A3, A4 and A5 are highlighted in bold.

Sequence	v (nm s^{-1})	1 F (pN)	1 r (pN s^{-1})	1 n	2 F (pN)	2 r (pN s^{-1})	2 n	3 F (pN)	3 r (pN s^{-1})	3 n
A4/B4	**50**	**33.2**	**30**	**84**	34.2	27	202	41.1	63	155
	200	**42.3**	**117**	**224**	40.6	117	168	41.0	267	238
	400	**39.0**	**237**	**294**	43.7	236	136	42.5	521	210
	1000	**47.4**	**764**	**240**	46.1	547	139	46.8	1505	146
	2500	**48.7**	**1678**	**224**	49.1	1530	105	47.7	4044	124
	5000	**52.8**	**4987**	**185**	51.9	4807	159	49.8	10069	97
A4$_{S1-4}$/ B4$_{S1-4}$	50	-	-	-	**16.1**	**35**	**19**	16.9	48	73
	200	22.3	190	85	**20.0**	**193**	**145**	25.5	207	86
	400	24.0	480	82	**25.4**	**492**	**99**	30.3	310	50
	1000	25.0	1353	53	**30.0**	**1187**	**67**	33.7	1355	131
	2500	36.1	3260	43	**33.4**	**2433**	**43**	37.6	3394	41
	5000	-	-	-	**35.7**	**7078**	**25**	44.3	7611	102
A4$_{V1-4}$/ B4$_{V1-4}$	50	22.1	18	85	21.6	31	151	**19.7**	**26**	**89**
	200	27.6	161	302	27.3	169	112	**22.3**	**120**	**153**
	400	28.2	321	422	35.6	517	80	**22.8**	**259**	**161**
	1000	36.1	1040	238	30.0	1000	60	**23.4**	**752**	**208**
	2500	34.3	3220	185	32.1	3070	23	**28.9**	**2394**	**135**
	5000	35.4	6731	79	-	-	-	**34.6**	**9072**	**76**

TABLE A5 – Summary of the kinetic and thermodynamic parameters obtained when varying the amino acid sequence.. Experiments are performed in triplicate. All values are depicted as mean ± standard error of the mean (SEM).

		1	2	3	Mean ± SEM
A4/B4	$\Delta x_{\text{N-TS}}$ **(nm)**	1.12	1.22	1.62	1.32 ± 0.15
	k_{off} **(s^{-1})**	7.3 x 10^{-4}	2.2 x 10^{-4}	7.3 x 10^{-6}	(3.2 ± 2.1) x 10^{-4}
	$\Delta G_{\text{N-TS}}$ **(k$_B$T)**	27.3	28.5	31.9	29.2 ± 1.4
A4$_{\text{S1-4}}$/ B4$_{\text{S1-4}}$	$\Delta x_{\text{N-TS}}$ **(nm)**	0.94	1.03	0.83	0.93 ± 0.06
	k_{off} **(s^{-1})**	4.0 x 10^{-1}	1.9 x 10^{-1}	2.5 x 10^{-1}	(2.8 ± 1.1) x 10^{-1}
	$\Delta G_{\text{N-TS}}$ **(k$_B$T)**	20.9	21.6	21.4	21.3 ± 0.2
A4$_{\text{V1-4}}$/ B4$_{\text{V1-4}}$	$\Delta x_{\text{N-TS}}$ **(nm)**	1.71	1.70	1.73	1.71 ± 0.01
	k_{off} **(s^{-1})**	6.6 x 10^{-4}	6.0 x 10^{-3}	7.3 x 10^{-4}	(2.4 ± 1.7) x 10^{-3}
	$\Delta G_{\text{N-TS}}$ **(k$_B$T)**	27.4	27.2	25.2	26.6 ±0.7

5. Supplementary data - Section 7.3. "Understanding the influence of the pulling geometry on Coiled Coil mechanics"

Here, all data of the thermodynamic and mechanical measurements is shown. Each measurement was performed in triplicate. For the AFM experiments, one example data set is shown (rupture force and loading rate histograms for each retract speed). The extracted values from the CD spectroscopy and SMFS-based AFM measurements are shown for each measurement together with the mean ± SEM.

TABLE A6 - Summary of the thermodynamic values extracted from the CD-thermal denaturation measurements in Section 7.3. Experiments are performed in triplicate. All values are depicted as mean ± standard error of the mean (SEM).

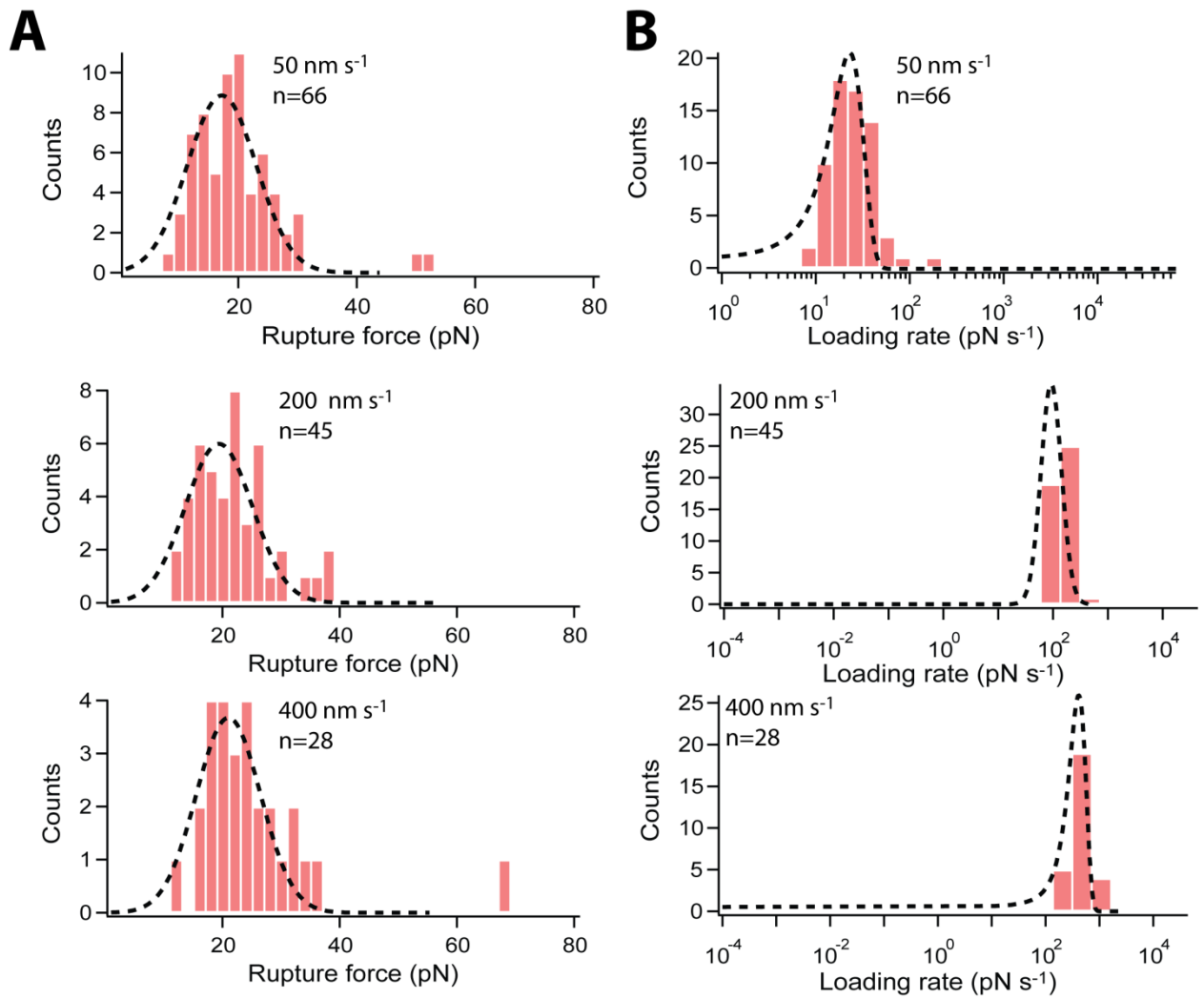|		1	2	3	Mean ± SEM
	T_m (°C)	77.7	77.9	75.2	76.9 ± 0.9
$A4_2/B4_2$	ΔH ($k_B T$)	86.3	67.9	76.8	77.0 ± 5.3
	ΔS (k_B)	0.25	0.20	0.22	0.22 ± 0.02
	ΔG_{N-U} ($k_B T$)	12.0	9.6	10.7	10.7 ± 0.7
	T_m (°C)	77.6	77.6	74.8	76.6 ± 0.9
$A4_2/B4$	ΔH ($k_B T$)	94.2	93.9	77.5	88.5 ±5.5
	ΔS (k_B)	0.27	0.27	0.22	0.25 ± 0.02
	ΔG_{N-U} ($k_B T$)	13.1	13.0	10.8	12.3 ± 0.8

FIGURE A6 – Representative data set for A4$_2$/B4 (Table A8). The dashed lines correspond to the Gaussian fits applied to determine the most probable rupture force (A) and loading rate (B). The loading rate graphs are plotted logarithmically. n = Number of force-distance curves analyzed for each histogram.

FIGURE A 7 - Representative data set for A4$_2$/B4$_2$ (cantilever 2 in table A7). The dashed lines correspond to the Gaussian fits applied to determine the most probable rupture force (A) and loading rate (B). The loading rate graphs are plotted logarithmically. n = Number of force-distance curves analyzed for each histogram.
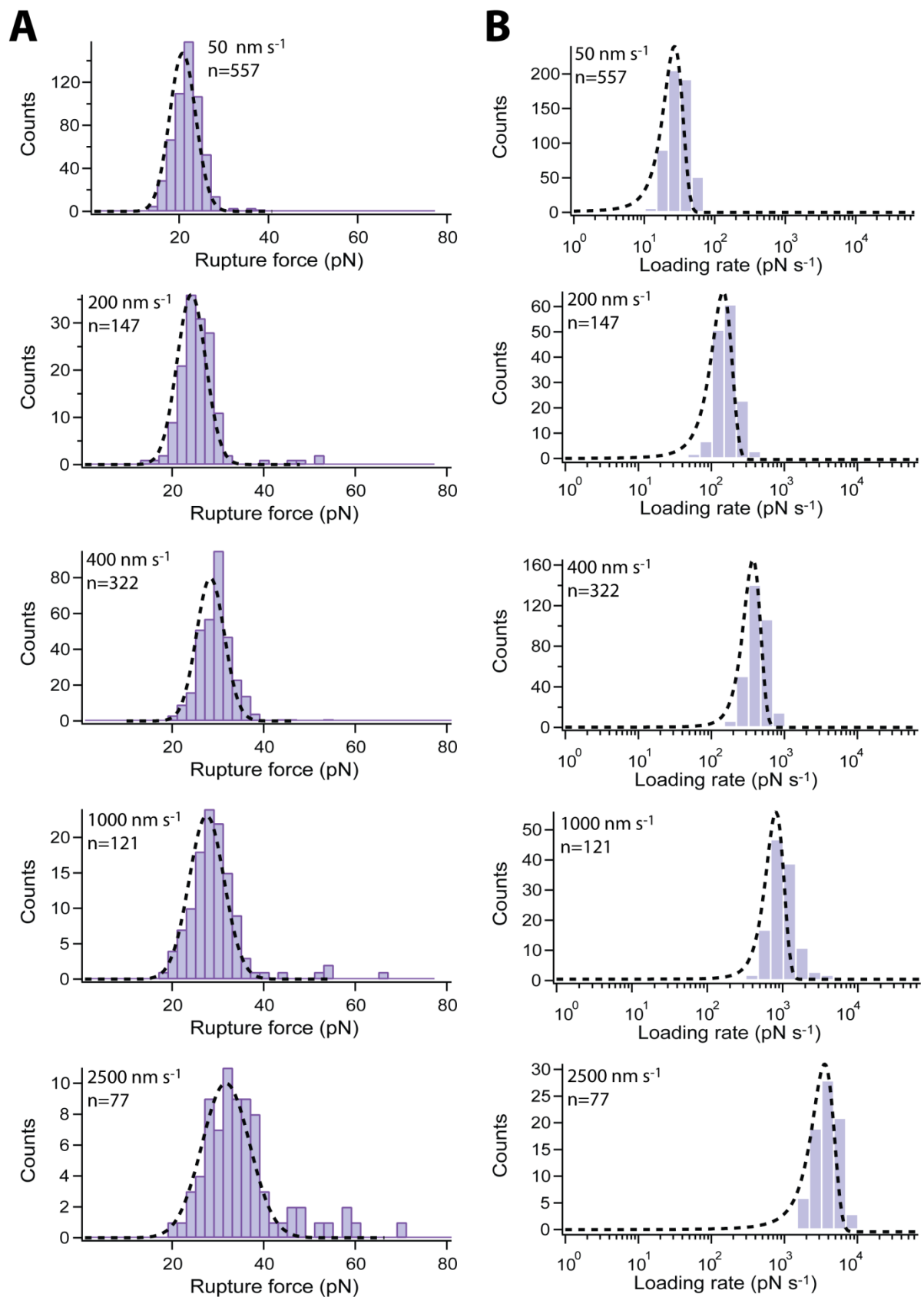
TABLE A7 - Values of the most probable rupture forces (*F*) and loading rates (*r*), obtained for the different retract speeds. n = number of force-distance included in the analysis. The data sets shown in Figure A6 and A7 are highlighted in bold.

Sequence	v (nm s^{-1})	*F* (pN)	*r* (pN s^{-1})	n	F (pN)	*r* (pN s^{-1})	n	F (pN)	*r* (pN s^{-1})	n
		1			**2**			**3**		
	50	23.7	32.8	666	**20.8**	**26.85**	**557**	22.3	25.9	225
	200	27.4	149.6	202	**24.2**	**144.6**	**147**	23.7	111.5	115
	400	29.3	351.6	350	**28.4**	**371.9**	**322**	25.7	262.2	171
A4$_2$/B4$_2$	**1000**	30.3	994.7	334	**27.6**	**815.8**	**121**	27.6	821.2	132
	2500	31.6	2779.4	110	**31.8**	**3566.2**	**77**	31.6	2495.2	105
	5000	38.4	8629.6	50	-	-	-	-	-	-
	50	**17.2**	**22.9**	**66**	-	-	-	-	-	-
A4$_2$/B4	**200**	19.4	92.7	45	-	-	-	-	-	-
	400	21.0	412.9	28	-	-	-	-	-	-

TABLE A8 - Summary of the kinetic and thermodynamic parameters obtained when varying the pulling geometry. Experiments are performed in triplicate. All values are depicted as mean ± standard error of the mean (SEM).

		1	2	3	Mean ± SEM
	Δx_{N-TS} (nm)	1.75	1.85	2.07	1.89 ± 0.09
A4$_2$/B4$_2$	k_{off} (s^{-1})	6.1 x 10^{-4}	9.2 x 10^{-4}	2.5 x 10^{-4}	(6.0 ± 1.9) x 10^{-4}
	ΔG_{N-TS} (k$_B$T)	27.4	27.0	28.3	27.6 ± 0.4

6. Supplementary data - Section 7.4. "Tuning helix thermodynamics and mechanics with "stapled" peptides

Here, all data of the thermodynamic and mechanical measurements is shown. Each measurement was performed in triplicate. For the AFM experiments, one example data set is shown (rupture force and loading rate histograms for each retract speed). The extracted values from the CD spectroscopy and SMFS-based AFM measurements are shown for each measurement together with the mean ± SEM.

TABLE A9 - **Summary of the thermodynamic values extracted from the CD-thermal denaturation measurements.**. Experiments are performed in triplicate. All values are depicted as mean ± standard error of the mean (SEM).

|		1	2	3	Mean ± SEM
$A4_{X-2}$/ $B4_2$	T_m (°C)	81.1	81.1	81.2	81.1 ± 0.0
	ΔH ($k_B T$)	87.9	108.8	80.7	92.5 ± 8.5
	ΔS (k_B)	0.25	0.31	0.23	0.26 ± 0.023
	ΔG_{N-U} ($k_B T$)	13.3	17.1	12.2	14.2 ± 1.5
$A4_2$/ $B4_{X-2}$	T_m (°C)	81.9	82.3	85	83.1 ± 0.9
	ΔH ($k_B T$)	100.7	98.5	87.6	95.6 ± 4.0
	ΔS (k_B)	0.29	0.28	0.25	0.27 ± 0.01
	ΔG_{N-U} ($k_B T$)	15.4	15.0	14.2	14.9 ± 0.3
$A4_{X-2}$/ $B4_{X-2}$	T_m (°C)	>95	>95	>95	>95
	ΔH ($k_B T$)	114.3	75.1	75.3	88.21 ± 13.0
	ΔS (k_B)	0.31	0.2	0.21	0.24 ± 0.04
	ΔG_{N-U} ($k_B T$)	21.4	14.1	14.0	16.5 ± 2.5
$A4_{H-2}$/ $B4_2$ in PIPPS-BS	T_m (°C)	75.8	76.2	76.2	76.1 ± 0.1
	ΔH ($k_B T$)	91.6	86.0	87.8	88.5 ± 1.6
	ΔS (k_B)	0.26	0.25	0.25	0.25 ± 0.004
	ΔG_{N-U} ($k_B T$)	13.1	12.0	12.6	12.5 ± 0.3
$A4_{H-2}$/ $B4_2$ in PIPPS-BS + Ni^{2+}	T_m (°C)	78.7	77	80.8	78.8 ± 1.1
	ΔH ($k_B T$)	98.6	115.3	95.8	103.2 ± 6.1
	ΔS (k_B)	0.28	0.33	0.27	0.29 ± 0.02
	ΔG_{N-U} ($k_B T$)	14.8	16.4	14.5	15.0 ± 0.7
$A4_{X-2}$/ $B4$	T_m (°C)	83.0	81.7	82.9	82.5 ± 0.4
	ΔH ($k_B T$)	63.9	86.6	73.6	74.7 ± 6.6
	ΔS (k_B)	0.18	0.25	0.21	0.21 ± 0.02
	ΔG_{N-U} ($k_B T$)	9.3	13.2	10.5	11.0 ± 1.2
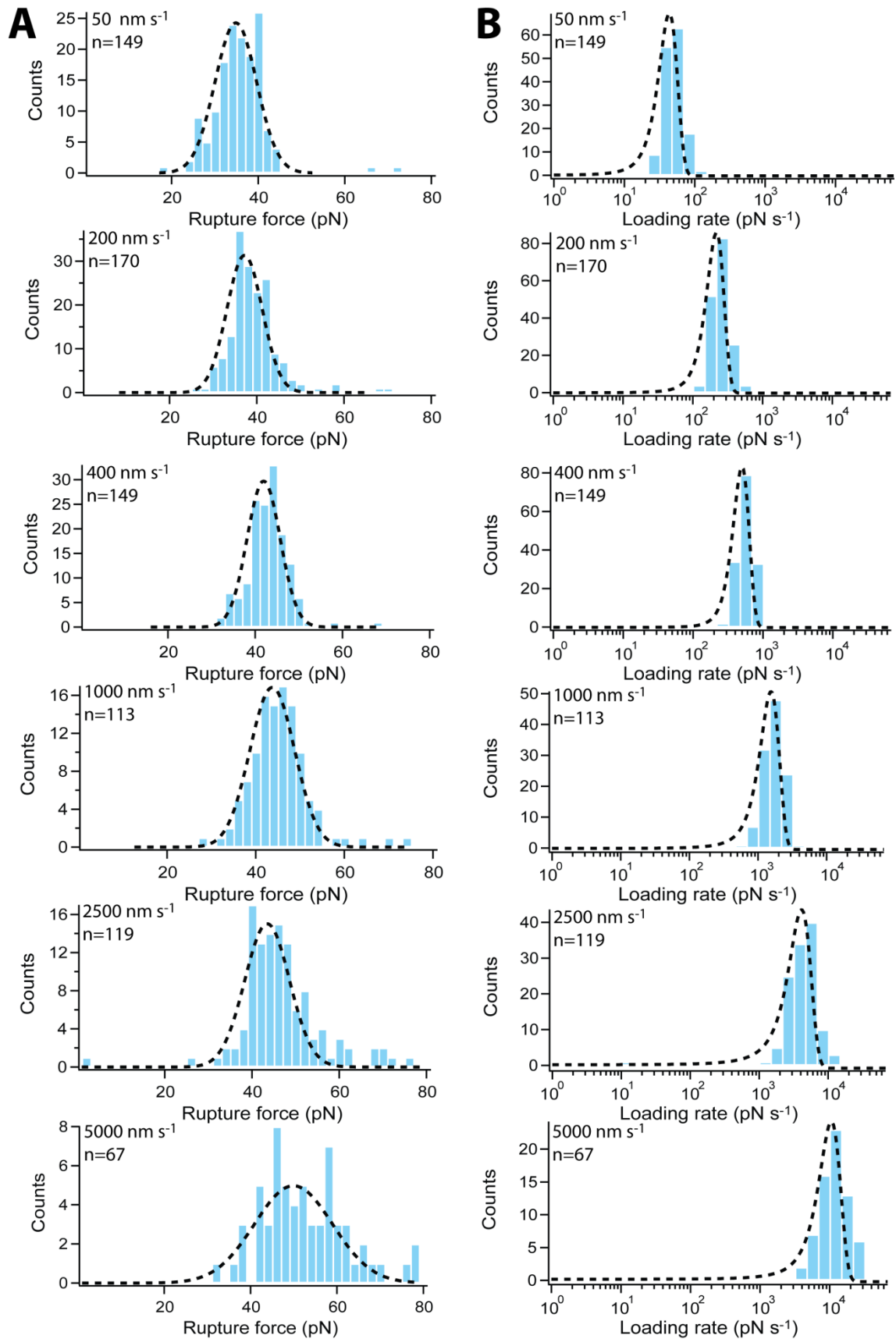
FIGURE A8 - Representative data set for A4$_{X-2}$/B42 (cantilever 3 in Table A9). The dashed lines correspond to the Gaussian fits applied to determine the most probable rupture force (A) and loading rate (B). The loading rate graphs are plotted logarithmically. n = Number of force-distance curves analyzed for each histogram.
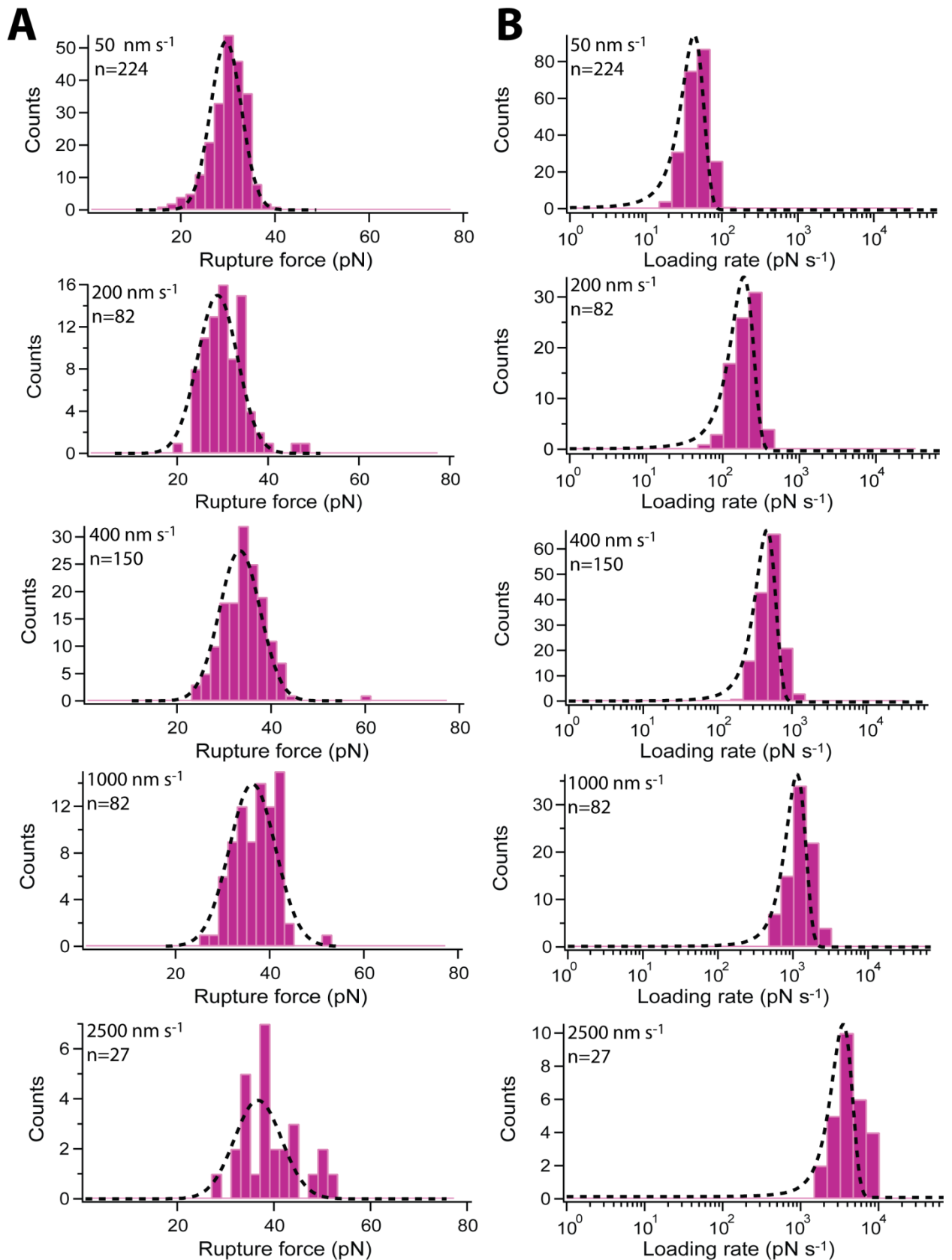
FIGURE A9 - Representative data set for A4$_2$/B4$_{X-2}$ (cantilever 2 in Table A9). The dashed lines correspond to the Gaussian fits applied to determine the most probable rupture force (A) and loading rate (B). The loading rate graphs are plotted logarithmically. n = Number of force-distance curves analyzed for each histogram.
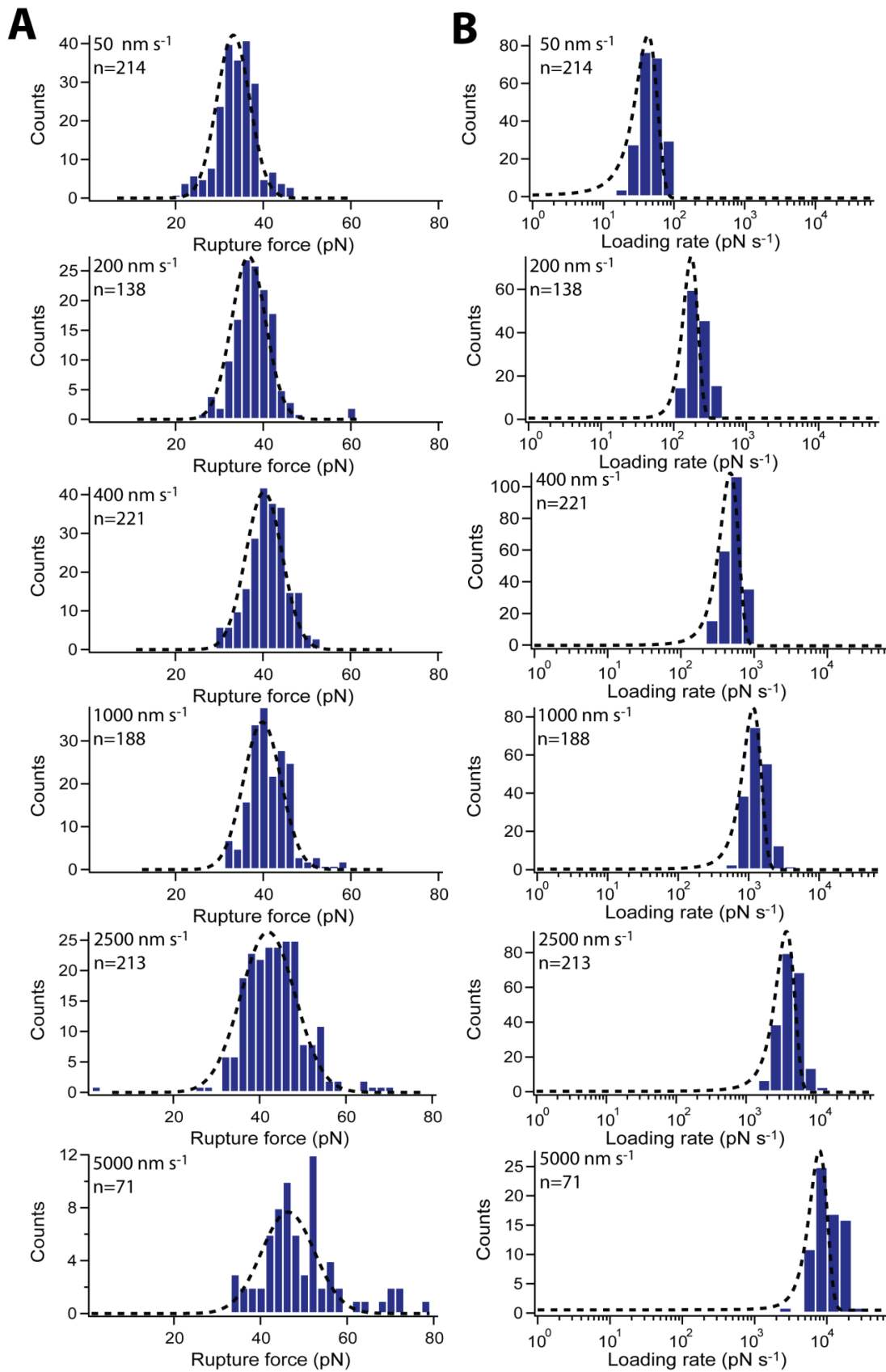
FIGURE A10 - **Representative data set for A4$_{X-2}$/B4$_{X-2}$** (cantilever 1 in Table A9). The dashed lines correspond to the Gaussian fits applied to determine the most probable rupture force (A) and loading rate (B). The loading rate graphs are plotted logarithmically. n = Number of force-distance curves analyzed for each histogram.
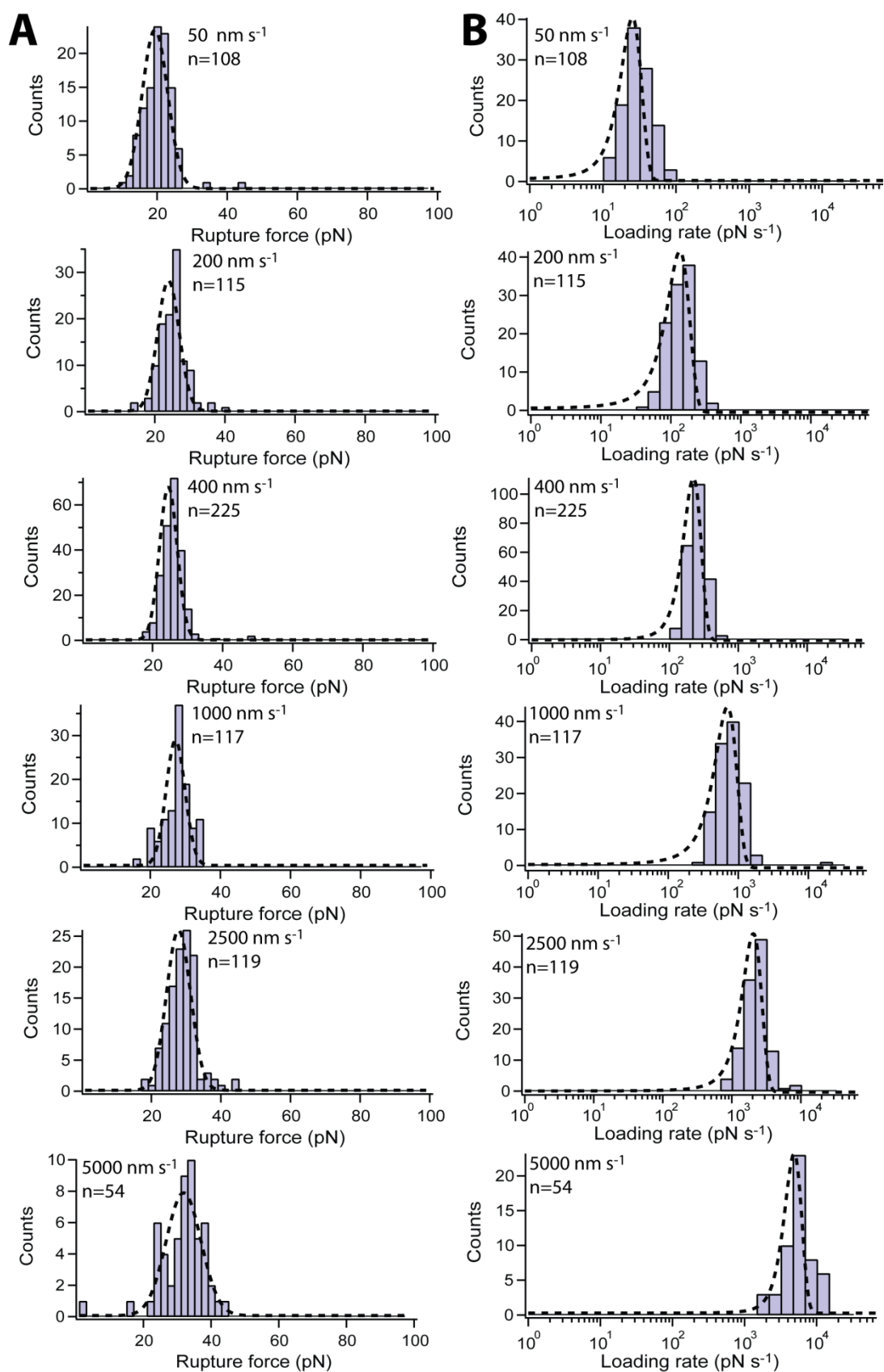
FIGURE A11 - Representative data set for A4₂/B4₂ in PIPPS-BS (cantilever 3 in Table A9). The dashed lines correspond to the Gaussian fits applied to determine the most probable rupture force (A) and loading rate (B). The loading rate graphs are plotted logarithmically. n = Number of force-distance curves analyzed for each histogram.

FIGURE A12 - Representative data set for A4$_{H-2}$/B4$_2$ in PIPPS-BS + Ni^{2+} (cantilever 2 in Table A9). The dashed lines correspond to the Gaussian fits applied to determine the most probable rupture force (A) and loading rate (B). The loading rate graphs are plotted logarithmically. n = Number of force-distance curves analyzed for each histogram.
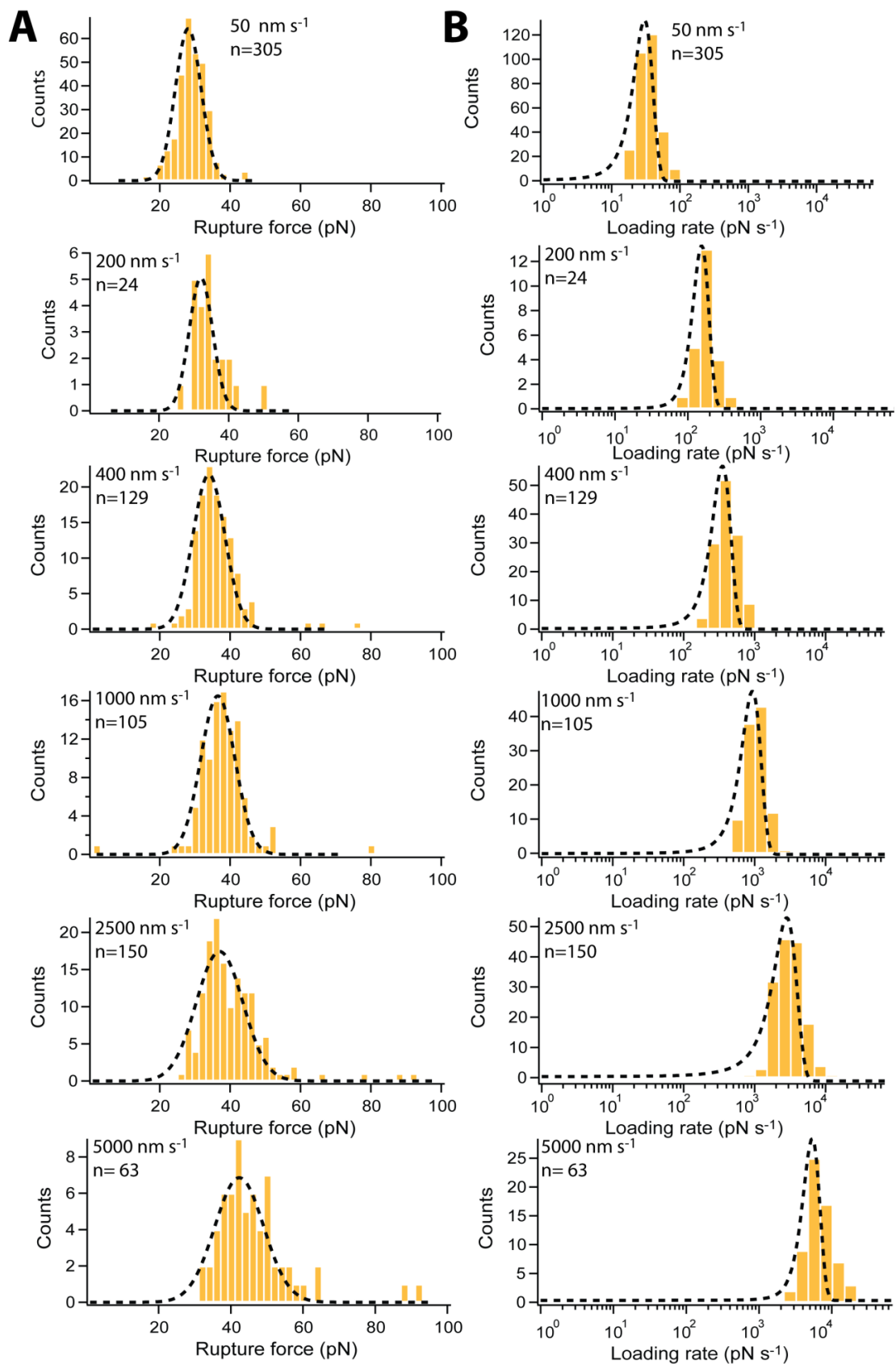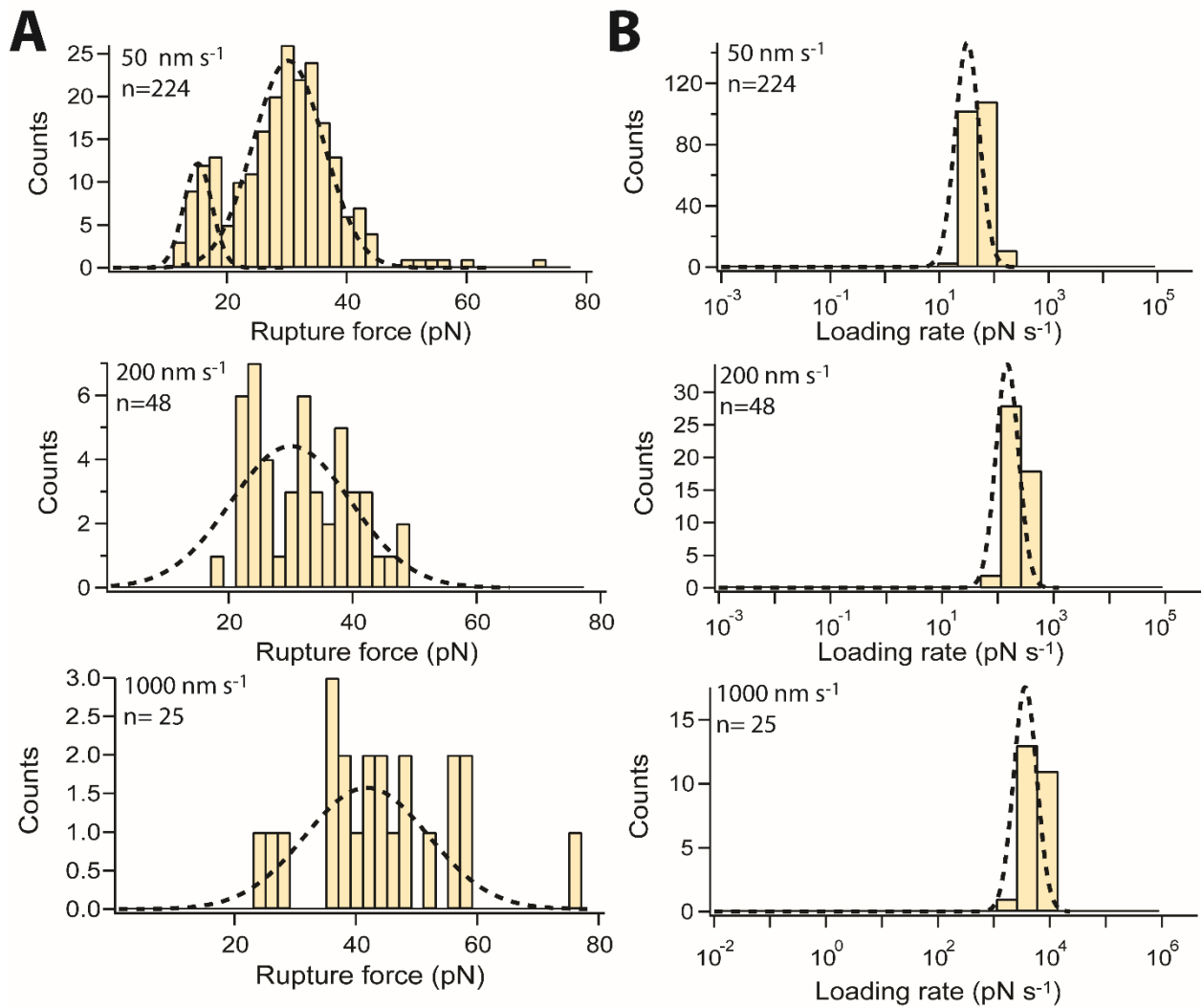
FIGURE A13 - Representative data set for A4$_{X-2}$/B4 (Table A9). The dashed lines correspond to the Gaussian fits applied to determine the most probable rupture force (A) and loading rate (B). The histogram measured at a retract speed of 50 nm s^{-1} shows two populations, each fitted with a Gaussian distribution. The first peak is suggested to correspond to a small fraction of the peptide without staple (A4$_2$/B4) and the second peak corresponds to A4$_{X-2}$/B4. The loading rate graphs are plotted logarithmically. n = Number of force-distance curves analyzed for each histogram.

TABLE A10 - Values of the most probable rupture forces (F) and loading rates (r), obtained for the different retract speeds. n = number of force-distance included in the analysis. The data sets shown in Figures A8-13 are highlighted in bold. Experiments were performed in triplicate.

		1			2			3		
Sequence	v (nm s⁻¹)	F (pN)	r (pN s⁻¹)	n	F (pN)	r (pN s⁻¹)	n	F (pN)	r (pN s⁻¹)	n
A4ₓ₋₂/ B4₂	50	36.3	36.1	196	36.2	53.6	209	**34.8**	**43.6**	**149**
	200	38.8	192.6	119	40.3	269.4	125	**37.2**	**217.7**	**170**
	400	39.0	500.6	113	46.9	516.9	128	**41.9**	**501.6**	**149**
	1000	44.8	1148.2	55	51.9	1638.5	68	**43.7**	**1544.2**	**113**
	2500	45.2	4301.5	54	53.6	4890.1	111	**43.5**	**4123.9**	**119**
	5000	50.9	10324.0	24	54.4	10377.0	63	**49.9**	**10579.0**	**67**
A4₂/ B4ₓ₋₂	50	22.3	31.7	123	**29.6**	**43.2**	**224**	29.7	40.4	333
	200	-	-	-	**28.9**	**187.3**	**82**	31.8	178.7	164
	400	31.0	317.8	97	**33.4**	**459.5**	**150**	38.8	422.6	207
	1000	32.3	1053.1	177	**36.3**	**1129.7**	**82**	37.7	1169.1	176
	2500	34.2	3194.3	73	**36.7**	**3521.8**	**27**	41.6	3724.8	149
	5000	39.6	9151.4	33	-	-	-	45.5	11677.0	48
A4ₓ₋₂/ B4ₓ₋₂	50	**33.2**	**43.1**	**214**	35.9	38.7	186	35.2	50.2	221
	200	**36.7**	**174.7**	**138**	40.6	217.9	53	39.8	225.2	157
	400	**40.2**	**474.2**	**221**	40.1	493.4	159	42.1	503.8	135
	1000	**39.8**	**1158.1**	**188**	40.2	1113.4	54	48.8	1786.5	152
	2500	**41.9**	**3790.3**	**213**	45.2	4159.8	57	51.1	4632.0	127
	5000	**46.4**	**7895.1**	**71**	-	-	-	57.3	1128.06	135
A4₂/ B4₂ in PIPPS-BS	50	23.2	30.1	111	19.0	23.5	60	**19.4**	**25.4**	**108**
	200	27.8	118.6	45	-	-	-	**23.9**	**134.3**	**115**
	400	29.3	326.6	121	23.7	297.8	117	**24.5**	**223.4**	**225**
	1000	31.5	798.1	109	28.3	1134.7	64	**27.2**	**699.4**	**117**
	2500	33.9	2589.1	87	27.8	2205	26	**27.8**	**2048.6**	**119**
	5000	36.5	5976.1	52	-	-	-	**31.9**	**4869.7**	**54**
A4ₕ₋₂/ B4₂ in PIPPS-BS + Ni²⁺	50	28.6	41.1	43	**28.1**	**30.2**	**305**	-	-	-
	200	32.6	169.1	67	**32.0**	**155.0**	**24**	31.3	180.2	78
	400	35.2	402.9	172	**34.0**	**352.7**	**129**	33.0	354.6	61
	1000	39.1	1423.5	66	**36.5**	**929.1**	**105**	34.9	970.5	102
	2500	38.7	4644.2	76	**37.0**	**2834.9**	**150**	37.7	3639.5	106
	5000	38.7	7431.1	44	**42.3**	**5375.7**	**63**	38.5	5398.5	41
A4ₓ₋₂/ B4	50	**30.3**	**32.3**	**224**	-	-	-	-	-	-
	200	30.0	147.6	48	-	-	-	-	-	-
	400	-	-	-	-	-	-	-	-	-
	1000	41.8	3624.0	25						

TABLE A11 - Summary of the kinetic and thermodynamic parameters obtained for the stapled CCs. Experiments are performed in triplicate. All values are depicted as mean ± standard error of the mean (SEM).

		1	2	3	Mean ± SEM
$A4_{X-2}/$ $B4_2$	Δx_{N-TS} (nm)	1.48	1.12	1.49	1.37 ± 0.15
	k_{off} (s^{-1})	5.3 x 10^{-5}	5.9 x 10^{-4}	7.0 x 10^{-5}	(2.4 ± 2.2) x 10^{-4}
	ΔG_{N-TS} (k$_B$T)	29.9	27.5	29.6	28.9 ± 0.8
$A4_2/$ $B4_{X-2}$	Δx_{N-TS} (nm)	1.47	1.83	1.45	1.58 ± 0.12
	k_{off} (s^{-1})	2.9 x 10^{-3}	7.3 x 10^{-5}	4.2 x 10^{-4}	(1.0 ± 0.9) x 10^{-3}
	ΔG_{N-TS} (k$_B$T)	25.9	29.5	27.8	27.7 ± 1.1
$A4_{X-2}/$ $B4_{X-2}$	Δx_{N-TS} (nm)	1.65	1.79	1.01	1.48 ± 0.24
	k_{off} (s^{-1})	3.6 x 10^{-5}	4.6 x 10^{-6}	2.6 x 10^{-3}	(9.0 ± 8.8) x 10^{-4}
	ΔG_{N-TS} (k$_B$T)	30.3	32.3	26.0	29.5 ± 1.9
$A4_2/$ $B4_2$ in PIPPS-BS	Δx_{N-TS} (nm)	1.73	1.95	1.90	1.86 ± 0.07
	k_{off} (s^{-1})	6.1 x 10^{-4}	1.3 x 10^{-3}	1.3 x 10^{-3}	(1.1 ± 0.2) x 10^{-3}
	ΔG_{N-TS} (k$_B$T)	27.4	26.6	26.7	26.9 ± 0.3
$A4_{H-2}/$ $B4_2$ in PIPPS-BS + Ni^{2+}	Δx_{N-TS} (nm)	1.85	1.68	1.69	1.74 ± 0.05
	k_{off} (s^{-1})	3.8 x 10^{-5}	1.4 x 10^{-4}	2.2 x 10^{-4}	(1.3 ± 0.5) x 10^{-4}
	ΔG_{N-TS} (k$_B$T)	30.2	28.9	28.4	29.2 ± 0.5

7. Supplementary data - Section 7.5. "Tuning Coiled Coil mechanics with fluorinated amino acids"

Here, all data of the thermodynamic and mechanical measurements is shown. Each measurement was performed in triplicate. For the AFM experiments, one example data set is shown (rupture force and loading rate histograms for each retract speed). The extracted values from the CD spectroscopy and SMFS-based AFM measurements are shown for each measurement together with the mean ± SEM.

TABLE A12 - Summary of the thermodynamic values extracted from the CD-thermal denaturation measurements. Experiments were performed in triplicate. All values are depicted as mean ± standard error of the mean (SEM).

		1	2	3	Mean ± SEM
A4/B4$_F$	T_m (°C)	70.1	68.7	68.1	68.9 ± 0.6
	ΔH ($k_B T$)	102.2	81.8	92.2	92.1 ± 5.9
	ΔS (k_B)	0.30	0.24	0.27	0.27 ± 0.02
	ΔG_{N-U} ($k_B T$)	13.1	9.9	11.2	11.4 ± 0.9
A4$_F$/B4	T_m (°C)	65.8	65.2	64.9	65.3 ± 0.3
	ΔH ($k_B T$)	65.7	69.2	73.2	69.4 ± 2.2
	ΔS (k_B)	0.19	0.21	0.22	0.21 ± 0.01
	ΔG_{N-U} ($k_B T$)	7.1	7.6	8.1	7.6 ± 0.3
A4$_F$/B4$_F$	T_m (°C)	56.4	56.4	56.1	56.3 ± 0.1
	ΔH ($k_B T$)	73.3	66.9	64.8	68.3 ± 2.6
	ΔS (k_B)	0.22	0.20	0.20	0.21 ± 0.01
	ΔG_{N-U} ($k_B T$)	6.6	6.0	5.8	6.2 ± 0.2
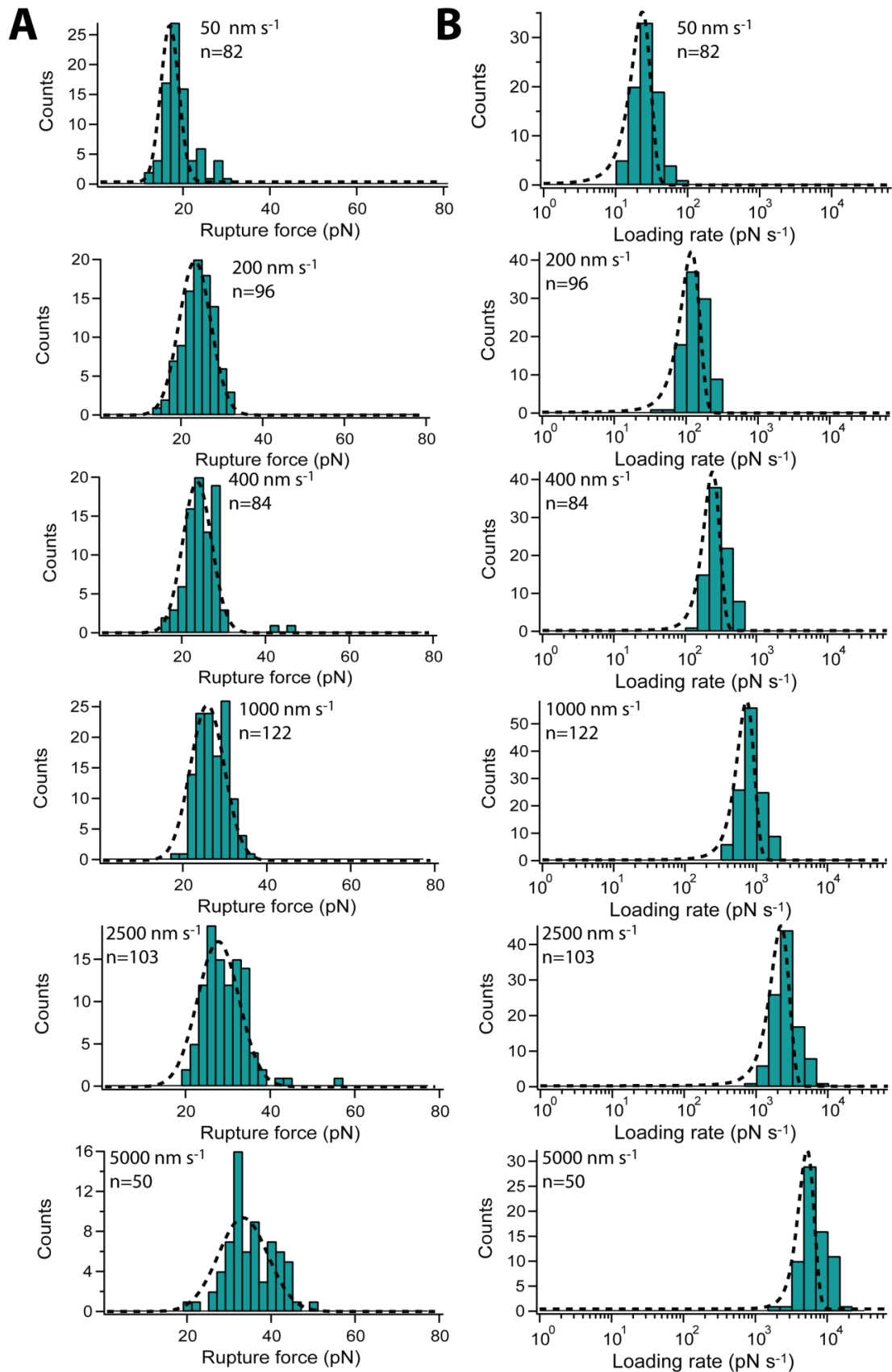
FIGURE A14 - Representative data set for A4/B4₍F₎ (cantilever 3 in Table A13). The dashed lines correspond to the Gaussian fits applied to determine the most probable rupture force (A) and loading rate (B). The loading rate graphs are plotted logarithmically. n = number of force-distance curves analyzed for each histogram.

TABLE A13 - Values of the most probable rupture forces (*F*) and loading rates (*r*), obtained for the different retract speeds. n = number of force-distance included in the analysis. The data sets shown in Figure A14 are highlighted in bold.

Sequence	v (nm s^{-1})	1				2			3		
		F (pN)	r (pN s^{-1})	n	F (pN)	r (pN s^{-1})	n	F (pN)	r (pN s^{-1})	n
	50	19.6	20.9	50	14.4	16.8	108	**16.9**	**23.4**	**82**
	200	23.8	114.1	119	19.2	105.5	132	**23.4**	**118.7**	**96**
	400	24.8	312.5	153	20.2	238.6	134	**23.7**	**243.9**	**84**
A4/B4$_F$	**1000**	29.8	935.2	120	22.6	697.9	107	**25.8**	**733.5**	**122**
	2500	31.6	2988.8	134	25.6	2394.7	107	**27.7**	**2225.2**	**103**
	5000	33.1	6576.7	63	26.8	5148.5	37	**33.3**	**5248.1**	**50**

TABLE A14 - Summary of the kinetic and thermodynamic parameters obtained when introducing fluorinated amino acids in the sequence. Experiments were performed in triplicate. All values are depicted as mean ± standard error of the mean (SEM).

		1	2	3	Mean ± SEM
	Δx_{N-TS} **(nm)**	1.69	1.91	1.56	1.72 ± 0.10
A4/B4$_F$	k_{off} **(s^{-1})**	2.9 x 10^{-3}	8.6 x 10^{-3}	1.2 x 10^{-2}	(7.8 ± 2.6) x 10^{-3}
	ΔG_{N-TS} **(k$_B$T)**	25.9	24.8	24.5	25.0 ± 0.4

14. ACKNOWLEDGEMENTS